8-12-2016

Multiscale Modeling of Multiphase Polymers

William Brantley Lawrimore

Multiscale modeling of multiphase polymers

By

William Brantley Lawrimore II

A Dissertation
Submitted to the Faculty of
Mississippi State University
in Partial Fulfillment of the Requirements
for the Degree of Doctor of Philosophy
in Mechanical Engineering
in the Department of Mechanical Engineering

Mississippi State, Mississippi

August 2016

Multiscale modeling of multiphase polymers

By

William Brantley Lawrimore II

Approved:

_____

Mark F. Horstemeyer
(Major Professor)

_____

Mei Qiang Chandler
(Committee Member)

_____

Tonya W. Stone
(Committee Member)

_____

Youssef Hammi
(Committee Member)

_____

D. Keith Walters
(Graduate Coordinator)

_____

Jason M. Keith
Dean
Bagley College of Engineering

Name: William Brantley Lawrimore II

Date of Degree: August 12, 2016

Institution: Mississippi State University

Major Field: Mechanical Engineering

Major Professor: Mark F. Horstemeyer

Title of Study: Multiscale modeling of multiphase polymers

Pages in Study: 127

Candidate for Degree of Doctor of Philosophy

Accurately simulating material systems in a virtual environment requires the synthesis and utilization of all relevant information regarding performance mechanisms for the material occurring over a range of length and time scales. Multiscale modeling is the basis for the Integrated Computational Materials Engineering (ICME) Paradigm and is a powerful tool for accurate material simulations. However, while ICME has experienced adoption among those in the metals community, it has not gained traction in polymer research. This thesis seeks establish a hierarchical multiscale modeling methodology for simulating polymers containing secondary phases.

The investigation laid out in the chapters below uses mesoscopic Finite Element Analysis (FEA) as a foundation to build a multiscale modeling methodology for polymer material systems. At the mesoscale a Design of Experiments (DOE) parametric study utilizing FEA of polymers containing defects compared the relative impacts of a selection of parameters on damage growth and coalescence in polymers. Of the parameters considered, the applied stress state proved to be the most crucial parameter affecting damage growth and coalescence.

At the macroscale, the significant influence of the applied stress state on damage growth and coalescence in polymers (upscaled from the mesoscale) motivated an expansion of the Bouvard Internal State Variable (ISV) (Bouvard *et al*. 2013) polymer model stress state sensitivity. Deviatoric stress invariants were utilized to modify the Bouvard ISV model to account for asymmetry in polymer mechanical performance across different stress states (tension, compression, torsion).

Lastly, this work implements a hierarchical multiscale modeling methodology to examine parametric effects of heterogeneities on Polymer/Clay Nanocomposite's (PCNs) mechanical performance under uncertainty. A Virtual Composite Structure Generator (VCSG) built three-dimensional periodic Representative Volume Elements (RVEs) coupled to the Bouvard ISV model and a Cohesive Zone Model (CZM) which featured a Traction-Separation (T-S) rule calibrated to results upscaled from Molecular Dynamics (MD) simulations. A DOE parametric examination utilized the RVEs to determine the relative effects of a selection of parameters on the mechanical performance of PCNs. DOE results determined that nanoclay particle orientation was the most influential parameter affecting PCN elastic modulus while intercalated interlamellar gallery strength had the greatest influence on PCN yield stress.

DEDICATION

I dedicate the endeavor presented herein to my parents William and Patricia Lawrimore whose steadfast and unwavering love, support, and understanding were paramount in pushing me through this ordeal. And to the rest of my close friends and family who helped and supported me during this undertaking.

ACKNOWLEDGEMENTS

First I want to thank my advisor Dr. Mark Horstemeyer. You took a risk on a stubborn, hopelessly unqualified student who barely managed to meet the requirements for acceptance into graduate school. Somehow, unfathomably you managed mold that hopeless student into a researcher. Your influence on me is unquestionable and today I am unrecognizable from the student that appeared in your office all those years ago. Thank you for all your effort, faith, and patience.

I'd like to thank the members of my graduate committee Mei Chandler, Tonya Stone, and Youssef Hammi for your support and guidance during my grad student tenure. Your vision and experience have been invaluable to me and my research and without each of you I would not have been able to make it this far.

I'd also like to thank all of the folks at CAVS and HPC2 who have collaborated, encouraged, and supported me through during my pursuit of this degree: David Francis, Kyle Johnson, Ric Carino, Rose Mary Dill, Joey Jones, Bhasker Paliwal, Justin Hughes, Wil Whittington, Shane Brauer, Jeremiah Deang, and Alston Rush.

Lastly I want to acknowledge Courtney Killian. She has been constant source of love and encouragement. She has kept me steady and grounded as I faced one adversity after the next. If not for her I could not have succeeded.

TABLE OF CONTENTS

LIST OF TABLES

LIST OF FIGURES

CHAPTER I

INTRODUCTION

Energy scarcity is among the most prevalent dilemmas on Earth today. An extensive amount of research has been conducted on methods to increase energy efficiency in numerous applications. One such method and application is the use of lighter materials (magnesium alloys, aluminum alloys, and polymers) in commercial, industrial, and consumer automotive transportation. In particular, amorphous polymers represent an inexpensive and effective way to approach the energy scarcity problem and are widely employed today in many non-structural engineering applications. However, the use of polymeric materials demands a sufficient level of understanding of their behavior and therefore a sufficient ability to predict their future behavior.

Full comprehension of polymeric material behavior requires careful consideration of deformation phenomena at every relevant length scale. In the last decade there has been a significant movement in material modeling toward an integrated, multiscale approach. Integrated Computational Materials Engineering (ICME) (Horstemeyer 2012) seeks to better understand the nature of material behavior through the incorporation of mechanisms at all length scales but has mainly focused on metals. The intent of this endeavor is to examine polymeric materials from a multiscale perspective.

Currently, very few structural components subjected to mechanical, thermal, and chemical loads use polymer-based materials. Since the future likely calls for an increase

in polymer use for structural applications, a sound understanding of mechanical performance and failure mechanisms is important. In general, polymers have low thermal conductivities and high damping factors leading to temperature increases during loads. The induced temperature rise typically leads to an undesired softening of the material (Constable *et al*.1970; Riddell *et al*. 1966). Additionally, polymer systems can vary in structural complexity as some polymers are amorphous and some are crystalline and others are originally amorphous but transition to crystalline under strain (strain induced crystallization). However polymers also possess a lofty theoretical upside. Frank (1970) reported that chain aligned polymers (crystallization) can have elastic moduli on the order of steel for a fraction of the processing cost. Also it has been shown that a small amount of secondary filler added to polymeric hosts can dramatically increase their mechanical performance (Markarian 2007). This study seeks to unravel some of the mystery surrounding the structure-properties-performance relationships within polymers through the implementation of a multiscale modeling paradigm.

Computational methods provide a cost efficient mechanism for examining the behavior of material in a menagerie of scenarios that would be far more costly to analyze with physical testing. Furthermore, many test conditions simply cannot be reproduced adequately in a laboratory environment. In the polymer case, there are a handful of empirical models that have been developed (Bardenhagen *et al*. 1997; Christensen 1982; Govaert *et al*. 2000; Khan *et al*. 2006; Khan and Zhang 2001; Krempl 1995; Lubarda *et al*. 2003; Tervoort *et al*. 1997; van der Sluis *et al*. 2001). There have also been several reviews composed on these and other empirical models (Chaboche 1997; Zaïri *et al*. 2007). Phenomenological models capture inelastic and nonlinear behavior of polymers

(within constraints) well. However, they are based explicitly on observable phenomena and therefore fail to include the microstructural rearrangements that govern the inelastic material behavior in polymers (Rice 1971).

There are also a group of models for polymers based on physics (Boyce, Parks, and Argon 1988; Haward and Thackray 1968). These descriptions include microstructural rearrangements (Coleman and Gurtin 1967; Lemaitre and Chaboche 1990; Rice 1971) and thus do well to capture polymeric inelastic behavior under simple loading cases but they all lack Internal State Variable's (ISV) (Coleman and Gurtin 1967) which are required to capture complex or cyclic loading. Radon (1980) published a study on the complexities of fatigue in polymers and an apparent lack of literature and that deficiency continues to this day.

Computational techniques although exceedingly useful, are only beneficial when accurate modeling methods are employed. An accurate model must be based on laws of physics, must consider phenomena on all relevant length and time scales, and must correlate with physical experiments. Bouvard *et al.* (2009) reviewed the state of polymer modeling literature in depth focusing on the difficulties in modeling at different length scales. Bouvard later developed a physically-based, time and temperature dependent elastoviscoelastic-viscoplastic ISV model for polymers featuring ISV's for dissipative effects during inelastic deformation (J. L. Bouvard *et al*. 2013). A year later Francis *et al*. (2014) modified Bouvard's model by incorporating a rate and temperature dependent damage formulation into the ISV model. The Bouvard-Francis ISV model was used as a platform to launch a multiscale modeling methodology for polymers.

Chapters 2-4 in this manuscript were all submitted for publication as individual entities prior to the creation of this document. Each chapter contains versions of those submissions with only minor alterations. This dissertation is organized in the following way: Chapter 2 lays the ground work for simulations at the mesoscale. That ground work motivates a modification of the Bouvard ISV model using key information upscaled from the mesoscale (Chapter 3). The work in Chapter 2 also highlights key requirements which are then downscaled to motivate work at the micro/nanoscale in Chapter 4.

Chapter 2 contains a split-level factorial Design of Experiments (DOE) parametric study using a two-dimensional mesoscale Finite Element Analysis (FEA) to elicit the most essential aspects pertaining to void/crack growth and void/crack coalescence in polymers above the glass transition temperature. The FEA uses a physically-based, strain rate and temperature dependent, elastoviscoelastic-viscoplastic ISV polymer model that was calibrated to physical experiments for Polycarbonate (PC) and Acrylonitrile Butadiene Styrene (ABS). The DOE method examined the relative influences of seven independent parameters related to mechanics (stress state, strain rate, and temperature) and materials science (polymer blend, number of initial defects, defect type, and initial microporosity—also called the subscale free volume) with respect to both void/crack growth and void/crack coalescence in polymers. The results of the DOE algorithm clearly illustrated that the stress state and applied strain rate were the most critical factors affecting void/crack growth. For void/crack coalescence, the stress state and number of defects were the crucial parameters. The conclusions of this study help to give insight for the development of a macroscale damage model for polymers.

The key information discovered at the mesoscale in Chapter 2 was subsequently upscaled into the macroscale in Chapter 3. Thus, Chapter 3 describes a modification of the ISV model proposed by Bouvard *et al.* (2013) (and modified by Francis *et al*. (2014)) for polymers by including additional terms that distinguish tensile, compressive, and torsional (shear) stress states. A "stress function" is defined using the deviatoric invariants of stress and said function is appended onto each of the internal state variables in the Bouvard-Francis ISV polymer model. The modified model is then calibrated to tensile, compressive, and torsional experimental data for two materials (polycarbonate and polypropylene) to illustrate its general applicability. Finally, the model was validated against experimental data from a notched specimen in a three-point-bend test for polypropylene.

In Chapter 4 a factorial DOE parametric study using FEA of Polymer/Clay Nanocomposites (PCN) was conducted to expose the most crucial parameters affecting the performance of PCNs under quasi-static tension. In order to optimize the material design of a polymer-based composite with nanofillers, we presented a systematic methodology that comprises several different computational methods. Three-dimensional FEA comprising three-dimensional periodic Representative Volume Elements (RVEs) served as the platform from which the DOE investigation was performed. RVEs featured a Polyvinyl Alcohol (PVA) matrix governed by a physically-based, strain rate,and temperature dependent, elastoviscoelastic-viscoplastic ISV polymer model calibrated to physical experiments, elastic Montmorillonite (MMT) nanoclay inclusions, and PVA/MMT interfaces simulated with a Cohesive Zone Model (CZM). The CZM was based on a Traction-Separation (T-S) rule calibrated with the results of lower length scale

Molecular Dynamics (MD) simulations of a PVA/MMT interface. RVEs were constructed with a Virtual Composite Structure Generator (VCSG) based on Random Sequential Absorption (RSA) and barycentric interference detection (Passerello 1982). The DOE process utilized an Analysis of Variance (ANOVA) technique to analyze the relative influence of four parameters related to nanoclay particles within a polymer matrix (aspect ratio, orientation, intercalation, and gallery strength) with respect to the overall PCN mechanical performance while including uncertainty principles. Additionally a Monte Carlo (MC) routine featuring a Radial Basis Function (RBF) provided quantification for the uncertainty related to the multiscale modeling methodology used in this endeavor. Results of the DOE examination clearly highlighted nanoclay particle orientation as the most crucial parameter that determines the PCN elastic modulus while the interlayer gallery strength was determined to have the most influence on PCN yield strength. Although the material focus here was PCNs, the multiscale methodology of bridging information from MD to FEA and DOE coupled to RVEs generated with VCSG can be used for any sort of nanocomposite material system and is not limited to nanocomposites with only two materials.

Chapter 5 features a summary of the work that is presented herein as well as proposals for future research in the area of multiscale modeling of polymers.

CHAPTER II

A MESOMECHANICS PARAMETRIC FINITE ELEMENT STUDY OF DAMAGE GROWTH AND COALESCENCE IN POLYMERS USING AN ELASTOVISCOELASTIC-VISCOPLASTIC INTERNAL STATE VARIABLE MODEL[1]

2.1 Introduction

The rate at which humanity consumes energy is a global-scale dilemma that attracts a broad amount of attention in both the academic and commercial realms. Of the many forms of human energy expenditure, transportation (commercial and private) is one of the most universal and expensive. Trimming the weight of a vehicle can substantially reduce its energy cost. Optimizing a structural material with an objective to decrease weight for transportation vehicles holds promise in reducing energy usage along with decreasing emissions.

Polymers possess the potential to dramatically reduce vehicular weight by replacing heavier metallic components with lighter, optimized polymeric ones. Prior to polymers becoming eligible for use in vehicular architectural contexts, a considerable

[1] Lawrimore II, W.B., D.K. Francis, J.L. Bouvard, Y. Hammi, and M.F. Horstemeyer. 2016. "A Mesomechanics Parametric Finite Element Study of Damage Growth and Coalescence in Polymers Using an Internal State Variable Model." Mechanics of Materials 96 (February): 83–95. doi:10.1016/j.mechmat.2016.02.002.

amount of work remains to truly comprehend and exploit the unique behavior of polymers. Before replacing metallic alloys with polymers, the strength and particularly the fracture behavior of polymers needs to first be understood. Our study provides insight into the various parameters that influence fracture in polymers. In the context of Integrated Computational Materials Engineering (ICME) (cf., Horstemeyer 2012), this work employs mesoscale finite element analysis to determine the relative influence of the engineering parameters which are most crucial for damage growth and coalescence in polymers. Once an understanding of void/crack growth and coalescence is obtained, fracture can in turn be better understood.

Thermoplastics, a polymer subclass, look to be the most viable approach for applying polymers to vehicular components. Thermoplastics typically feature polymer chain entanglements as opposed to the bonded cross-links observed in thermosets. Thus thermoplastics can be melted and resolidified without degrading their mechanical properties. This reversible process allows the addition of secondary phases (which are typically included to modify the performance of polymers) without deleterious effects. Stiff secondary phases are added to increase a polymer's strength while softer, elastomeric secondary phases are used to improve a polymer's impact properties.

The polymer strengthening mechanism can occur with only a small percentage of second phase material (Markarian 2007) thus increasing the specific strength. By comprehending the complete set of boundary and environmental conditions, polymer structures can be used within automobiles to reduce their weight. In the present study, a DOE method was employed to uncover the most influential parameters that affect damage growth and coalescence in polymers.

The earliest works that relate statistical procedures to physical experiments are attributed to Sir Ronald Fisher (1935a, b). As a result of his work, statisticians used several analysis of variance techniques to interpret physical experimental data (Box *et al.* 1978). DOE is one such technique. Taguchi (1974, 1986, 1987) popularized the DOE method for use in the quality-engineering area. In the present DOE study, the 'experiments' are not physical but numerical in nature. Briefly, the DOE method uses a split-level geometric array of unique condition combinations to extract the influence of parameters that are most critical to a particular result. For example, Horstemeyer *et al.* (1999) implemented a DOE method into a mesoscale crystal plasticity framework to understand the relative macroscale effects of a variety of mesoscale constitutive models on the behavior of FCC metals. The study concluded that intergranular constraints and kinematic hardening were much more influential than the type of constitutive model used. Gall *et al.* (2000) used a two-dimensional mesoscale finite element analysis within a DOE framework to investigate the effects matrix-particle morphology on the fracture and debonding of silicon particles enclosed within an aluminum matrix. The study identified temperature as the critical parameter for the fracture and debonding of silicon particles. For analyzing void growth and coalescence in different metal alloys, Horstemeyer and Ramaswamy (2000c) examined different variables and showed that temperature and microporosity played the most dominant roles. Later, Horstemeyer *et al.* (2003) conducted finite element simulations guided by a DOE matrix to quantify the relative influence of different parameters on void nucleation. Wang *et al.* (2009) used the DOE technique coupled with crystal plasticity in mesoscale finite element simulations to determine that the remote applied displacement is the most important parameter affecting

fatigue crack incubation in a 7075 aluminum alloy when compared to some microstructural features. These different DOE studies have shown in some cases that the mechanics issues are more important but in others the microstructural morphology is more important, each depending on the variables and metrics of interest. Furthermore, all of these studies included a metal of some type, so the current study is the first of its kind for a polymer-based material system.

This investigation parallels the Horstemeyer and Ramaswamy (2000c) study but instead of evaluating metals focuses on polymers by using two-dimensional mesoscale finite element simulations using a physically-based, rate and temperature sensitive ISV model to describe the behavior of polymers (Bouvard *et al*. 2013). The simulations were cast in a DOE framework featuring seven parameters each accommodating an upper bound and a lower bound to identify which parameter(s) is(are) most crucial to damage incubation and damage growth in polymers. The authors chose the DOE parameters and limiting bounds based on literature and available experimental data which include the following: polymer blend, number of initial defects, defect type, temperature, stress state, strain rate, and initial microporosity (molar volume).

2.2 Metrics

The metrics for polymer fracture quantification used here have a historical precedence from metals. Horstemeyer *et al.* (2000a) stated that in the case of metals, damage is characterized by three individual components: nucleation, growth, and coalescence. Francis *et al.* (2014) extended the damage/fracture methodology to polymers. Typically, the damage parameters (void/crack nucleation, void/crack growth, and void/crack coalescence) are functions of the stress triaxiality and maximum local

inelastic strain. In this investigation The stress triaxiality is defined as the tensile hydrostatic stress (negative pressure) divided by the equivalent von Mises stress while the local inelastic strain is defined by the von Mises equivalent inelastic strain. Looking at the stress triaxiality and local inelastic strain as two metrics for polymer damage, the total void volume fraction would be a resulting metric as well in our study. Furthermore, a well-accepted continuum description for void growth in metals was developed by Cocks and Ashby (1980).

$$\dot{\phi}_{pores} = \chi \left[\frac{1}{(1-\phi_{pores})^{m}} - \left(1 - \phi_{pores}\right) \right] \left\| \boldsymbol{D}_p \right\| \tag{2.1}$$

$$\chi = \sinh \left[\frac{2(m-0.5)}{(m+0.5)} \frac{p}{\sigma_e} \right] \tag{2.2}$$

where ϕ_{pores} is the volume fraction of voids in the material, $\boldsymbol{D}_p$ is the inelastic rate of deformation, p is the tensile hydrostatic pressure, σ_e is the von Mises equivalent stress, and m is the strain rate sensitivity parameter. Void growth exhibits a dependence on both stress triaxiality (Eq. 2.2) and inelastic strain (Eq. 2.1). Francis *et al.* (2014) implemented Eqs. 2.1 and 2.2 into a macroscale damage framework including damage from pores, particles, and crazing built on a modified inelastic amorphous glassy thermoplastic ISV model (Bouvard *et al.* 2013). In that work, Francis *et al.* (2014) showed that the Cocks-Ashby void growth equations (Eqs. 2.1 and 2.2) that were intended for metals work very well for polymers.

In terms of coalescence of voids/cracks, Brown and Embury (1973) defined coalescence as the first impingement of two different voids. Tvergaard (1990) proposed that coalescence did not occur until the onset of final fracture. However, Lu *et al.* (1998) showed that voids can interact much earlier than the commencement of fracture through

notch tensile tests of 304L stainless steel. Moreover, Horstemeyer *et al.* (2000b) conducted micromechanical finite element simulations of discrete voids showing that when multiple voids are in close proximity, their void growth rate will increase dramatically due to the neighboring effects of adjacent voids. For polymers, Francis *et al.* (2014) developed a coalescence ISV rate equation that was essentially an interactive term between voids and crazes and is a function of the nearest neighbor distance of voids/crazes and size of voids/crazes, temperature, and strain rate. To demonstrate "enhanced void growth," for this study two finite element simulations identical except for the number of voids present were executed using the ISV model for polymers. The dramatic increase in void growth rate between the single void case and the two void case simulations are shown in Fig. 2.1. Given these arguments about coalescence, the current study incorporates coalescence since the total void volume fraction will include single and two void cases.

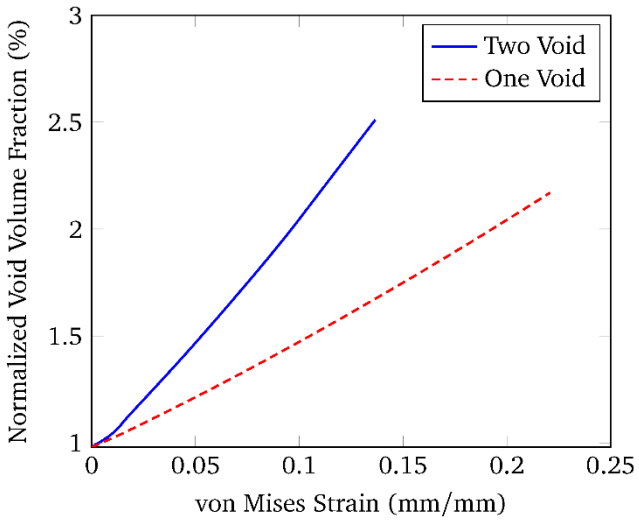

Figure 2.1 Testing phase simulation results showing normalized void volume fraction versus von Mises strain highlighting the "enhanced void growth" that occurs when two voids are in close proximity.

2.3 Parameters

The ISV model requires calibration to experimental data in order to provide a reasonable engineering approximation of polymer behavior. As such, the collection of available experimental data provided a primary constraint to the selection and quantification of DOE parameters. Appendix C contains a detailed overview of the ISV model forms while Appendix A contains the calibrated material parameters for both ABS and PC.

2.3.1 Polymer Blend

This study focused on two distinct polymer blends: Acrylonitrile Butadiene Styrene (ABS) and Polycarbonate (PC). ABS is an engineering grade, high impact polymer produced by polymerizing styrene and acrylonitrile with polybutadiene. The investigated grade of ABS contains carbon-based inclusions that have an average diameter of 3.5 microns and an average particle nearest neighbor distance of 1.4 microns (cf., Lugo *et al*. 2014). PC is a polymer chain of carbonate groups that is created through a reaction between phosgene and bisphenol A (BPA). Both polymers are sensitive to temperature fluctuations and changes in strain rate showing a large deviation in stress–strain behavior when either condition is altered (Abts, Eckel, and Wehrmann 2014).

The stress–strain comparison of the ISV model with the experimental data is shown in Figs. 2.2 and 2.3 for PC and ABS, respectively. The experimental data for both PC and ABS for all strain rates and temperatures was obtained from Bouvard *et al.* (2011). This model calibration was completed before the DOE analysis was conducted using a material point simulator in Matlab followed by single element finite element simulations. Note that the ISV captures the temperature and strain rate dependence with

one set of material constants. Note also that yield stress was approximately 60 MPa for PC and 40 MPa for ABS. PC softens after yielding, while ABS experiences a short-range transient of softening following by hardening. These two different polymers have been used as mechanical load bearing structures.

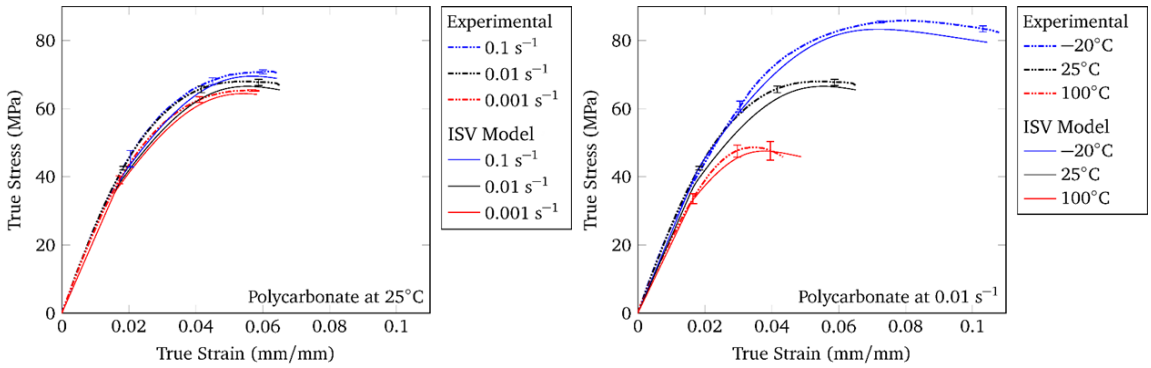

Figure 2.2 True stress - true strain curves under tension comparing the thermoplastic internal state variable model over a range of strain rates (left) and temperatures (right) with experiments for polycarbonate.

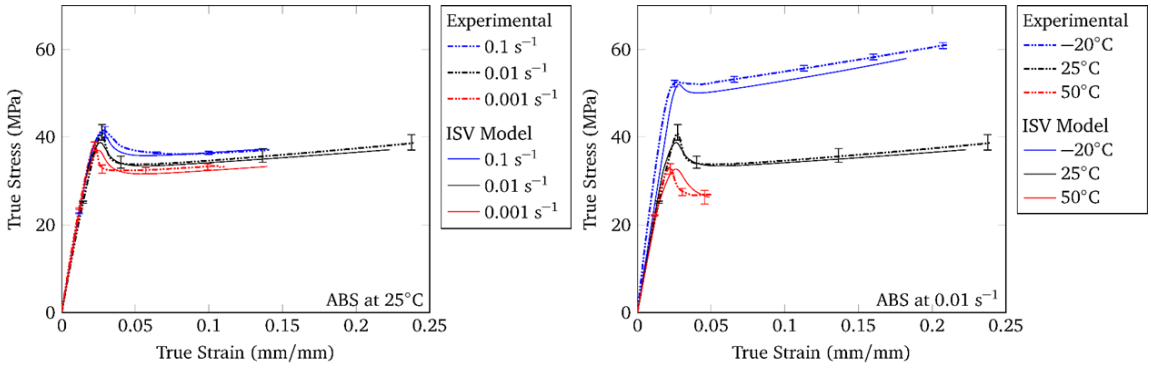

Figure 2.3 True stress - true strain curves under tension comparing the thermoplastic internal state variable model over a range of strain rates (left) and temperatures (right) with experiments for acrylonitrile butadiene styrene (ABS).

2.3.2 Particle/Void

Most structural polymers are not monolithic materials but include multiscale microstructures in the form of hard phases, voids/cracks, or carbon based strengtheners. The added constituents typically serve to make the material stronger while adding very little mass; however, the inclusions (voids/cracks) will provoke deleterious effects on the material's mechanical properties. Most engineering polymers contain some level of porosity due to the manufacturing processes. Tjia and Moghe (1998) used a confocal microscope to quantify the microstructure of solvent casted – salt leached porous poly (lactic-acid, glycol-acid) (PLAGA). The study found that when the salt concentration was low, the effective void size was directly related to the size of the salt particles. Day *et al.* (2002) used multiphoton absorption under an infrared beam that illuminated the voids in a doped polymethylmethacrylate (PMMA). Lugo *et al.* (2014) used optical microscopy and image analysis to quantify particle and porosity properties in ABS. The investigation reported an average particle diameter of 3.55 μm and an average pore size of 0.059 μm.

In this study, we employ the idea that the structural polymer could have inherent porosity or included additives via the polymer manufacturing process. In this way, it is not clear if the inclusion or microstructures induce strengthening or weakening. As such, we will examine the effect of the inclusions to assess if they influence the damage state and thus weaken the material.

2.3.3 Number of Inclusions

Inclusions within polymers typically arise from the processing associated with the initial chemistry of the material. After processing, a polymer's inclusions are inhomogeneously present in various shapes, sizes, and clusters throughout the material.

The pattern of the defect distribution becomes important while considering damage nucleation. Some regions of the material could have regions with heavy concentrations of particles or pores, while other regions may be relatively free of the inclusions. The local inclusion interaction effects were examined by constraining the nearest neighbor distance to remain equal in all cases and varying the number of inclusions (either 1 or 2). The performance contrast between one and two inclusions is an indicator of the effect that inclusion coalescence has on the material. All of the initial conditions have the same area fraction of defects; thus, when two defects are present, they are initially smaller than the case when only one is initially present. In Horstemeyer *et al.* (2000b) a larger single defect incurred damage growth at a lesser rate than two smaller defects, when the defect diameter was the distance between the defects. In another study, Fu *et al.* (2008) reviewed the effects of particle size and density on the mechanical response of particles embedded in polymer systems finding that the aggregate normalized elastic modulus increased as particle volume fraction increased.

2.3.4 Temperature

The stress–strain behavior of polymers is highly temperature dependent (cf., Arruda *et al.* 1995; Francis *et al.* 2014). The temperature dependence of the stress–strain behavior for ABS and PC is shown in Figs. 2.2 and 2.3, respectively. As the temperature increases, the flow stress and strain hardening effects decrease in general. In terms of damage, Tijssens *et al.* (2000) showed the importance that temperature plays in crazing. Elongations to failure typically increase when the temperature increases. Finally, the elastic moduli decreases as the temperature increases. In Horstemeyer *et al.* (2003), mesoscale finite element simulations showed that the temperature effects had the greatest

influence in damage nucleation when compared to other parameters like microporosity, defect size, defect shape, and the number of defects for metals. Whether or not the observations of Horstemeyer *et al.* (2003) will occur for polymers is yet to be realized, hence, one reason for the current study.

Another temperature dependent issue for polymers is the glass transition temperature, which indicates the temperature at which a polymer will transition from a hard, glassy material to a soft material. Our study focused on temperatures below the glass transition temperature ($T_g^{PC} = 428\ K, T_g^{ABS} = 373\ K$). As such, all experiments and simulations were conducted at temperatures well below the glass transition thresholds for both thermoplastics. The two temperatures chosen as limits for this parametric study were 253 K and 323 K, which are reasonable bounds for standard vehicular chassis temperature requirements.

2.3.5 Stress State

Bridgman (1923) conducted experiments on a variety of metal alloys discovering that a rise in stress triaxiality elicited a corresponding increase in damage nucleation and growth. Since then, a vast array of damage models for metals have emerged starting with McClintock (1968). One damage study for analysis of polymers is that of Asp *et al.* (1996), who studied the failure behavior of epoxy systems under uniaxial, biaxial, and triaxial stress states. The study concluded that the epoxies considered exhibited much lower strains-to-failure and brittle-like behavior in equibiaxial and equitriaxial tension as opposed to yielding and “ductility” observed in uniaxial tension. This work examines both uniaxial and biaxial tensile deformation inducing two different levels of the stress triaxiality.

2.3.6 Strain Rate

As Figures 2.2 and 2.3 illustrate, the material behavior of both ABS and PC are modestly strain rate dependent. Both materials exhibit an escalation in the yield stress as their applied strain rate rises with ABS showing a much larger dependence. Hagerman (1973) examined the effect that applied strain rate had on craze growth in ABS. The study examined micrographs of ABS loaded at different rates and concluded that lower strain rates allowed crazes to grow longer (dissipating energy) before fracture occurred. Chen and Sauer (1990) investigated the yield behavior of ABS across a range of loading rates. The study revealed that the yield stress of ABS varied linearly with the log of the applied strain rate. Siviour *et al.* (2005) performed high strain rate mechanical compression tests on PC and saw a drastic increase in both elasticity and yield stress. Inberg *et al.* (2002) performed single edge notch tensile tests over a range of strain rates on PC/ABS blends. They concluded that under greater applied strain rates, the PC/ABS blends displayed greater maximum stresses and fracture energies. Here, the investigation explores deformation under different strain rates spanning multiple orders of magnitude.

2.3.7 Microporosity

Budd *et al.* (2005) reviewed intrinsic microporosity and free volume in polymers finding that polymers with intrinsic microporosity (PIMs) are fabricated with molecular backbones that simultaneously have no conformation freedom but are highly contorted to impede effective packing. Furthermore, Budd *et al.* (2005) discussed the vagueness of the term "free volume" and connected it to the term microporosity: "[a polymer with] a large amount of interconnected free volume in the glassy state behaves in many respects like microporous materials." Cooper (2009) reviewed a variety of methods for fabricating

conjugated microporous polymers (CMP's) and found that in many cases, the CMP networks showed very little or no phase segregation meaning the CMP's consisted of low density, high surface area, near-homogeneous material. Consistent with Horstemeyer and Ramaswamy (2000) microporosity is a continuum quantity that is distributed evenly within each element in a finite element mesh. The microporosity was defined by an "initial void volume fraction" within the Cocks-Ashby relationship (Equation 1). The initial microporosity or free volume levels were 0.0 (no microporosity) and 0.001 for the finite element simulations.

2.4 Internal State Variable Model

A physically-based, rate and temperature dependent ISV model for polymers developed by Bouvard *et al.* (2013) was used to accurately represent both ABS and PC. The ISV model was calibrated to physical experiments at a variety of temperatures and strain rates for both PC and ABS (Figures 2.2 and 2.3). The constitutive model features three ISVs to account for inelastic dissipation mechanisms in polymers:$\bar{\xi}_1$ is a strain-like scalar that accounts for dissipation induced from polymer chain entanglement points; $\bar{\xi}_2$ is a strain-like scalar that represents material hardening resulting from polymer chain alignment and coiling at large strains; $\bar{\boldsymbol{\alpha}}$ is a strain-like tensor that accounts for hardening induced by polymer chain orientation and stretching at large strains. For an overview of the ISV model, refer to Appendix C.

2.5 Design of Experiments Methodology

This study compares the relative parametric influences between the parameters described in Section 2.2 on damage growth and coalescence in polymers. Having seven

parameters quantified at two levels yields 128 (2^7) unique simulations (one for each possible parameter grouping). The DOE technique is essentially a tool that selects a minimum spanning set for the simulation space based on some criteria. The DOE method creates a linear mapping from a set of influences, {A}, to a set of responses, {R}, through a parameter matrix, **[P]** corresponding to the orthogonal array with

$$\{R\} = [\boldsymbol{P}]\{A\} \tag{2.3}$$

where

$$\{R\} = \begin{Bmatrix} R_0 \\ R_1 \\ R_2 \\ R_3 \\ R_4 \\ R_5 \\ R_6 \\ R_7 \end{Bmatrix}, \{A\} = \begin{Bmatrix} A_0 \\ A_1 \\ A_2 \\ A_3 \\ A_4 \\ A_5 \\ A_6 \\ A_7 \end{Bmatrix}, \ [\boldsymbol{P}] = \begin{bmatrix} +1 & -1 & -1 & -1 & -1 & -1 & -1 & -1 \\ +1 & -1 & -1 & -1 & +1 & +1 & +1 & +1 \\ +1 & -1 & +1 & +1 & -1 & -1 & +1 & +1 \\ +1 & -1 & +1 & +1 & +1 & +1 & -1 & -1 \\ +1 & +1 & -1 & +1 & -1 & +1 & -1 & +1 \\ +1 & +1 & -1 & +1 & +1 & -1 & +1 & -1 \\ +1 & +1 & +1 & -1 & -1 & +1 & -1 & +1 \\ +1 & +1 & +1 & -1 & +1 & -1 & +1 & -1 \end{bmatrix} \tag{2.4}$$

The set of influences, {A} is found by inverting Equation (2.3),

$$\{A\} = [\boldsymbol{P}]^{-\mathbf{1}}\{R\} \tag{2.5}$$

Since this investigation is only concerned with the first order main parametric effects, only eight simulations are needed to span the simulation space (DeVor *et al.* 1992). An orthogonal array with parameter definitions for each simulation is shown in Table 2.1.

Table 2.1 L_8 orthogonal array displaying design of experiment (DOE) simulation conditions.

Calc	Material	Particle/ Void	One/Two Inclusion (s)	Temperature (K)	Stress State	Strain Rate (1/s)	Microporosity (Vol Frac)
1	ABS (-)	Void (-)	One (-)	253 (-)	Uniaxial (-)	0.001 (-)	0 (-)
2	ABS (-)	Void (-)	One (-)	323 (+)	Biaxial (+)	0.1 (+)	1e-3 (+)
3	ABS (-)	Particle (+)	Two (+)	253 (-)	Uniaxial (-)	0.1 (+)	1e-3 (+)
4	ABS (-)	Particle (+)	Two (+)	323 (+)	Biaxial (+)	0.001 (-)	0 (-)
5	PC (+)	Void (-)	Two (+)	253 (-)	Biaxial (+)	0.001 (-)	1e-3 (+)
6	PC (+)	Void (-)	Two (+)	323 (+)	Uniaxial (-)	0.1 (+)	0 (-)
7	PC (+)	Particle (+)	One (-)	253 (-)	Biaxial (+)	0.1 (+)	0 (-)
8	PC (+)	Particle (+)	One (-)	323 (+)	Uniaxial (-)	0.001 (-)	1e-3 (+)

2.5.1 Finite Element Analysis

The explicit, dynamic finite element code ABAQUS (v 6.11) was used for each DOE computation (Hibbitt 1984). The polymeric ISV constitutive model referred to in Section 2.4 was inserted via an explicit user subroutine (VUMAT). 2.4 contains a schematic of the geometries and boundary conditions used in the parametric finite element analysis. Each simulation was built on one of four idealized two-dimensional, plane strain meshes. Each mesh consisted of either one or two circular defects that were either particles or voids. In the case where the defects were particles, non-bonded, rigid particles were used. A minimum distance of four defect diameters separated all defects from all mesh edges (this distance was defined in Horstemeyer *et al.* (2000b) as the minimum distance where no interaction between voids would occur). When two defects

were present, their centers were separated by two defect diameters. Each mesh had an equivalent initial defect volume fraction except for those meshes containing microporosity. All computations featured a 4.7 % remote applied strain to capture (as much as possible) post-yield behavior before failure.

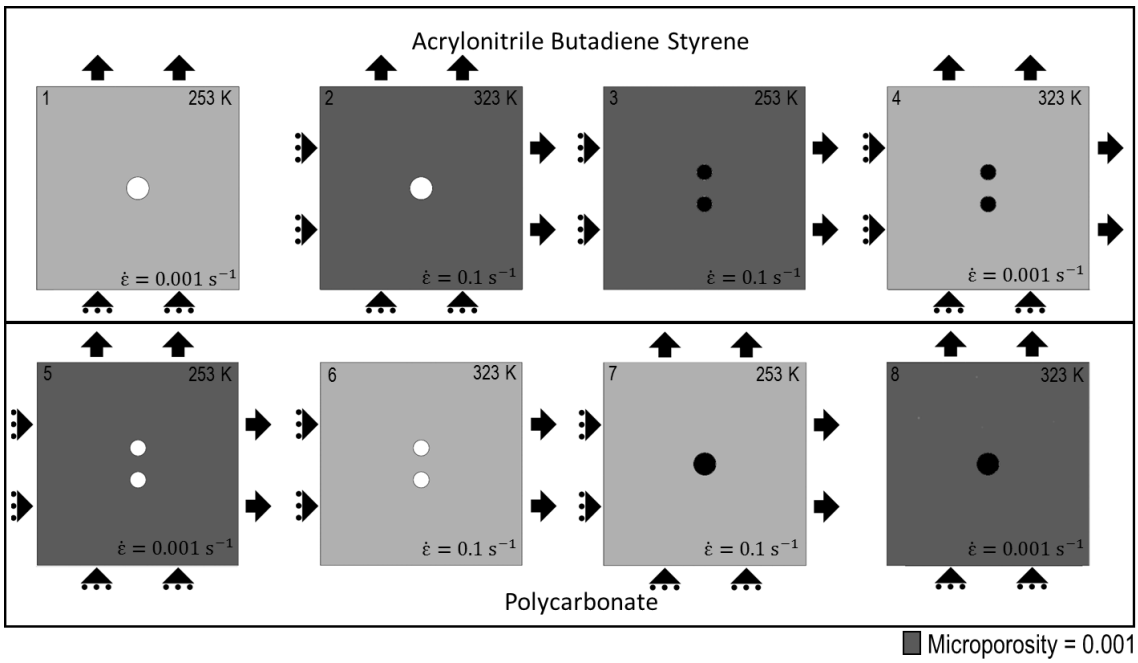

Figure 2.4 Finite element schematic of the geometries, design aspects, and boundary conditions for eight design of experiments simulations for two different materials.

2.6 Mesomechanical Parametric Finite Element Results

2.6.1 Stress Triaxiality

Since stress triaxiality is a continuum quantity, the stress triaxiality volume average over all of the elements was calculated for the duration of each simulation. Equation 2.6 was used to obtain the mesh average stress triaxiality.

$$\chi_{mesh} = \frac{1}{N}\sum_{i=1}^{N}\chi_i;\ \ \chi_i = \frac{p_i}{\sigma_i^e} \tag{2.6}$$

where χ_{mesh} is the average triaxiality for the whole mesh, N is the number of elements, χ_i is the triaxiality for the i^{th} element, p_i is the pressure for the i^{th} element, and σ_i^e is the equivalent stress for the i^{th} element. Fig. 2.5 shows a complete amalgam of contour plots exhibiting the stress triaxiality distributions for each of the eight DOE finite element simulations determined at the peak load. The normalized quantification of the main parametric effects of each DOE parameter (Fig. 2.6) correspond to the stress triaxiality data in Fig. 2.5. The first order influence parameter was the stress state dependence, i.e., the increase from the uniaxial to the biaxial loading conditions. Inherently, the importance of stress state on the triaxiality parameter is consistent with Equation (2.2), as the biaxial loading cases have an extra stress dimension and therefore higher triaxiality.

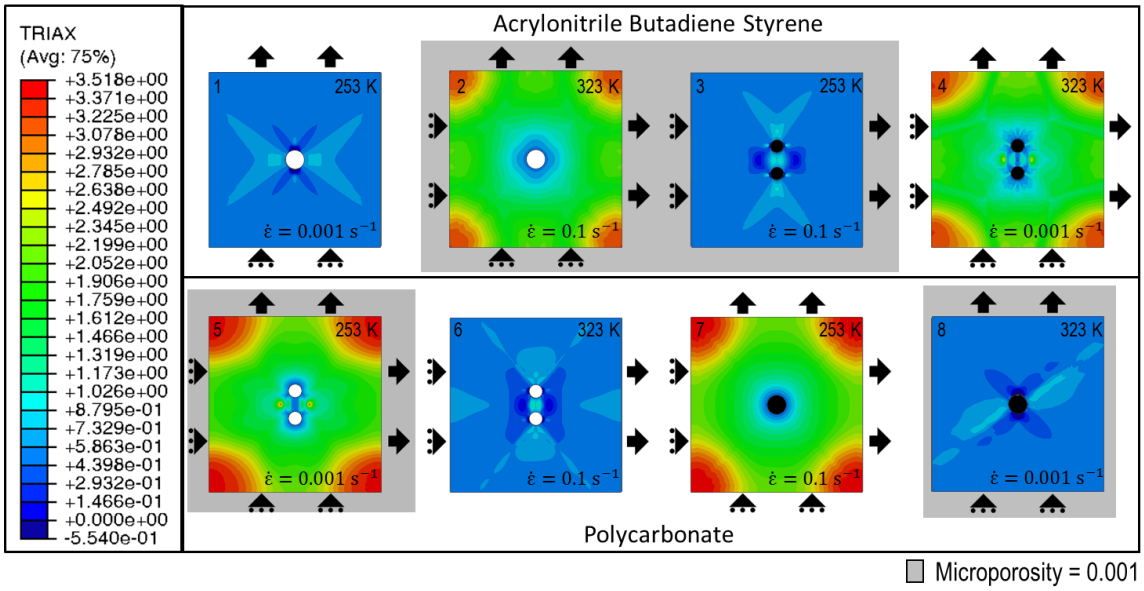

Figure 2.5 Stress triaxiality contour plots from each design of experiments finite element computations at the peak load.

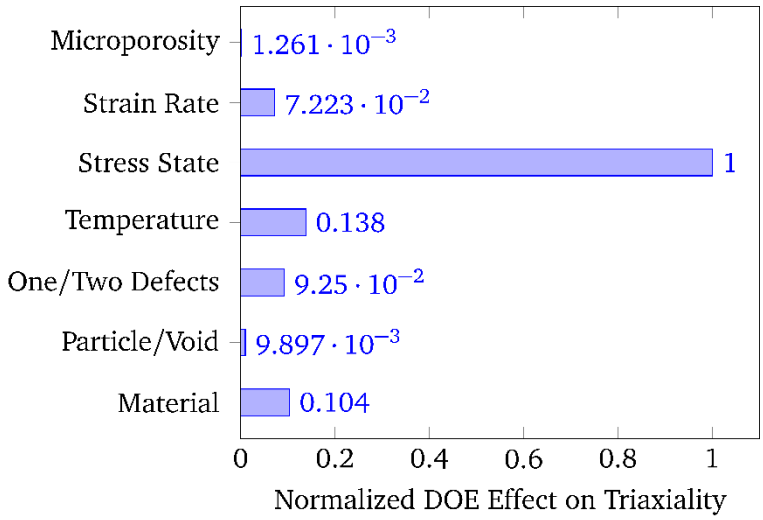

Figure 2.6 Normalized influence of each design of experiments parameter on the aggregate stress triaxiality.

Note that all influences were normalized to the maximum influence value.

2.6.2 Local Maximum Equivalent Inelastic Strain

In each simulation the maximum value of inelastic strain was extracted at the peak loading. The equivalent inelastic strain contours at the peak loading for each simulation (Fig. 2.7) and the normalized first order influences of each DOE parameter on the maximum local inelastic strain (Fig. 2.8) illustrate that the stress state is the primary influence on local inelastic strain. A change in temperature exhibits the second highest influence on inelastic strain, which is reasonable for polymers, a class of materials very sensitive to heat transfer. The number of defects provides a tertiary influence implying that the stress fields from neighboring defects interact and exacerbate the local strains.

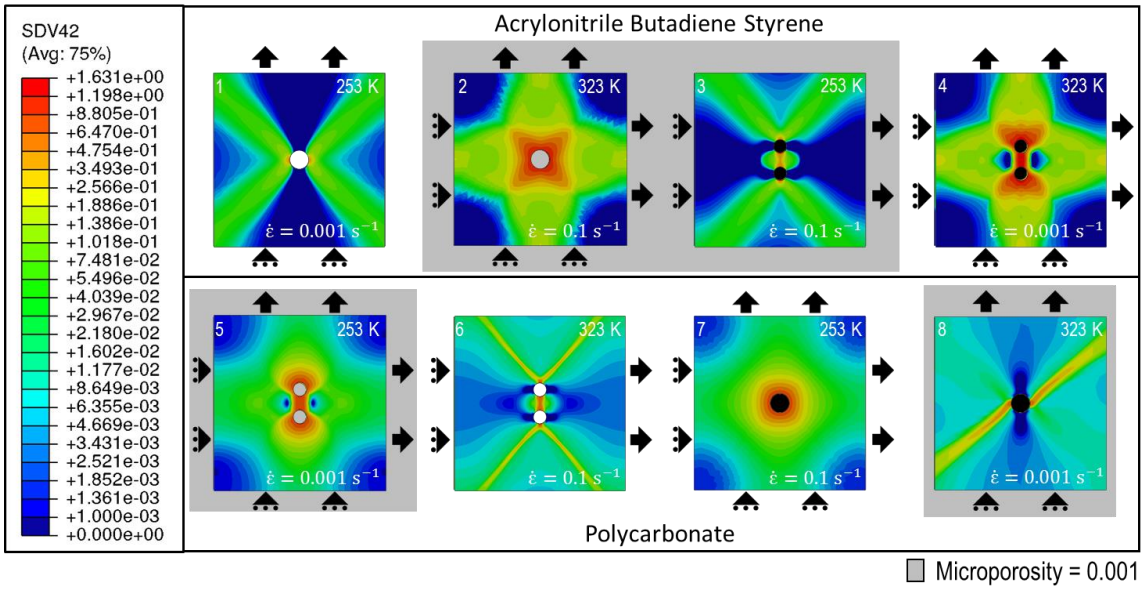

Figure 2.7 Schematic showing equivalent inelastic strain contour plots for each design of experiments simulation at the peak load.

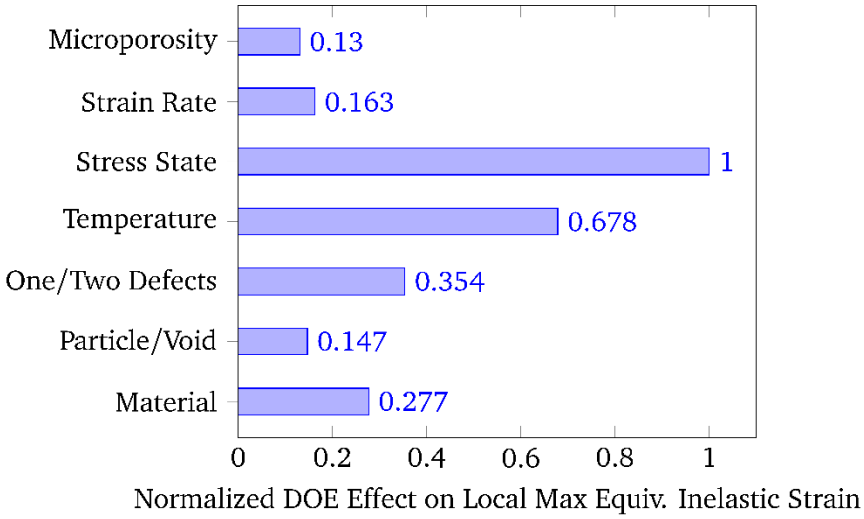

Figure 2.8 Normalized influence of each design of experiments parameter on the local maximum equivalent inelastic strain.

Note that all influences were normalized to the maximum influence value.

2.6.3 Void Volume Fraction

The void volume (area) fraction was observed for the duration of each simulation. The area (since the calculations are two-dimensional) of the voids was calculated using the following:

$$A = \sum_i \pi \, (r_1 r_2)_i \tag{2.7}$$

where i represents an elliptical void within a mesh and r_1 and r_2 are the major and minor axes of an ellipse. The void area fraction versus far field applied von Mises strain for both uniaxial and biaxial DOE cases is plotted in Fig. 2.9. As in the previous section, the stress state is the largest influence on void growth rate. While the uniaxial case does display a clear dependence on strain rate and number of defects, the level of influence is negligible when compared to that of stress state. Note that for Calculation 8, the simulation exhibited strain localization because of the particular boundary conditions. This localization resulted in shear bands forming. Normalizing the first order parametric effects on final (peak loading) void volume fraction (Fig. 2.10) shows that increasing from uniaxial to biaxial loading culminates in the greatest increase of the final void volume fraction. Meanwhile an increase in temperature or a reduction in material strength results in a secondary increase in final void volume fraction.

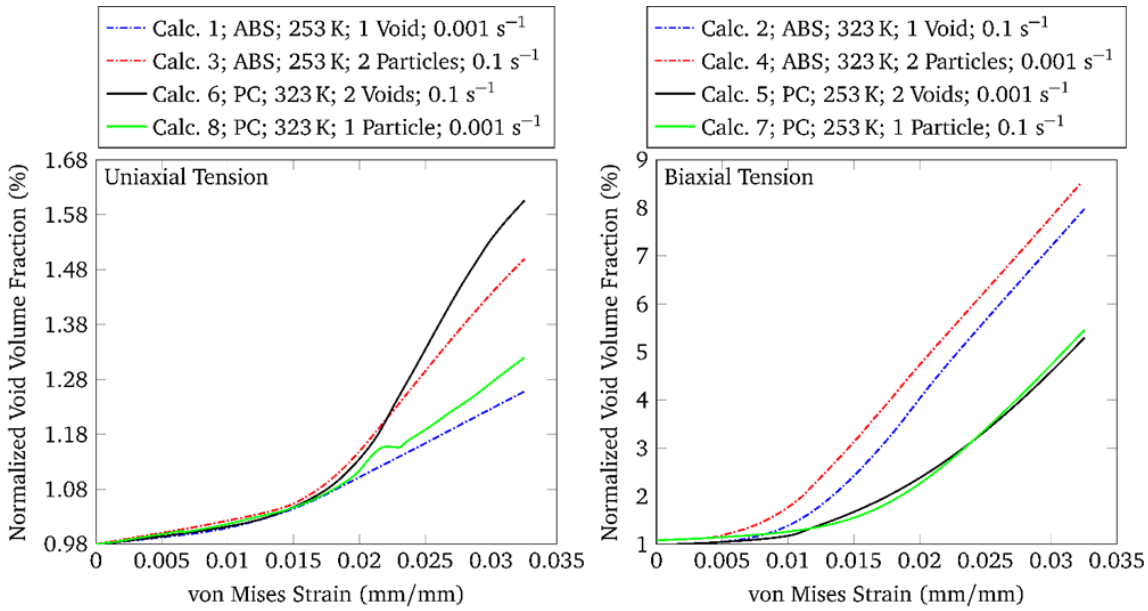

Figure 2.9 Void area fraction versus applied von Mises strain plots for uniaxial loading and biaxial loading.

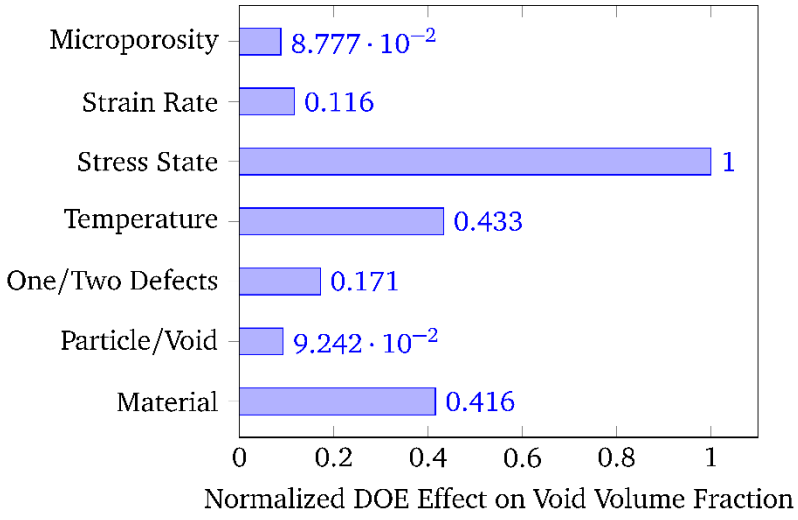

Figure 2.10 Normalized influence of each design of experiments parameter on the void volume fraction.

Note that all influences were normalized to the maximum influence value.

2.7 Summary

A DOE parametric study was conducted to discover the crucial influence parameters affecting damage growth and coalescence in polymers. The parametric study employed a finite element analysis coupled with an experimentally calibrated time and temperature sensitive ISV model for polymers. The analysis revealed that the stress state that induced a particular stress triaxiality was the most important parameter for damage growth. Researchers have argued that viscoelastic materials, such as the structural polymers represented in this study, have a strong strain rate and time sensitivity. Although these polymers do exhibit a strain rate and time sensitivity, the mechanism that induces void growth and coalescence the strongest is a large stress triaxiality arising from an elevated applied stress state with secondary contributions from the material having a larger yield stress and a higher temperature.

CHAPTER III

MODELING POLYMERIC STRESS STATE DEPENDENCIES USING INTERNAL STATE VARIABLE THEORY

3.1 Introduction

As discussed in the previous chapter, a polymer's stress state is the primary influencer in damage growth and coalescence. However, most polymer models (physically-based or otherwise) neglect stress state effects.

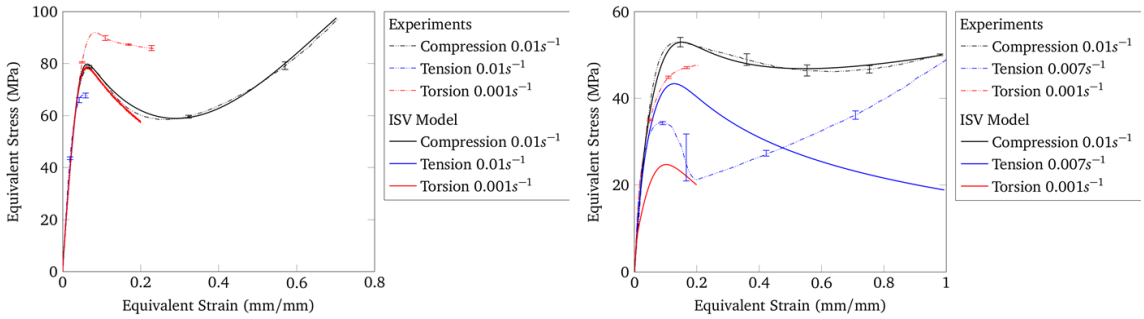

Figure 3.1 Calibration of Bouvard *et al.* Internal State Variable (ISV) model for Polycarbonate (left) and Polypropylene (PP) for tension, compression and torsion.

Note that the ISV model cannot capture polymer performance across different stress states.

Fig. 3.1 shows an attempt at calibrating the Bouvard *et al.* (2013) ISV model for Polycarbonate (PC) and Polypropylene (PP) over tension compression and torsion. From Fig. 3.1 it is apparent that the Bouvard *et al.* ISV model cannot adequately capture polymer mechanical performance asymmetry across stress states.

Employing polymeric material models with time and temperature dependence has been the subject of a large amount of attention. See Bouvard *et al.* (2010) for a detailed review of the history of polymeric modeling. Additionally there has been a significant amount of advancement in the last six years. Srivastava *et al*. (2010) developed a constitutive model based on the notion that as temperature rises (especially above the glass transition, T_g) the number of mechanisms for inelastic dissipation rises. Using this 'multi-mechanism' theory they were able to capture the polymer performance over a large range of strain rates and a range of temperatures that spanned the glass transition. Ayoub *et al*. (2011) proposed a physically-based hyperelastic-viscoplastic constitutive model to examine the effect of the level of crystallinity on the mechanical performance of Polyethylene (PE). Zaïri *et al*. (2011) developed a hyperelastic-viscoplastic constitutive model for rubber-toughened polymers under large strains. They determined that damage due to deformation in such materials is controlled by rubber cavitation. Launay *et al*. (2011) explored the cyclic behavior of short glass fiber reinforced (SGFR) Polyamide 66 through developing a viscoelastic-viscoplastic constitutive model that uses dissipated pseudo-viscoplastic energy to calculate cyclic softening. Khan and Yeakle (2011) examined non-monotonic creep behavior in polymers determining that pre-loading a polymer to maximum stress before unloading to a test stress drastically changes its mechanical behavior. They were able to predict this behavior with a state variable model featuring a modified viscoplasticity based on overstress. Fleischhauer *et al*. (2012) produced a strain rate and pressure sensitive constitutive model for polymers that captures post yield softening behavior over a large range of strain rates in tension. Voyiadjis, Shojaei, and Li (2012) proposed a viscoplastic-viscodamage-viscohealing

constitutive model using a novel viscoplastic theory featuring a modified backstress tensor to capture the irregular inelastic response of glassy polymers. Alisafaei, Han, and Garg (2016) developed a length scale sensitive elasto-plastic coupled stress model to capture length scale dependent deformation in polymers.

There has also been a considerable amount of constitutive model research in the realm of semi-crystalline polymer systems, as well as shape memory polymers (SMPs). Baghani *et al*. (2012) developed a constitutive model for SMPs featuring second phase 'hard segments'. This model was able to predict SMP behavior under multiaxial loading. Zhang and Yang (2012) conducted a review of recent studies performed on constitutive modeling of SMPs. Cayzac, Saï, and Laiarinandrasana (2013) constructed a constitutive model for semi-crystalline polymers using a multi-mechanism approach that accounted for both the semi-crystalline nature of Polyamide 6, as well as damage for tensile cases. Ponçot, Addiego, and Dahoun (2013) proposed a semi-crystalline polymer model that captures volume strain caused by cavitation during deformation. Popa *et al*. (2014) proposed a constitutive model for semi-crystalline polymers featuring a homogenization approach that used representative mesostructure and separate descriptions for crystalline and amorphous phases.

The multiscale aspects of polymer modeling have also seen a significant amount of attention. Bouvard *et al.* (2009) gave an overview of the history of hierarchical multiscale modeling of polymers. A large amount of work has been contributed to multiscale modeling of polymers in recent years as well. Uchida and Tada (2013) developed a multiscale model for semi-crystalline polymers that spanned the micro-meso-macro length scales. This model was able to predict the changes in hardening rate

between stress states (tension, compression, and shear) and account for the changes in modulus and flow stress with increasing crystallinity. Shojaei and Li (2013) developed a multiscale constitutive model for semi-crystalline polymers based on a modified Transformation Field Analysis (TFA) method featuring crystal plasticity for crystalline phases and a viscoelastic model for amorphous phases. Yang *et al*. (2013) used molecular dynamics and continuum micromechanics in a multiscale modeling scheme to examine the performance of carbon nanotube reinforced polymer composites.

Torsional strain hardening has been witnessed in polymers (Tervoort and Govaert 2000; O'Connell and McKenna 2002), yet the differences in mechanical behavior polymers exhibit in different stress states has received far less attention in the modeling community. Bouvard *et al.* (2013) composed an ISV model for glassy polymers that included a "pressure" term from Boyce *et al.* (1988) but was unable to capture the disparity between tension, compression, and torsion at large strains. Arruda *et al.* (1993) investigated separate stress states while studying the effects of initial anisotropy on large strain forming of polymers, but they were constrained to uniaxial compression and plane strain compression. More recently, Anand *et al.* (2009) constructed a polymer material model to capture the micro-indentation behavior of polymers and used compression-tension physical data to calibrate their model. However, they did not calibrate to high tensile strains. Clausen *et al.* (2010) created a material model for thermoplastics that included a term representing the ratio of the tensile and compressive yield stresses for a given polymer. Pouriayevali *et al*. (2013) developed an elastoviscoelastic-viscoplastic constitutive model that predicted polymeric behavior over a range of strain rates for tension and compression. However this constitutive model required a separate set of

calibrate constants for tension and compression. Balieu *et al*. (2013) proposed an elastoviscoplastic constitutive model with fully coupled damage for semi-crystalline polymers. They were able to capture both tensile and compressive behavior of Polypropylene (PP). Poulain, Benzerga, and Goldberg (2014) developed an elastoviscoplastic constitutive model for glassy amorphous polymers. They were able to capture performance variations between different temperatures and strain rates as well as tension and compression for epoxy Epon 862. Hachour *et al*. (2014) performed multiaxial experiments on High Density Polyethylene (HDPE) and was able to model HDPE yield behavior using modified Tresca and von Mises yield surfaces.

While stress state sensitive modeling is in its infancy within the polymeric realm, it has reached a much higher maturity within the metallic community. Prager (1944) and Drucker (1949) first included stress state dependence by including the third invariant of deviatoric stress, J_3, on the yield surface for metals. Horstemeyer *et al.* (1996) and Miller and McDowell (1996) were the first to include the stress state dependence of J_3 into ISV hardening laws for metals. Horstemeyer *et al.* (2000) later modified the Bammann-Chiesa-Johnson (1996) model for metals to capture the metallic hardening rate differences between tension, compression and torsion, as well as damage, by using J_3. They were able to differentiate between stress states using a complex stress function $f(J_2, J_3)$ where J_2 and J_3 ($J_2 = \frac{1}{2}\sigma'_{ij}\sigma'_{ij}$; $J_3 = \det(\sigma')$; $\sigma' = \sigma - \frac{1}{3}\delta_{ij}\sigma_{kk}$) are the second and third invariants of *deviatoric* stress, respectively. The stress function is given by

$$f_{\blacksquare}(J_2, J_3) = a_{\blacksquare}\left[\frac{4}{27} - \frac{J_3^2}{J_2^3}\right] + b_{\blacksquare}\frac{J_3}{J_2^{3/2}} \; ; \; \blacksquare \in \{\alpha, \kappa_1, \kappa_2, g_0, Y\} \tag{3.1}$$

where $a_{\blacksquare}$, and $b_{\blacksquare}$ are material parameters related to a given material's sensitivity to torsion and tension/compression, respectively. The '■' (■ ∈ $\{\alpha, \kappa_1, \kappa_2, g_0, Y\}$) symbol is a placeholder representing the relation upon which the stress function is applied where α, κ_1, and κ_2 are the ISVs, g_0 is an expression within κ_1, and Y is the yield function. The philosophy behind using the stress function in Equation (3.1) is covered in Horstemeyer and Gokhale (1999) and Horstemeyer *et al.* (2000). Further explained in Table 3.1, the stress function (Equation (3.1)) is able to uniquely distinguish the differences between tension, compression, and torsion.

Table 3.1 Stress invariant expressions under different stress states.

	Tension	Compression	Torsion
$\frac{4}{27} - \frac{J_3^2}{J_2^3}$	0	0	$\frac{4}{27}$
$\frac{J_3}{J_2^{3/2}}$	$\frac{2}{3\sqrt{3}}$	$-\frac{2}{3\sqrt{3}}$	0

This investigation seeks to bolster the ISV model for glassy polymers originally proposed by Bouvard *et al.* (2013) via the incorporation of an expanded stress state dependence. The ISV model's stress state dependence will be enhanced by appending instances of the stress function (Equation (3.1)) on to the ISV constructs.

3.2 Internal State Variable Modeling

The ISV constitutive model (Bouvard *et al.* 2013; Francis *et al.* 2014) was developed based upon the original thermodynamic foundation proposed by Coleman and Gurtin (1967). Three ISVs accounted for polymeric internal energy dissipation

mechanisms based on the molecular dynamics studies in Hossain *et al.* (2010). For a comprehensive discussion on the kinematics, kinetics, and thermodynamics of the ISV model presented here, see Francis *et al*. (2014). In sections 3.2.1-3.2.5 the modified polymer ISV model is outlined. Unless otherwise stated, all material parameters are labeled $C_{\#}$ where '#' varies from 1-14. For the ISV model to function all material parameters must be calibrated to the material under consideration.

3.2.1 Stress State Dependence

The stress function ($f(J_2, J_3)$) was included in each ISV (Equations (3.3) and (3.6)), the hardening modulus (g_0) in the first scalar ISV (Equation (3.7)), as well as the yield function (Equation (3.14)). The stress function's ($f(J_2, J_3)$) segments (Table3.1) are what permit stress state sensitivity. The first segment ($4/27 - J_3^2/J_2^3$) acts as a switch for torsion, only having a non-zero value in torsion. Meanwhile the second portion $\left(J_3/J_2^{3/2}\right)$ serves as an activation term for tension and compression. The tension/compression switch takes on positive value in tension, a negative one in compression, and is equal to zero in torsion.

3.2.2 Assumptions

- Plastic flow is incompressible: $|\boldsymbol{F^p}| = 1$, $Tr(\bar{\boldsymbol{L}}^{\boldsymbol{p}}) = \boldsymbol{0}$.
- Plastic flow is irrotational: $\overline{\boldsymbol{W^p}} = 0$.
- Thermal portion of deformation gradient is isotropic: $\boldsymbol{F^\theta} = F^\theta \boldsymbol{I}$, $\overline{\boldsymbol{W^\theta}} = 0$.

3.2.3 Cauchy Stress

The constitutive model consists of two intermediate configurations corresponding to the decomposition of the deformation gradient (Fig. 3.1). All calculations are executed in the first intermediate configuration ($\bar{\boldsymbol{B}}$) and the results are "pushed forward" with the elastic component of the deformation gradient.

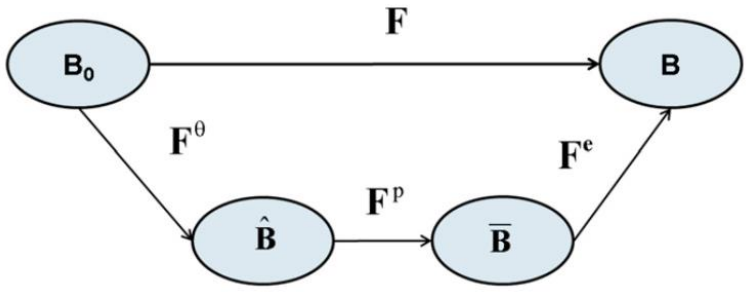

Figure 3.2 Illustration of the glassy polymer Internal State Variable Model deformation gradient decomposition.

The Cauchy stress ($\boldsymbol{\sigma}$) is written in terms of the Mandel stress ($\bar{\boldsymbol{M}}$) where J^e is the Jacobian determinant of the elastic deformation gradient, $\boldsymbol{\tau}$ is the Kirchhoff stress, $\boldsymbol{R}^e$ is the elastic rotation tensor, $\mu(\theta)$ is the shear modulus, $K(\theta)$ is the bulk modulus, $\bar{\boldsymbol{E}}^e$ is the elastic portion of the Green's strain tensor, and θ is the temperature.

$$\boldsymbol{\sigma} = J^{e-1}\boldsymbol{\tau}, \;\; \boldsymbol{\tau} = J^{e-1}\boldsymbol{R}^e\bar{\boldsymbol{M}}\boldsymbol{R}^{eT}, \;\; \bar{\boldsymbol{M}} = 2\mu(\theta)\bar{\boldsymbol{E}}^e + \left[\boldsymbol{K}(\theta) - \frac{2}{3}\mu(\theta)\right] Tr(\bar{\boldsymbol{E}}^e)\boldsymbol{I} \quad (3.2)$$

3.2.4 Internal State Variables (ISVs)

The ISV rate schemes were constructed by modifying the works of Boyce *et al.* (1988) and Ames *et al.* (2009). As previously mentioned ISVs quantify unobservable, internal energy dissipation effects. This constitutive model features three such ISVs.

- The second rank tensorial quantity $\bar{\boldsymbol{\alpha}}$, seen in Equation (3.3) serves to represent large-strain hardening behavior caused by the str*etc*hing of polymer chains.

$$\bar{\boldsymbol{\alpha}} = \hat{\mu}_B(\theta)\bar{\boldsymbol{\beta}};\ \ \hat{\mu}_B(\theta) = \mu_R(\theta)\left[1 - \frac{\lambda_1^{\bar{\beta}} + \lambda_2^{\bar{\beta}} + \lambda_3^{\bar{\beta}}}{\lambda_L}\right]^{-1}\left[1 + f(J_2, J_3)\right] \tag{3.3}$$

$$\dot{\bar{\boldsymbol{\beta}}} = R_{s_1}(\theta)\left(\bar{\boldsymbol{D}}^p\,\bar{\boldsymbol{\beta}} + \bar{\boldsymbol{\beta}}\bar{\boldsymbol{D}}^p\right) \tag{3.4}$$

where $\mu_R(\theta)$ is a temperature dependent rubbery modulus, λ_L is a network locking str*etc*h, $\lambda_i^{\bar{\boldsymbol{\beta}}}$ are the eigenvalues of $\bar{\boldsymbol{\beta}}$, $R_{s_1}(\theta)$ is a temperature dependent material parameter, and $\boldsymbol{D}^p$ is the inelastic rate of deformation. The evolution form of $\bar{\boldsymbol{\beta}}$ is derived from the metallic kinematic hardening relation introduced by Prantil *et al.* (1993) and later modified for polymeric application by Ames *et al.* (2009).

$$R_{s_1}(\theta) = C_{13}\left(\theta - \theta_{ref}\right) + C_{14},\ \ \mu_R(\theta) = C_1\left(\theta - \theta_{ref}\right) + C_2 \tag{3.5}$$

- A pair of scalar-valued ISVs accounting for polymer chain entanglement density as well as polymer chain coiling /alignment:

$$\bar{\kappa}_1 = C_{\bar{\kappa}_1}\mu(\theta)\bar{\xi}_1\left[1 + f(J_2, J_3)\right],\ \ \bar{\kappa}_2 = C_{\bar{\kappa}_2}\mu(\theta)\bar{\xi}_2\left[1 + f(J_2, J_3)\right] \tag{3.6}$$

where the first scalar ISV is defined:

$$\dot{\bar{\xi}}_{\mathbf{1}} = h_0\left(1 - \frac{\bar{\xi}_1}{\bar{\xi}^*}\right)\dot{\bar{\gamma}}^p,\ \ \xi^* = \left(\bar{\xi}_{sat}^* - g_0(\theta)\bar{\xi}^*\right)\dot{\bar{\gamma}}^p,\ \ \bar{\xi}^* = \bar{\xi}_0^*\ at\ t = 0 \tag{3.7}$$

where h_0 and $g_0(\theta)$ are hardening moduli (g_0 being temperature and stress state dependent), $\bar{\xi}^*$ is a temperature dependent strain-like quantity accounting for chain slippage, and $\bar{\xi}_{sat}^*$ is the temperature dependent saturation value for $\bar{\xi}^*$.

$$\bar{\xi}_0^*(\theta) = C_5\left(\theta - \theta_{ref}\right) + C_6,\ \bar{\xi}_{sat}^*(\theta) = C_7\left(\theta - \theta_{ref}\right) + C_8 \tag{3.8}$$

$$g_0(\theta) = \left[C_9\left(\theta - \theta_{ref}\right) + C_{10}\right]\left[1 + f(J_2, J_3)\right] \tag{3.9}$$

The second scalar ISV is defined by:

$$\dot{\bar{\xi}}_2 = h_1\left(\bar{\lambda}^p - 1\right)\left(1 - \frac{\bar{\xi}_2}{\bar{\xi}_{2sat(\theta)}}\right)\dot{\bar{\gamma}}^p,\ \bar{\lambda}^p = \sqrt{\frac{1}{3}tr\left(\bar{\boldsymbol{B}}_p\right)} \tag{3.10}$$

where h_1 is the temperature independent hardening modulus, $\bar{\lambda}^p$ is the effective plastic str*etc*h related to the Cauchy-Green deformation tensor (Ames *et al*. 2009), and $\bar{\xi}_{2_{sat}}$ is the saturation value for $\bar{\xi}_2$.

$$\bar{\boldsymbol{B}}_p = \boldsymbol{F^p F^{pT}},\ \bar{\xi}_{2_{sat}}(\theta) = C_{11}\left(\theta - \theta_{ref}\right) + C_{12} \tag{3.11}$$

3.2.5 Inelastic Rate of Deformation (Flow Rule)

A flow rule is employed to represent viscous flow phenomena rooted in relative polymer chain displacement (Boyce, Parks, and Argon 1988; L Anand and Ames 2006). The "dev" tag refers to the deviatoric portion of a tensor.

$$\dot{\boldsymbol{F}}^{\boldsymbol{p}} = \bar{\boldsymbol{D}}^{\boldsymbol{p}}\boldsymbol{F}^{\boldsymbol{p}},\ \bar{\boldsymbol{D}}^{\boldsymbol{p}} = \frac{1}{\sqrt{2}}\dot{\bar{\gamma}}^p\bar{\boldsymbol{N}}^{\boldsymbol{p}},\ \bar{\boldsymbol{N}}^{\boldsymbol{p}} = \frac{\mathrm{dev}(\bar{\boldsymbol{M}} - \bar{\boldsymbol{\alpha}})}{\|\mathrm{dev}(\bar{\boldsymbol{M}} - \bar{\boldsymbol{\alpha}})\|} \tag{3.12}$$

where $\dot{\bar{\gamma}}^p$ represents the inelastic shear strain rate derived from a modified cooperative model (Richeton *et al*. 2005; Richeton *et al*. 2007), (D. Fotheringham, Cherry, and Bauwens-Crowet 1976; D. G. Fotheringham and Cherry 1978) and $\bar{\boldsymbol{N}}^{\boldsymbol{p}}$ is the direction of viscous flow.

$$\dot{\bar{\gamma}}^p = \dot{\bar{\gamma}}_0^p exp\left(-\frac{\Delta H_\beta}{k_B\theta}\right)\sinh^n\left(\frac{[\bar{\tau} - (Y(\theta) + \bar{\kappa}_1 + \bar{\kappa}_2)]V}{2k_B\theta}\right),\ \bar{\tau} = \frac{\mathrm{dev}\|\bar{\boldsymbol{M}} - \bar{\boldsymbol{\alpha}}\|}{\sqrt{2}}, \tag{3.13}$$

where $\dot{\bar{\gamma}}_0^p$ is a material constant that dictates when the inelastic shear strain rate dependence activates, ΔH_β is an activation energy, k_B is the Boltzmann constant, n is a parameter describing cooperative behavior of polymer chain segments, V is a shear

activation volume, and $Y(\theta)$ is a temperature dependent yield surface also including the stress state dependence,

$$Y(\theta) = \{C_3(\theta - \theta_{ref}) + C_4\}[1 + f(J_2, J_3)] \tag{3.14}$$

The effective shear stress $\bar{\tau}$ (Equation (3.13)) consists of the deviatoric portions of the Mandel stress and the backstress.

3.3 Finite Element Results

3.3.1 Calibration

The ISV model's material parameters were calibrated from physical experimental data from tension, compression, and torsion tests for two materials: Polycarbonate (PC) and Polypropylene (PP). The constitutive relations from the ISV model were ported into a three-dimensional subroutine and incorporated into a Matlab graphical user interface (GUI) to expedite the calibration process. The routine uses a single element finite element simulation for the calibration process. First, the physical experimental data was imported into the Matlab GUI. Then each of the ISV model's parameters were modified until a good "visual fit" was obtained (i.e. the stress-strain curve output from the model becomes very close or collinear with that of the physical experiment(s)). The "fitting" algorithm employs a nonlinear optimization algorithm to minimize the error between the model and experimental data.

Using a *single* set of parameters for each material, the calibration of the ISV constitutive model was able to capture the behavior of both PC (Fig. 3.2) and PP (Fig. 3.3) for all three stress states. The calibrated parameter values are shown for both materials in Appendix A.

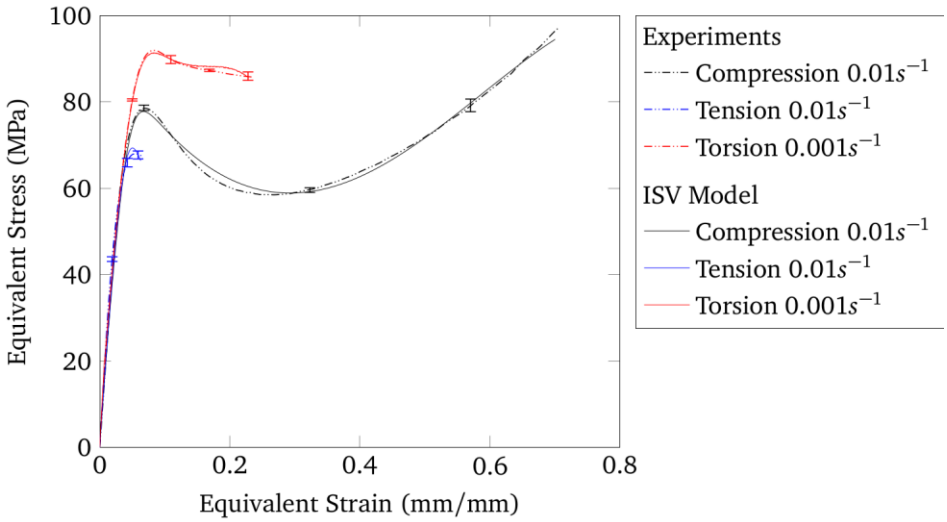

Figure 3.3 True stress-strain internal state variable constitutive model calibration of polycarbonate in three different stress states: tension, compression, and torsion.

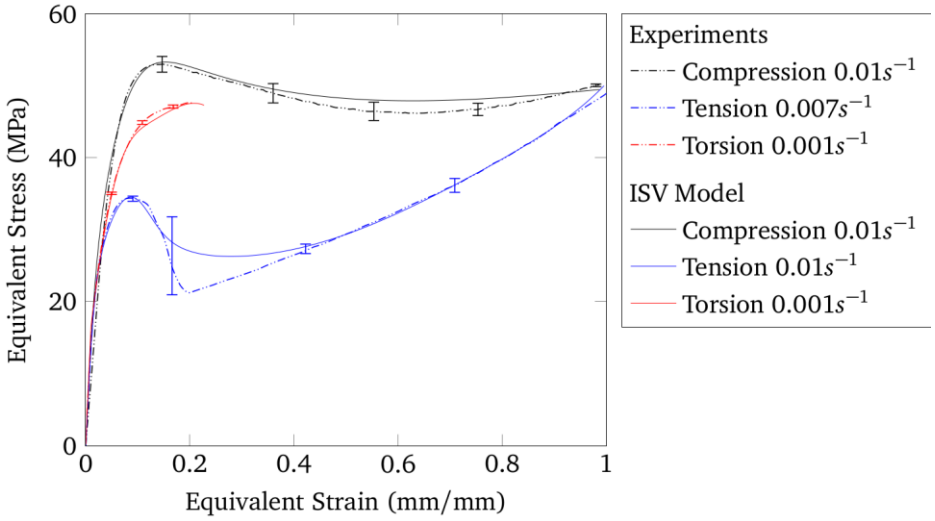

Figure 3.4 True stress-strain internal state variable constitutive model calibration of polypropylene in three different stress states: tension, compression, and torsion.

3.3.2 Validation

3.3.2.1 Experiment

A notched three-point bending problem was chosen to validate the ISV model. We note that calibration includes homogeneous stress/strain states, and validation includes stress and strain gradients, such as those induced by bending. The physical experiment was performed using PP on an Instron 5882 electro-mechanical load frame using a cross head displacement rate of 0.167 mm/s. The test specimen and testing apparatus geometry is shown in Fig. 3.4.

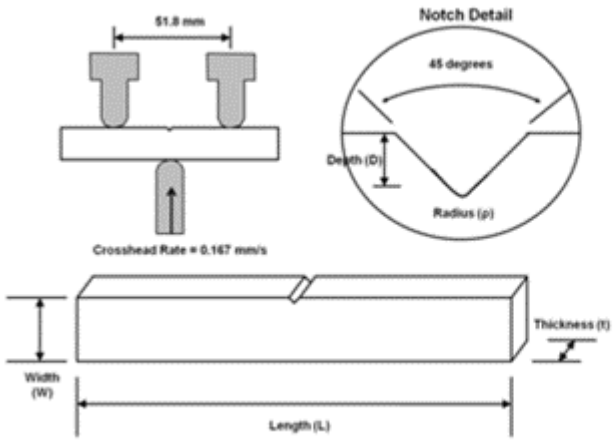

Geometry	Dimension (mm)
L	125
T	3.2
W	12
ρ	0.79
D	~3.5

Figure 3.5 Experimental three-point bending schematic showing specimen dimensions and apparatus setup.

3.3.2.2 Finite Element Simulation

To recreate the three-point bending experiment, the specimen and testing apparatus geometries were imported into ABAQUS finite element code. (Hibbitt 1984) The ISV model was ported into a Fortran subroutine (VUMAT) for explicit FEA. Each

pin was modeled using rigid elements while the bending specimen was modeled with hexagonal brick elements with reduced integration (C3D8R). Contact conditions were established between all pins and the specimen where no penetration was permitted and no friction was applied. A constant displacement rate of 0.167 mm/s was applied to the bottom pin (see Fig. 3.5). The entire setup was split into quarter symmetry to decrease the necessary simulation time. The finite element setup is shown in Fig. 3.6.

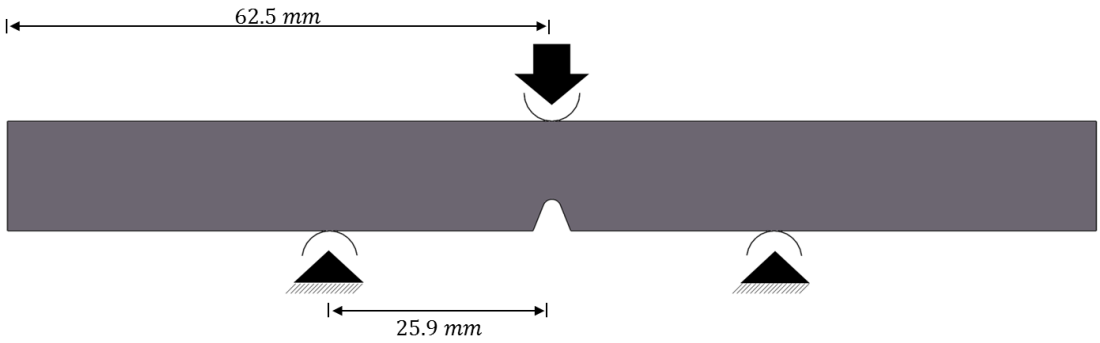

Figure 3.6 Free body diagram for three-point bending finite element simulation. Top pins are held fixed while a displacement is applied to the bottom pin

3.3.2.3 Results

A contour plot of axial stress in the three-point bending specimen is depicted in 3.6. Both tensile and compressive stress states are clearly shown under the bending deformation. Furthermore, Fig. 3.7 displays a force-displacement curve comparing the results from the physical experiment on Polypropylene and that of the simulation. A high level of agreement is achieved by the modified Bouvard *et al.* (2013) model.

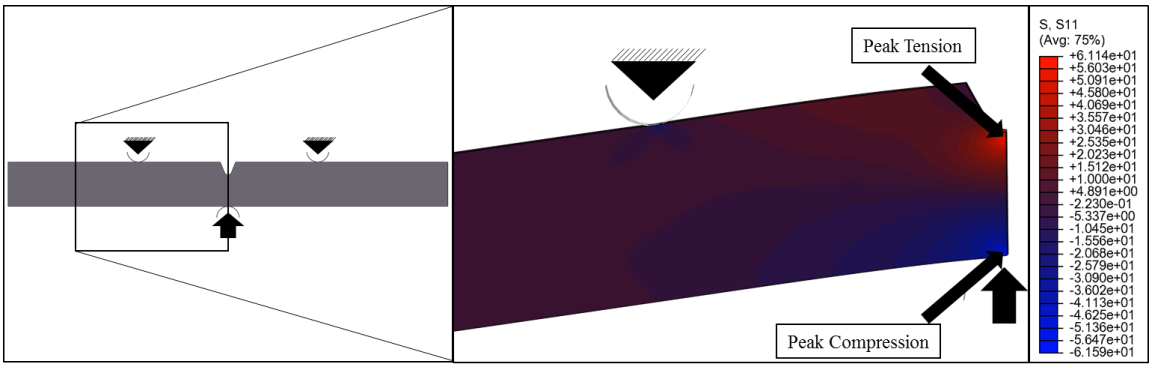

Figure 3.7 Polypropylene three-point bending finite element results showing a contour plot of axial stress.

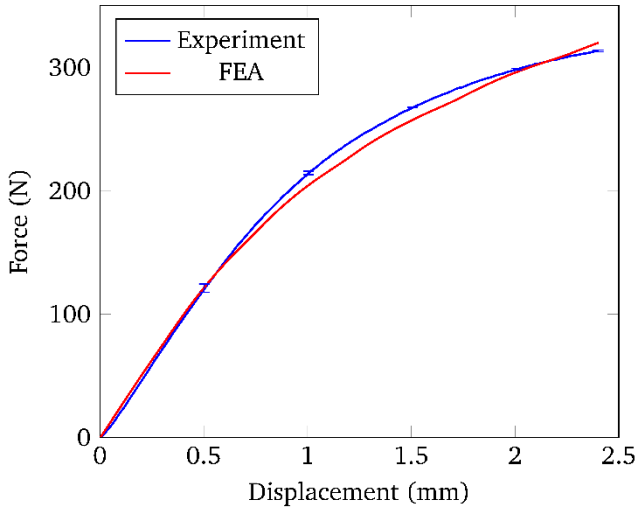

Figure 3.8 Three-point bending force-displacement plot showing the validation showing the finite element results for Polypropylene and the experimental results.

3.4 Conclusions

A method for calculating the elastic-viscoelastic-viscoplastic behavior of glassy polymers has been modified to account for performance variations between tensile, compressive, and torsional stress states. The stress function featuring the second and third deviatoric stress invariants was added to each internal state variable to distinguish hardening with different applied stress states. The modified ISV model was calibrated to

two different thermoplastics and validated against a notched three-point bend test of polypropylene with excellent agreement.

CHAPTER IV

HIERARCHICAL MULTISCALE MODELING AND PARAMETRIC ANALYSIS OF POLYVINYL ALCOHOL/MONTMORILLONITE NANOCOMPOSITES

4.1 Introduction

With the Bouvard ISV model modified in the previous chapter, Chapter 4 focuses on satisfying the downscaled requirements for the dependence of heterogeneities on polymer composite mechanical performance. Polymer nanocomposites represent a composite material subclass that demonstrates significant promise in producing composite materials with remarkable strength to weight ratios, high impact resistances, and rapid fabrication (c.f., Tehrani and Abu Al-Rub 2011).

A polymer nanocomposite is a compound material consisting of a polymeric matrix infused with filler that have at least one dimension on the nanometer scale (Spencer and Sweeney 2008). Nanocomposites featuring nanoclay particles as filler are often referred to as "Polymer/Clay Nanocomposites" (PCN) or "Polymer Layered Silicates (PLS)." Our investigation is concerned with PCN nanocomposites containing reinforcing filler material featuring a plate-like geometry where two of the spatial dimensions are far greater than the third. The large aspect ratio, plate-like, secondary particles are generally referred to as "nanoclay" and exhibit surface areas that are a vast majority of their volume. As such, nanoclay particles typically offer a potent combination of strong elasticity, ample surface area for particle matrix bonding, and very little space

for defects. The thinness of nanoclay particles also results in a constituent filler with very low mass.

Montmorillonite (MMT) from the smectite class of aluminum silicate clays is the most pervasively used nanoclay filler for PCNs today. MMT is a hydrophilic 2:1 phyllosilicate that is easily distributed in water soluble polymers like Polyvinyl Alcohol (PVA) (Carrado, Thiyagarajan, and Elder 1996). The MMT unit crystal comprises a single sheet of aluminum octahedron coated on each side by a layer of silica tetrahedron (Sinha Ray, Bousmina, and Maazouz 2006). MMT are typically around 1 nm thick and have a length and width that can vary from a few nanometers to over a micron (Pavlidou and Papaspyrides 2008; McNally *et al*. 2003). The silicate layers often form lamellar structures with a very regular van der Waals gap that can be infiltrated by polymers during the fabrication process (Sapalidis, Katsaros, and Kanellopoulos 2011).

The matrix of the nanocomposite described herein is PVA, which is a biocompatible, biodegradable, and water soluble polymer produced through the hydrolysis of Polyvinyl Acetate (Hay and Lyon 1967). These characteristics make PVA useful in biomedical devices (Kobayashi, Toguchida, and Oka 2003) or drug delivery systems (Brazel and Peppas 1999). However, PVA also suffers from low strength and poor heat resistance thus fillers (i.e. MMT) are often added to PVA to improve its properties (Sapalidis, Katsaros, and Kanellopoulos 2011).

4.1.1 Polymer/Clay Nanocomposite Morphology

Introducing MMT nanoclay particles or other “planar” reinforcements into a polymer host can result in different substructures and morphological states. The resulting morphological states include:

- Agglomerated: large quantities of the nanoclay filler pile up that form larger effective particles (Alexandre and Dubois 2000).
- Exfoliated: individual nanoclay sheets are substantially separated from each other, and are misaligned with respect to neighboring nanoclay sheets. In the exfoliated state, the matrix-inclusion interaction benefits are at a maximum (Chin *et al*. 2001; Varlot *et al*. 2001).
- Intercalated: polymer chains are able to enter the gallery spacing causing a lamellar lattice expansion. Nanoclay layers will typically remain "stacked" and parallel relative to each other.

Images from Transmission Electron Microscopy (TEM) (Sheng *et al*. 2004; Wang *et al*. 2005; Song *et al*. 2013; Song *et al*. 2014) and Atomic Force Microscopy (AFM) (Ploehn and Liu 2006) have revealed that PVA/MMT nanocomposites contain heterogeneous distributions of agglomerated clumps, exfoliated sheets, and intercalated lamellar nanoclay structures in different regions (Strawhecker and Manias 2000). Fig. 4.1 shows a TEM image identifying each of the three PCN states along with a highlighted intercalated structure which was used as a template for the idealized finite element lamellar structures discussed in Section 4.4.

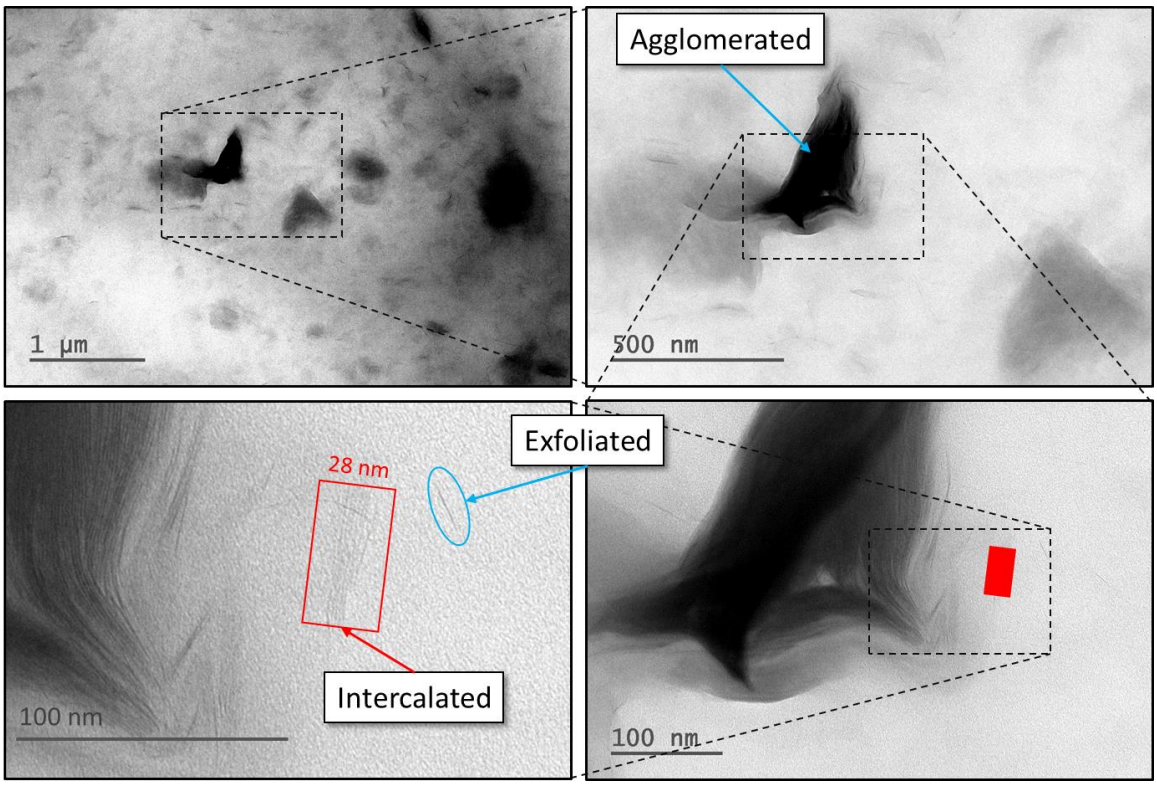

Figure 4.1 Transmission Electron Microscopy (TEM) images of Polyvinyl Alcohol (PVA) with 5 vol% Montmorillonite (MMT) showing a variety of nanocomposite formation states.

Note the agglomerated region, intercalated region, and exfoliated region. The red box indicates an intercalated lamellar structure that is the basis for this investigation

In this research our focus is on the delamination of the intercalated lamellar nanoclay structures, since delamination of nanoclay sheets from the polymer matrix is the primary source of inelasticity in PCNs (Wang *et al*. 2005).

Introducing small quantities of MMT (1%-5%) within a PVA host can result in a significant improvement in the elastic modulus, yield stress, and tearing energy of PVA (Strawhecker and Manias 2000; Lee *et al*. 2009; Soundararajah, Karunaratne, and Rajapakse 2009; Song *et al*. 2013; Song *et al*. 2014; Allison *et al*. 2015). Fig. 4.2 (Allison *et al*. 2015) contains data from physical tensile experiments on pure PVA and 1%

PVA/MMT thin films. The inclusion of MMT boosts the elastic modulus of PVA by 53% and the yield strength by 45%.

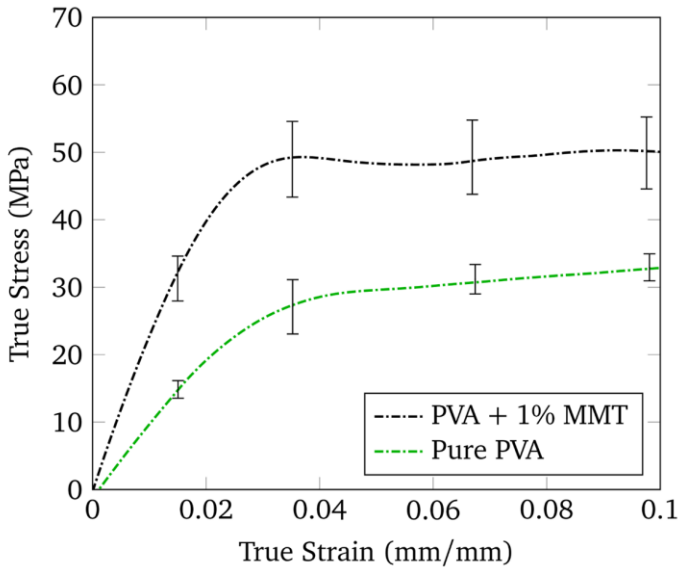

Figure 4.2 True stress-strain tensile behavior of pure Polyvinyl Alcohol (PVA) and a 1% volume fraction PVA/Montmorillonite nanocomposite strained at 0.0007 s^{-1} (Allison *et al*. 2015).

4.1.2 Polymer/Clay Nanocomposite Fracture

Fabrication of PCNs is complex, often resulting in poor bonding between the nanoclay particles and polymer matrix. Furthermore, silicate interlayer gallery spacing is generally too small for a sufficient amount of polymer chains to penetrate and form bonds. Kim *et al.* (2001) investigated the influence of nanoclay particles on the deformation mechanisms in polyamide-12/nanoclay composites, and determined that microvoids from between silicate layers arise from debonding between the silicate layers and the polymer matrix. Gam *et al.* (2003) examined the fracture behavior of core-shell-rubber-modified clay/epoxy nanocomposites and found that debonding of intercalated

nanoclay layers followed by extensive matrix shear banding were the main failure mechanisms. Wang *et al.* (2005) used TEM on subcritically loaded epoxy/nanoclay composite test specimens and concluded that microcracks nucleated within the gallery zones in between intercalated nanoclay layers. These microcracks coalesce and result in delamination of nanoclay particles from the epoxy.

4.1.3 Polymer/Clay Nanocomposite Modeling

A considerable level of research effort has been dedicated to developing computational strategies to deal with the complexities of modeling PCNs over the last half century. Adams (1970) conducted a two-dimensional, plane strain FEA of anisotropic fiber composites under transverse normal loading, and discovered that composites undergo a significant amount of local yielding and stress redistribution without significant fluctuation in the overall stress-strain behavior. Lin *et al.* (1972) performed plane strain finite element calculations on anisotropic boron/aluminum and boron/epoxy fiber composites under longitudinal loading, and learned that the ultimate strength of a composite depends not only on the tensile strength of the constituents, but also on their associated elastic moduli and ductility. Newaz (1986) determined that analytical models could only provide a Young's modulus for polyester/clay composites due to the heterogeneous structure. Sheng *et al.* (2004) introduced an "effective particle" for lamellar structures into a two-dimensional micromechanical framework to simulate the elastic behavior of PCNs. Spencer and Sweeney (2008) performed two dimensional FEA on PCNs featuring both straight and curved nanoclay particles within the polymer matrix, and discovered that while the PCN stiffness rose with filling fraction, the level of stiffness enhancement decreased and eventually saturated as the amount of intercalation

increased. The saturation suggests that the internal nanoclay layers were "shielded" from load transfer from the matrix at a certain strain level. Tehrani and Abu Al-Rub (2011) used a viscoelastic-viscoplastic-viscodamage constitutive model to simulate PMMA/nanoclay composites under two-dimensional uniaxial compressive loading. The study showed that the addition of small amount of nanoclay particles greatly enhanced the mechanical performance of the pure polymer.

While the bulk of the PCN modeling effort has been focused on two-dimensional frameworks, colossal growth in computational power coupled with novel methods for characterizing and recreating PCN nanostructures have allowed researchers to explore PCN performance using three-dimensional frameworks. Chawla *et al.* (2006) used a serial sectioning procedure to recreate realistic three-dimensional silicon carbide reinforced aluminum microstructures and performed FEA on those microstructures determining that structures regenerated from serial sectioning produced more accurate results than both analytical models and idealized geometries. Wang *et al.* (2011) performed three-dimensional FEA on nanocomposites using an effective interface model to investigate the nanocomposite's elastic response. The effective interface model featured a stiff outer layer and a soft inner layer. The study found that if the composite interface stiffness was less than that of the matrix, then the composite's mechanical performance would rise with particle size. However in the opposite scenario the relationship was reversed. Song *et al.* (2013) performed FEA on three-dimensional representative volume elements (RVEs) of epoxy/nanoclay composites showing that the interlayer gallery strength played a significant role in the mechanical performance of PCNs. Song *et al.* (2014) performed FEA on three-dimensional RVEs of nylon

6/nanoclay composites showing that a multiscale modeling method where interface properties are determined by MD can be effective tools for simulating PCNs. Further reading can be found in PCN review articles by Valavala and Odegard (2005) and Hu *et al.* (2010).

The complex geometry of PCNs (Section 4.1.2) dictates the need for an algorithm to construct virtual representations of PCN nanostructures in order to build FEA models. In this present work, we designed a Virtual Composite Structure Generator (VCSG) algorithm based on a modified Random Sequential Absorption (RSA) technique as described by Spencer and Sweeny (2008) to generate random PCN morphology realizations. Each realization consisted of four material definitions: matrix (PVA), inclusions (MMT), interphases (PVA), and interlamellar galleries (PVA). A Cohesive Zone Model (CZM) (Dugdale 1960; Barenblatt 1962) based on a Traction-Separation (T-S) rule (Section 4.3.1) controlled the behavior of both the interphases and interlamellar galleries. Details on the PCN simulation structure can be found in Section 4.4.2.

Since delamination is the primary mode of deformation in PCNs, a CZM simulated the PVA/MMT interface behavior. The aforementioned CZM employed a T-S rule (Section 4.3.1) calibrated with the results of Molecular Dynamics (MD) simulations of a PVA/MMT interface (Lawrimore II *et al*. 2016b; Paliwal *et al*. 2016) for both the interphase and the gallery regions. Simulating damage progression/decohesion at interfaces with a T-S rule has been widely used in the literature (Needleman 1987; Needleman 1990a; Needleman 1990b; Viggo Tvergaard and Hutchinson 1992; Xu and Needleman 1993; Viggo Tvergaard and Hutchinson 1996; Camacho and Ortiz 1996; Bigoni, Ortiz, and Needleman 1997; Tay *et al*. 1999; Alfano and Crisfield 2001; Espinosa

and Zavattieri 2003; J. L. Bouvard, Chaboche, *et al*. 2009; Song *et al*. 2014). Additionally see Park and Paulino (2013) for a detailed review on the use of T-S rules within CZMs.

Most of the existing research in the PCN computational realm employs analytical, empirical, or simple viscoelastic-viscoplastic material models to simulate the polymeric response under loads. Based on the work first proposed by Coleman and Gurtin (1967) and Rice (1971), the investigation presented here used a physically-based, temperature sensitive elastoviscoelsatic-viscoplastic ISV model (J. L. Bouvard *et al*. 2013) calibrated to physical experimental data to simulate the mechanical response of PVA. Section 5.1.3 contains further details on the ISV model used in this work.

The earliest works that relate statistical procedures to physical experiments are attributed to Fisher (1935a, b). As a result of his work, statisticians used several analysis of variance techniques to interpret physical experimental data (Box *et al.* 1978). Taguchi (1974, 1986, 1987) popularized the DOE method for use in quality-engineering. In the present DOE study, the 'experiments' are not physical but numerical in nature. Briefly, the DOE method uses a tri-level geometric array of unique condition combinations to extract the influence of parameters that are most critical to a particular result. For example, Horstemeyer *et al.* (1999) implemented a DOE method into a mesoscale crystal plasticity framework to understand the relative macroscale effects of a variety of mesoscale constitutive models on the behavior of FCC metals. The study concluded that intergranular constraints and kinematic hardening were much more influential than the type of constitutive model used. Gall *et al.* (2000) used two-dimensional mesoscale finite element analysis within a DOE framework to investigate the effects matrix-particle

morphology on the fracture and debonding of silicon particles enclosed within a aluminum matrix. The study identified the temperature as the critical parameter for the fracture and debonding of silicon particles. For analyzing void growth and coalescence in different metal alloys, Horstemeyer and Ramaswamy (2000c) examined different variables and showed that temperature and microporosity played the most dominant roles. Later, Horstemeyer *et al.* (2003) conducted finite element simulations guided by a DOE matrix to quantify the relative influence of different parameters on void nucleation. Wang *et al.* (2009) used the DOE technique coupled with crystal plasticity in mesoscale finite element simulations to determine that the remote applied displacement is the most important influence parameter affecting fatigue crack incubation in a 7075 aluminum alloy when compared to some microstructural features. Lawrimore *et al*. (2016a) employed a DOE method to discern that a polymer's stress state was the most influential parameter affecting damage growth and coalescence. These different DOE studies have shown in some cases that the mechanics issues are more important, but in others the microstructural morphology is more important, each depending on the variables and metrics of interest.

Another issue that we must consider is the uncertainty that can arise from physical experiments (extrinsic) and computational methods (intrinsic) as illustrated in Fig. 4.3. The subject of uncertainty is mostly absent from the computational realm; however, recently Acar and Solanki (2008) quantified uncertainty in designing vehicles for crashworthiness and Hughes *et al*. (2014) was able to quantify the uncertainty of data bridged from the electronics scale to calibrate an interatomic potential within the Modified Embedded Atom Method (MEAM) (Baskes 1987).

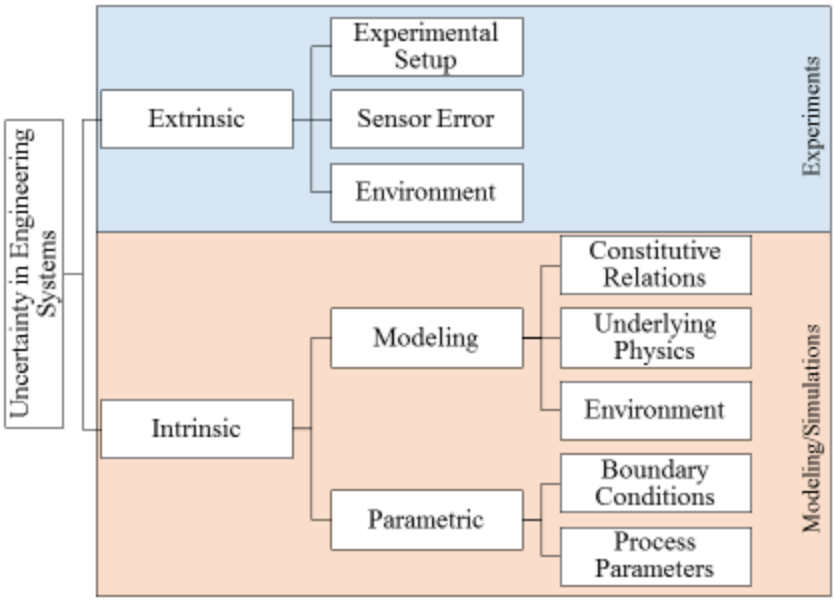

Figure 4.3 Schematic demonstrating hierarchy of uncertainty across engineering systems (Coleman and Steele 1999).

This endeavor seeks to use three-dimensional FEA of periodic PVA/MMT RVEs cast in a DOE framework to expose the parameter(s) most crucial to enhancing the elastic modulus and yield strength in PCNs. The DOE method used in this study consists of four parameters related to PCN inclusions: MMT aspect ratio, MMT orientation, PVA intercalation, and intralamellar PVA gallery strength. RVE's were produced via the VCSG (Lawrimore *et al.* 2016b) and featured a physically-based, rate and temperature dependent ISV model to simulate the behavior of PVA as well as a Cohesive Zone Model (CZM) to govern the behavior of PVA/MMT interfaces. A metamodel trained with the FEA stress-strain response data and cast in a Monte Carlo framework produced a quantified uncertainty for the multiscale modeling methodology discussed in this work.

4.2 Molecular Dynamics of Polymer/Clay Nanocomposites

In this section, we briefly establish the MD methodology employed to extract the bridging information between cohesive traction and crack-opening displacement for PVA/MMT nanocomposites. The endeavor is covered in full detail in Paliwal *et al.* (2016). The work consists of tensile MD calculations that simulated the PVA/MMT debonding process over several representative PVA/pyrophillite-clay (aluminum silicate hydroxide - $Al_2Si_4O_{10}(OH)_2$, analogous to MMT) interfacial structures at ambient temperatures. A T-S rule was mapped to the results from the range of atomistic simulations for subsequent use in characterizing the interfacial load transfer in higher length scale finite element simulations.

The "Large-scale Atomic/Molecular Massively Parallel Simulator" (LAMMPS) distributed by Sandia National Laboratories (Plimpton 1995) was used to perform all MD simulations. An explicit, all-atom, Polymer Consistent Force-Field (PCFF) represented atomic interactions within PVA, while an interatomic potential, based on PCFF and developed by Heinz *et al.* (2005), modeled the atomic interactions of MMT. In each MD calculation, both the amorphous PVA and the pyrophylllite clay substrates were relaxed and equilibrated at room temperature. Several PVA configurations were constructed with each having a specific number of polymer chains and monomer units per chain. Periodic boundary conditions were applied along the interfacial plane to account for the large length of the clay particles. Tensile separation was described by the orthogonal relative motion of the phases along the interface. The simulation box contained a fixed pyrophyllite clay layer at the bottom and a constrained layer of PVA at the top for applying loads (Fig. 4.4). Mode I decohesion behavior was examined by subjecting the

constrained PVA layer to tension until the mobile PVA portion (sandwiched between the constrained PVA layer and fixed clay layer) experienced complete separation and the system's normal traction disappeared.

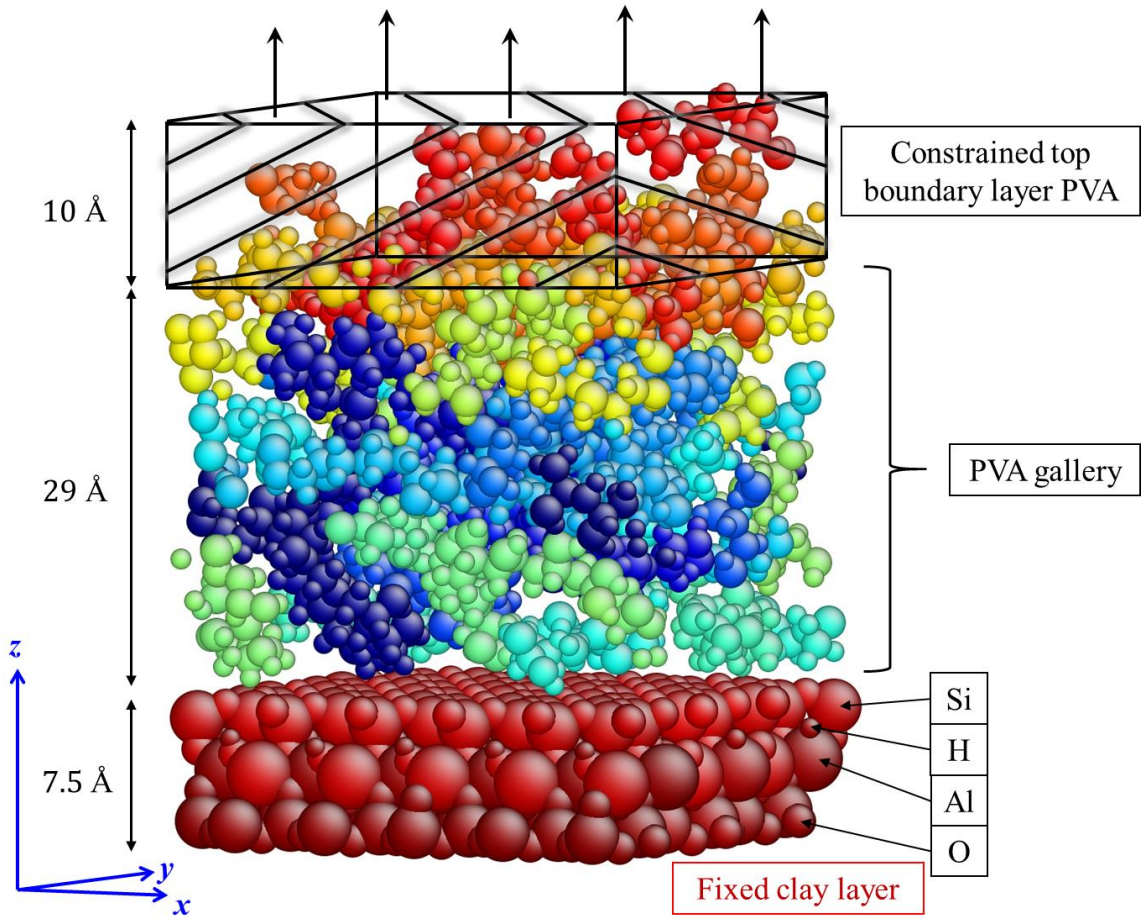

Figure 4.4 Initial structure and boundary conditions of Molecular Dynamics (MD) simulations of the Polyvinyl Alcohol (PVA)/Pyrophyllite interface.

The fixed clay layer is the pyrophyllite region, and the many-colored middle region is the PVA.

The cohesive (and subsequent decohesion) behavior only involved non-bonded van der Waals and electrostatic interactions both among the polymer chains as well as between the polymer and clay. None of the atomistic simulations contained covalent

bonding between the clay substrate and the polymer. To examine the strain rate sensitivity, MD calculations for the PVA/pyrophyillite clay interfaces were perfromed at four strain rates: $10^6 s^{-1}, 10^7 s^{-1}, 10^8 s^{-1}$, and $10^9 s^{-1}$. In the model, a single chain of PVA included 360 monomer units. Mode I tractions and separation distances were quantified for the duration of each simulation and are displayed in Fig. 4.8 also shows that the effect of the applied strain rate on the debonding of PVA/pyrophyllite clay is insignificant since the interaction between the constituents is governed by van der Waals and electrostatic forces, which are typically insensitive to strain rate.

4.3 Upscaling Molecular Dynamics Results

This investigation seeks to establish a Cohesive Zone model (CZM) calibrated to atomistic simulations of an interface between PVA and MMT in order to define the criteria mesoscale delamination between layers of MMT within PVA. During the last decade, a considerable amount of effort has been put toward development of multiscale bridging methods to calibrate mesoscale or higher CZMs though atomistic simulations. Gall *et al.* (2000) showed that mathematical forms of continuum scale cohesive laws were compatible with Modified Embedded Atom Method (MEAM) atomistic simulation results between biomaterials (aluminum and silicon). Yamakov *et al.* (2006) used MD simulations to isolate a T-S rule for grain boundary crack propagation in aluminum. Glaessgen *et al.* (2006) parameterized a CZM for finite element simulations of aluminum polycrystals using atomistic simulations of separation along grain boundaries. Zhou *et al.* (2008) used MD simulations of an interface between two brittle BCC materials to quantify a T-S relation employed in a cohesive surface constitutive model. Yamakov *et al.* (2008) formulated a T-S rule for finite element simulations though MD simulations of

grain-boundary debonding during intergranular fracture in fine grained aluminum. Stoilov (2008) used atomistic simulation of a NiTi system featuring a Helmholtz free energy interatomic potential to derive parameters for a continuum model for NiTi systems. Zhou *et al.* (2009) calibrated a T-S rule using MD simulations of interfaces between two brittle materials under mixed loading. Dandekar and Shin (2011) performed MD simulations on an aluminum-silicon carbide interface to calibrate a T-S relation within a finite element framework for high strain rate loading.

4.4 Metrics

A statistical confidence interval (Coleman and Steele 1999) provided a means to assess the uncertainty related to the PVA/MMT stress-strain data shown in Fig. 4.2. The data corresponding to the PVA + 1% MMT nanocomposite corresponds to three separate experiments. Since the data was sparse, the authors assumed the experimental data adhered to a normal distribution. The normal distribution confidence interval was obtained from

$$\bar{x} - t_{\alpha,\upsilon}\frac{S_x}{\sqrt{N}} \leq \mu \leq \bar{x} + t_{\alpha,\upsilon}\frac{S_x}{\sqrt{N}} \tag{4.1}$$

where $\bar{x}$ is the mean of the sampled data, S_x is the standard deviation of the sampled data, N is the number of samples, and $t_{\alpha,\upsilon}$ is an expansion factor for the sample standard normal distribution for α (1%, 5%, or 10% most commonly) level of significance, and υ degrees of freedom. Statistically, Equation (4.1) captures $(1-\alpha)$% of experimental observations. Uncertainty ranges calculated with Equation (4.1) are displayed in Fig. 4.5 for PVA +1% MMT.

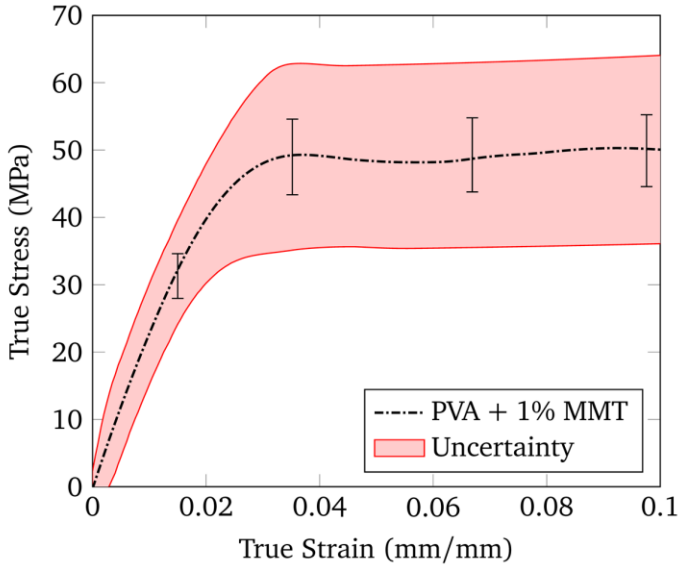

Figure 4.5 True stress-strain behavior exhibiting tensile experimental data for pure Polyvinyl Alcohol (PVA) and PVA + 1% Montmorillonite along with their associated uncertainty bands.

This work was focused on quantifying the relative MMT parametric influence on the mechanical performance increase shown in Fig. 4.2 Thus elastic modulus and yield strength constituted the metrics by DOE parameters were examined. Elastic moduli were calculated using the linear portions of resultant stress-strain responses. Since yield strength is not well defined in the PCN community, we selected the stress at a 0.02 % strain offset as the yield stress according to standard ASTM D638.

4.5 Parameters

According to Sapalidis *et al*. (2011) there are four crucial parameters that determine the properties of PCN: inclusion aspect ratio, inclusion intercalation/dispersion, inclusion orientation/alignment, and polymer/nanoclay interface behavior. The internal mechanisms of PVA are captured with a physically-based ISV

polymer model so only polymer-inclusion interfaces are explicitly examined. Table 4.1 contains the set of parameter levels used in the DOE parametric study.

Table 4.1 Parameter levels featured in the Design of Experiments (DOE) parametric study.

	Level 1	Level 2	Level 3
Aspect Ratio	100	400	800
Orientation	0^o	90^o	180^o
Intercalation	3	6	10
Gallery Strength	20 MPa	60 MPa	100 MPa

Note that 'intercalation' refers to the number of nanoclay layers used in intercalated lamellar clusters and 'gallery strength corresponds to percentages of the maximum traction used in the Traction-Separation (T-S) rule.

4.5.1 Aspect Ratio

All MMT inclusions had a predefined thickness of 1 nm obtained through observation of TEM (Sheng *et al*. 2004; Song *et al*. 2013; Song *et al*. 2014). Furthermore. Ploehn and Liu (2006) used Atomic Force Microscopy (AFM) to show that MMT was typically very round. Thus, all MMT inclusions were defined to be round disks with 1 nm thickness. In an idealized case, high geometric aspect ratio (L/t) inclusions are optimal as reinforcing agents since their volume is almost all surface area (Shepherd, Golemba, and Maine 1973). Song *et al*. (2013) used FEA to show that increasing the aspect ratio of nanoclay inclusions within epoxy resulted in a corresponding increase to the PCN elastic modulus and tensile strength. Song *et al*. (2014) demonstrated that as the aspect ratio of nanoclay inclusions rose, both the elastic modulus as well as the yield stress of nylon 6/clay composites increased. In addition planar reinforcements have been reported to have diameters anywhere between a few nanometers and multiple microns (Pavlidou and Papaspyrides 2008; Sapalidis, Katsaros, and Kanellopoulos 2011); hence, this work

(Table 4.1) features a large range of aspect ratios $(100 - 800)$ to quantify the influence of very high aspect ratio nanoclay particles on PCN performance.

4.5.2 Orientation

Analogous to fiber composites, the orientation of planar inclusions has a significant effect on the resulting mechanical performance of PCNs. When platelets are near orthogonal to the loading axis, far less stress is transferred into the clay layers than when they are aligned in a parallel manner (Spencer and Sweeney 2008). When clay layers are misaligned from the loading axis, much more of the system's stress is contained within the much weaker polymer host, resulting in weaker performance. In this investigation, the 'orientation' parameter refers to a bound on the uniform distribution of random orientations assigned during VCSG. Three Euler angles selected at random within the bound set by the orientation parameter served to describe the three dimensional orientation of intercalated lamellar structures within RVEs. For example, an orientation of 90^o meant that during VCSG, intercalated lamellar structures were assigned three random Euler angles between 0^o and 90^o corresponding to rotations around each Cartesian axis. An orientation of 0^o referred to intercalated structures aligned to the loading axis and an orientation of 90^o referred to those that were orthogonal to the loading axis. The authors chose a $[0^0 - 180^o]$ range (Table 4.1) for the orientation parameter in order to capture all orientation effects on PCN behavior.

4.5.3 Intercalation

The 'intercalation' parameter controls the number of MMT nanoclay layers used in the intercalated lamellar clusters within a given DOE simulation. The amount of

'stacking' is directly related to overall performance of PCNs. Sheng *et al*. (Sheng *et al*. 2004) demonstrated using an 'effective particle' to model intercalated lamellar clusters within a polymer matrix that as intercalation increased, the overall strength of the effective particle decreased. Spencer and Sweeney (2008) used two-dimensional finite element simulations to show that independent of inclusion filling fraction, as intercalation increased the overall stiffness of the composite material decreased due to internal nanoclay layers being shielded from stress**.** Tehrani and Abu Al-Rub (2011) showed that the resulting toughness enhancement when nanoclay was added to Polymethyl Methacrylate Polymer (PMMA) was much higher in the case where the nanoclay was exfoliated as opposed to the case where it was intercalated. Since nanoclay are around 1 nm in thickness (Pavlidou and Papaspyrides 2008; McNally *et al*. 2003) and PCN intercalated lamellar structures have a very regular gallery spacing around 3 nm (Alexandre and Dubois 2000; Beyer 2002; McNally *et al*. 2003), the present study employs intercalated lamellar structures with 1 nm thick nanoclay layers and 3 nm interlayer gallery spacing. Table 4.1 shows the range of intercalation examined in this study.

4.5.4 Gallery Strength

As exposed by Wang *et al*. (2005), PCN intercalated lamellar galleries contain a significant amount of initial microporosity due to the host polymer's inability to adequately penetrate the lamellar lattice. The endeavor goes on to demonstrate that as the PCN is loaded, the initial voids grow and coalesce within the gallery layers comprising the polymer before propagating to neighboring intercalated structures. The initial microporosity combined with the complex stress state experienced by the gallery polymer

due to the presence of nanoclay particles likely exacerbates damage progression (Lawrimore *et al*. 2016a). Since initial microporosity cannot yet be quantified, our work explored a wide range of gallery strengths (Table 4.1) represented in a T-S rule (Section 4.3.2). Different amounts of microporosity would change the gallery strength levels; hence, we chose percentages of the maximum traction for the T-S rule used to model interfaces within the RVEs.

4.6 Finite Element Analysis

4.6.1 Internal State Variable Model

All FEA computations utilized a physically-based, rate and temperature dependent ISV model for polymers developed by Bouvard *et al.* (2013) to simulate the behavior of PVA. A three-dimensional material point simulator provided an efficient means to calibrate the ISV model to physical quasi-static tensile experiments of pure PVA. The constitutive model features three ISVs to account for inelastic dissipation mechanisms in polymers.

- $\bar{\xi}_1$ is a strain-like scalar that accounts for dissipation induced from polymer chain entanglement points.
- $\bar{\xi}_2$ is a strain-like scalar that represents material hardening resulting from polymer chain alignment and uncoiling at large strains.
- $\bar{\boldsymbol{\alpha}}$ is a strain-like tensor that accounts for hardening induced by polymer chain orientation and str*etc*hing at large strains.

Fig. 4.6 shows the physical tensile stress-strain data for pure PVA along with the corresponding ISV model calibration. Additionally, Appendix A contains an outline of the calibrated ISV parameters.

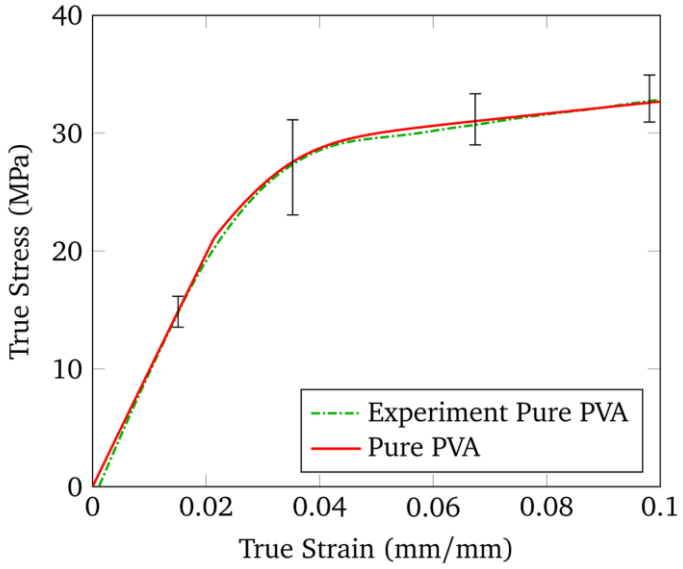

Figure 4.6 True stress-strain behavior displaying the polymer Internal State Variable (ISV) model calibration with pure Polyvinyl Alcohol (PVA) tensile data at a strain rate of 0.0007 /s.

4.6.2 Virtual Composite Structure Generation

The complex nature of the nanostructure associated with PCNs necessitates a systematic method for producing RVEs with which to investigate PCN mechanical behavior. Thus, we developed an algorithm capable of producing unique, three-dimensional RVEs featuring random assortments of nanoscale inclusions within a matrix host subject to user input. The VCSG algorithm (Lawrimore II *et al*. 2016b) applied RSA and interference detection to assemble a collection or nonintersecting, randomly oriented, and randomly positioned inclusions within a specified cubic matrix. A supplementary Python code ported RVEs into Abaqus 6.14 for explicit FEA. For a detailed overview of the VCSG algorithm, see Appendix B.

4.6.3 Cohesive Zone Model

A CZM was used to control delamination of MMT sheets from the PVA matrix via a T-S rule calibrated with results from lower length scale MD calculations (Lawrimore *et al.* 2016b; Paliwal *et al.*, 2016). For this investigation, the VCSG created a range of RVEs featuring MMT in intercalated lamellar structures distributed within a PVA matricies. For simplicity, the present study treated both the gallery and interphases as cohesive interfaces with finite thickness (Song *et al*. 2013; Song *et al*. 2014). Table 4.7 contains a sample intercalated structure showing MMT as well as a cohesive interphase and gallery zones stacked in a regular manner. Depending on which DOE simulation was under consideration, each lamellar structure consisted of N_{MMT} nanoclay layers, $N_{MMT} - 1$ cohesive gallery layers in between layers of nanoclay, and a pair of cohesive boundary interphase regions. All interphases, galleries, and nanoclay particles had equivalent predefined thicknesses (4.2) obtained from TEM (McNally *et al*. 2003; Sheng *et al*. 2004; K. Wang *et al*. 2005; Pavlidou and Papaspyrides 2008; Song *et al*. 2013; Song *et al*. 2014) and AFM (Ploehn and Liu 2006) observations.

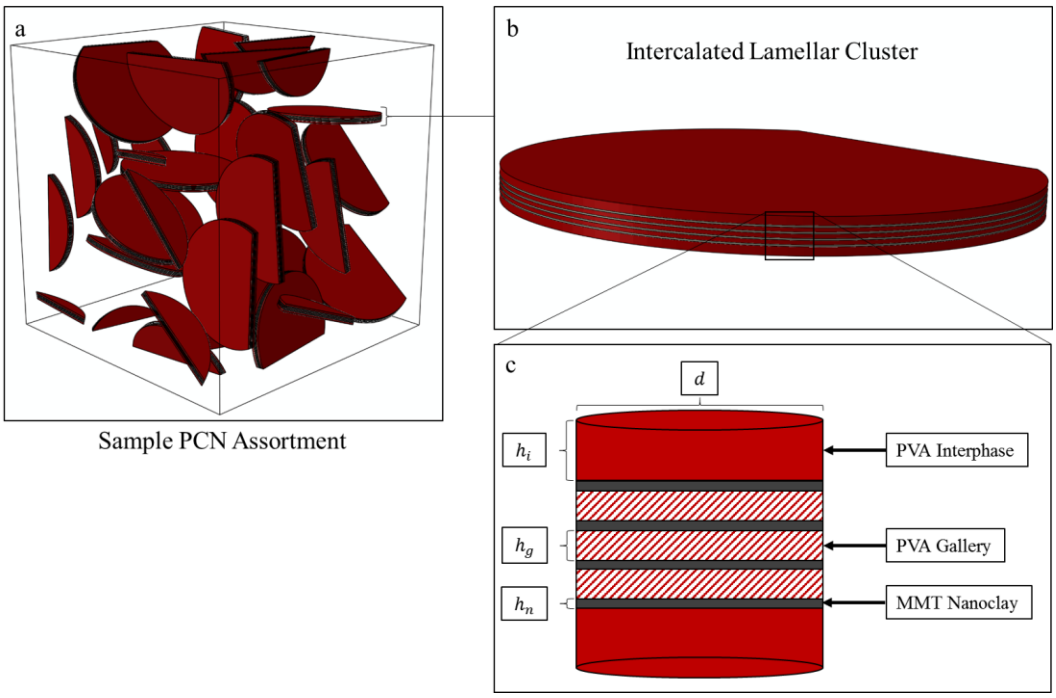

Figure 4.7 Sample Polymer/Clay Nanocomposite (PCN) schematic showing (a) an entire Representative Volume Element (RVE) created by the Virtual Composite Structure Generator (VCSG), (b) a single intercalated lamellar structure, and (c) a detailed view of the lamellar dimensions and arrangement.

Table 4.2 Parameter values for intercalated polymer/clay nanocomposite lamellar structures.

Parameter	Value
h_i	6 nm
h_g	3 nm
h_n	1 nm

4.6.4 Traction-Separation

This work employs a T-S formulation built into the FEA code Abaqus 6.14 (Hibbitt 1984). The three-dimensional uncoupled elastic tractions for cohesive elements are given by:

$$\underline{t} = \begin{Bmatrix} t_n \\ t_s \\ t_t \end{Bmatrix} = \begin{bmatrix} E_{nn} & & \\ & E_{ss} & \\ & & E_{tt} \end{bmatrix} \begin{Bmatrix} \epsilon_n \\ \epsilon_s \\ \epsilon_t \end{Bmatrix} = \underline{\boldsymbol{E}}\,\underline{\epsilon};\ \ \epsilon_x = \frac{\delta_x}{T_0}\ \forall x \in \{n, s, t\} \tag{4.2}$$

where $\underline{t}$ and $\underline{\epsilon}$ are the traction and strain vectors with components in the normal and two shear directions with respect to an interface; $\underline{\boldsymbol{E}}$ is the tractional stiffness tensor; δ_x is the displacement in the normal or one of the two shearing directions (depending on x); and T_0 is the initial thickness of the cohesive element for which the traction is calculated. The purpose of a T-S law is to model a progressive degradation of a cohesive element's stiffness. To accomplish this, a scalar damage parameter ϕ is defined by the following,

$$\phi = \left\{\frac{\delta_{eff}^0}{\delta_{eff}^{max}}\right\}\left\{1 - \frac{1-\exp\left[-\alpha\left(\frac{\delta_{eff}^{max}-\delta_{eff}^0}{\delta_{eff}^f-\delta_{eff}^0}\right)\right]}{1-\exp(-\alpha)}\right\};\ \ \delta_{eff} = \sqrt{\delta_n^2 + \delta_s^2 + \delta_t^2} \tag{4.3}$$

where δ_{eff}^{max} is the maximum effective separation achieved, δ_{eff}^0 is the effective displacement at which microporosity damage begins to propagate, δ_{eff}^f is the effective displacement at which failure occurs, and α is a material parameter. The authors selected an exponential damage progression for the damage parameter ϕ, since it best described the decohesion behavior revealed from MD simulations. The modified traction with damage included was given by the following,

$$t_x = (1 - \phi)\,\bar{t}_x;\quad \forall\, x \in \{n, s, t\} \tag{4.4}$$

where t_x is the resultant traction component; ϕ is the damage parameter; and $\bar{t}_x$ is the predicted linear elastic corresponding component of traction given by Equation (4.2). The calibration (Fig. 4.8/Table 4.3) shows a good agreement between Equation (4.4), and the results from the MD simulations discussed in Section 4.2.

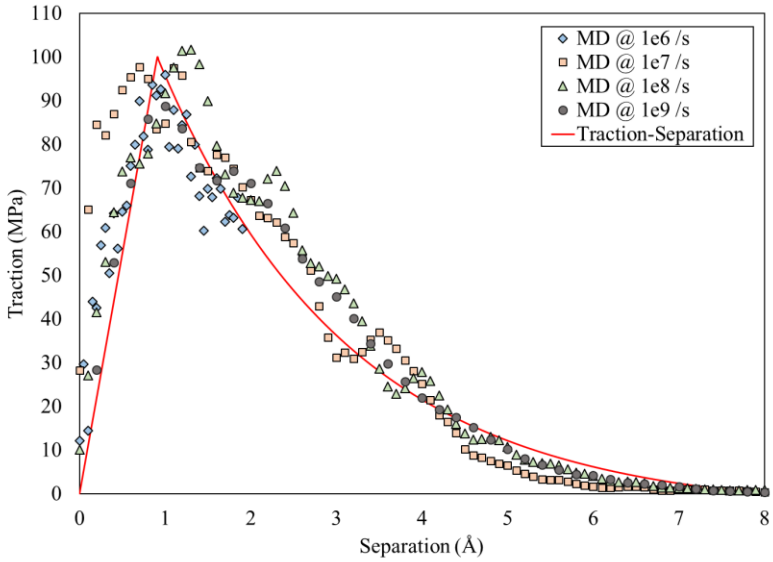

Figure 4.8 The Traction-Separation (T-S) relation was calibrated to Molecular Dynamics (MD) simulation results over a range of applied strain rates. Note that the strain rate effects are minimal.

Table 4.3 The calibrated Traction Separation (T-S) parameter values.

Parameter	Value
δ_{eff}^{0}	0.909 Å
δ_{eff}^{f}	8 Å
α	3.2

4.6.4.1 Gallery Cohesive Strength

This study introduces a cohesive strength moderation parameter, K to modulate the cohesive strength of the PCN gallery layers (Section 4.4.3) to account for the presence of initial defects (Song *et al*. 2014). K contains a value between 0 and 1 modifies the maximum traction a cohesive zone can tolerate before damage progresses. Reordering Equation (4.2),

$$\underline{\delta}^{0} = \underline{\sigma}^{c}\frac{\underline{\boldsymbol{E}}}{T_0};\ \ \underline{\sigma}^{c} = K \cdot \underline{t}_{max} \tag{4.5}$$

where $\underline{\delta}^0$ is the vector of displacements at which damage begins to propagate, $\underline{\sigma}^c$ is a vector containing the cohesive strengths in the normal and two shear directions, and $\underline{t}_{max}$ is the traction vector containing the maximum traction thresholds from the T-S rule.

4.6.5 Periodicity Assumptions

The purpose of an RVE in the context of FEA is to capture the performance of a bulk material simulating only a small repeatable unit cell. To that end, PCN RVEs were periodic across bounding surfaces. During the VCSG process, when a proposed inclusion had a position and orientation such that a portion of the inclusion was protruding from one of the RVE bounding surfaces, the protruding portion was severed and reinserted at the opposite surface. Fig. 4.9 contains a two-dimensional representation of the RVE boundary periodicity.

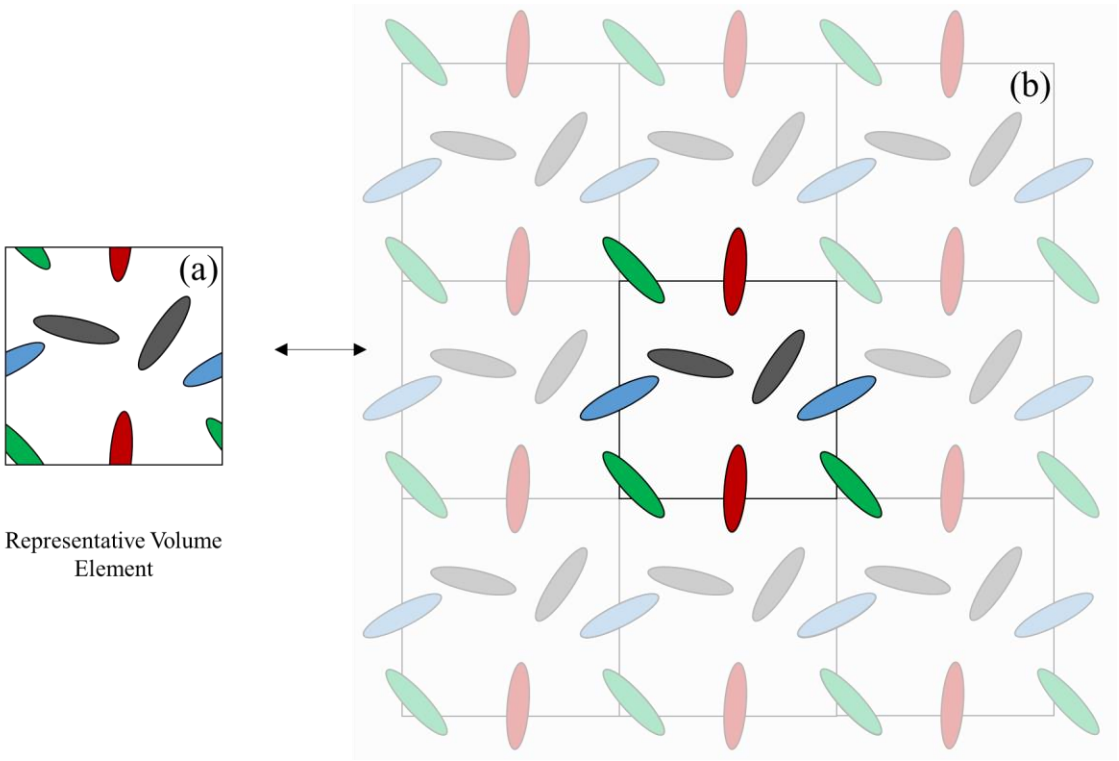

Figure 4.9 Two-dimensional schematic illustrating how a periodic Representative Volume Element (RVE) (a) translates into a continuous bulk material by repeating the RVE in all dimensions (b).

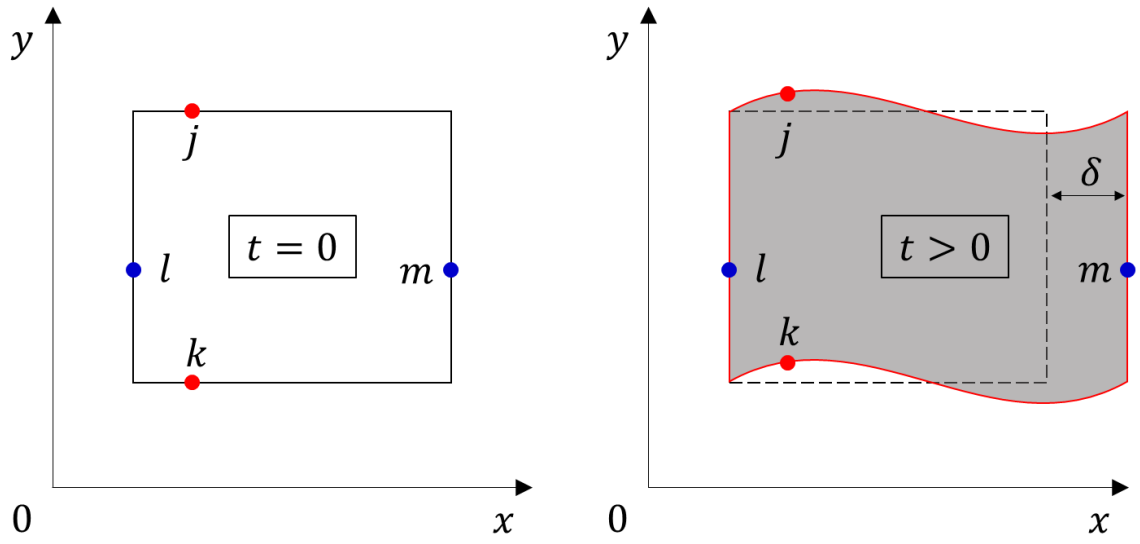

Figure 4.10 Two-dimensional schematic displaying how matching displacements of opposing nodes on a Representative Volume Element (RVE) creates a uniform deformation across opposing faces.

Additionally, RVEs must maintain periodicity throughout deformation. Thus, opposing faces must deform in the same manner so that when RVEs are stacked in three dimensions, they form a continuous volume. Analogous to the two-dimensional work performed by Sheng *et al*. (2004) and Spencer and Sweeney (2008), Multipoint Constraint Equations (MCEs) were employed to equilibrate all displacement Degrees of Freedom (DOFs) of corresponding nodes on opposing faces as they represent the same spatial material point. Fig. 4.10 displays a two-dimensional diagram demonstrating periodic deformation using MCEs. When expanding the MCE periodic deformation technique into the third dimension, the authors reserved special consideration for nodes located along the edges of the RVE (where two adjacent surfaces intersect). Edge nodes have three spatially equivalent corresponding nodes (on the other three parallel edges of the RVE) as opposed to the one that interior surface nodes have. Completely matching all

displacement DOFs for all four corresponding edge nodes creates an over constrained system. Therefore, the displacements of corresponding pairs of edge nodes are constrained *only* across the DOF for which they correspond. Fig. 4.11 contains a diagram demonstrating the relationship of edgewise nodes. This investigation represents the first time MCE corresponding surface shape matching periodic boundary conditions have been implemented in three-dimensions for a PCN RVE.

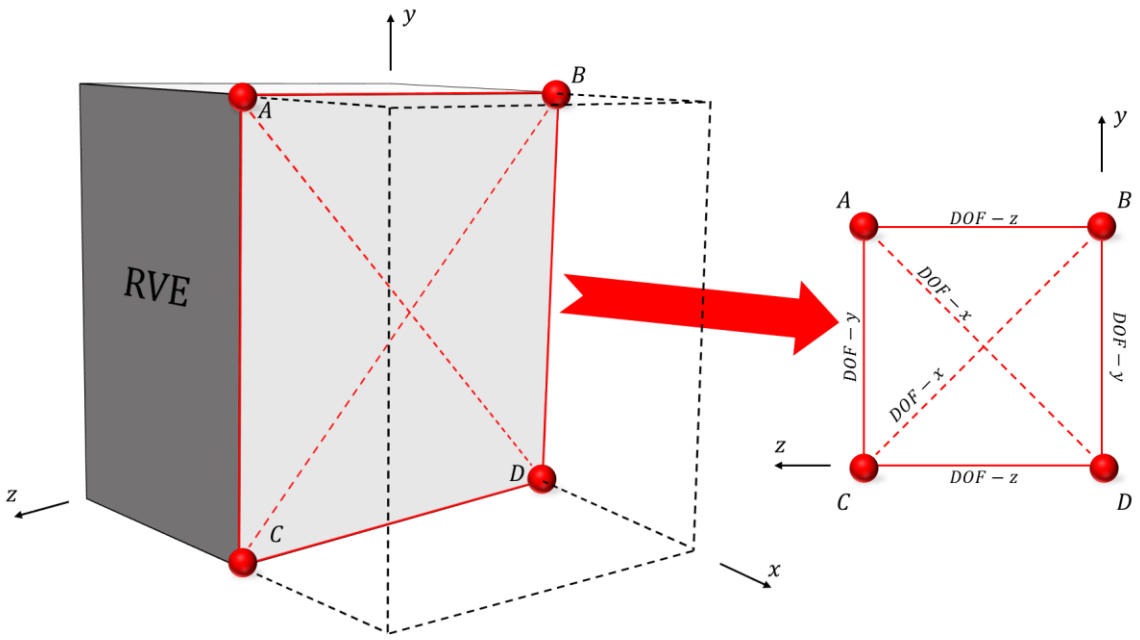

Figure 4.11 Illustration of special Multipoint Constrain Equation (MCE) periodic boundary conditions for edgewise nodes.

Lines $\overline{AB}$ and $\overline{CD}$ represent constraints on the $'z'$ Degree of Freedom (DOF) for nodes pairs $A - B$ and $C - D$, respectively. Lines $\overline{AC}$ and $\overline{BD}$ represent constraints on the $'y'$ DOF for nodes pairs $A - C$ and $B - D$, respectively. Also lines $\overline{AD}$ and $\overline{CB}$ represent constraints on the $'x'$ DOF for nodes pairs $A - D$ and $C - B$, respectively.

4.6.6 Finite Element Setup

A supplementary Python code was implemented to build RVEs in the finite element code Abaqus (Hibbitt 1984) using MMT configurations produced with VCSG. Each RVE employed four distinct material definitions:

- A physically-based, ISV polymer model (Section 4.4) governed the PVA matrix through an explicit material user subroutine (VUMAT) inserted within Abaqus.
- An elastic model featuring a Young's modulus of 182 GPa and a Poisson's ratio of 0.2 determined the behavior of the MMT nanoclay particles.
- A CZM using a T-S rule was calibrated with MD simulation results. The CZM controlled the PVA interphase performance with a peak traction of 100 MPa.
- In order to model the PVA interlayer gallery performance as opposed to the PVA interphase performance, the peak traction of the T-S rule varied from 100 MPa, 60 MPa, and 20 MPa according to the DOE procedure.

The RVEs featured three dimensional, linear, hexagonal elements with reduced integration to discretize the inclusions (C3D8R) whereas interphases and galleries used three dimensional, linear, hexagonal cohesive elements (COH3D8). Note that when the cohesive elements progressed entirely through the T-S rule, they were removed from the simulation (element deletion). Meanwhile, due to the complexity of the PCN structure, the PVA matrix consisted of linear tetrahedral elements (C3D4). All FEA computations applied uniaxial tension to the RVEs by securing the 'negative-x' RVE surface (RVE surface with outward normal parallel to and oriented equivalently with the *negative* x

axis) in the ‘x’ DOF and administering a constant velocity to the ‘positive x’ RVE surface to achieve a constant quasi-static strain rate of 0.0007 /s (RVE surface with outward normal parallel to and oriented equivalently with the *positive* x axis) (see Fig. 4.12). To account for behavioral variation resulting from the random assortment of intercalated structures within RVEs, this work featured two RVE ‘realizations’ per DOE configuration. All computations were run to an applied strain of 0.1, and the volume-averaged stress was obtained from the total sum of the normal forces acting on the positive-x RVE surface with

$$\sigma_x = \frac{1}{\Omega}\sum_i F_x^i \tag{4.6}$$

where σ_x is the axial stress, Ω is the area of the loaded face, and F_x^i is the axial load on the i^{th} node.

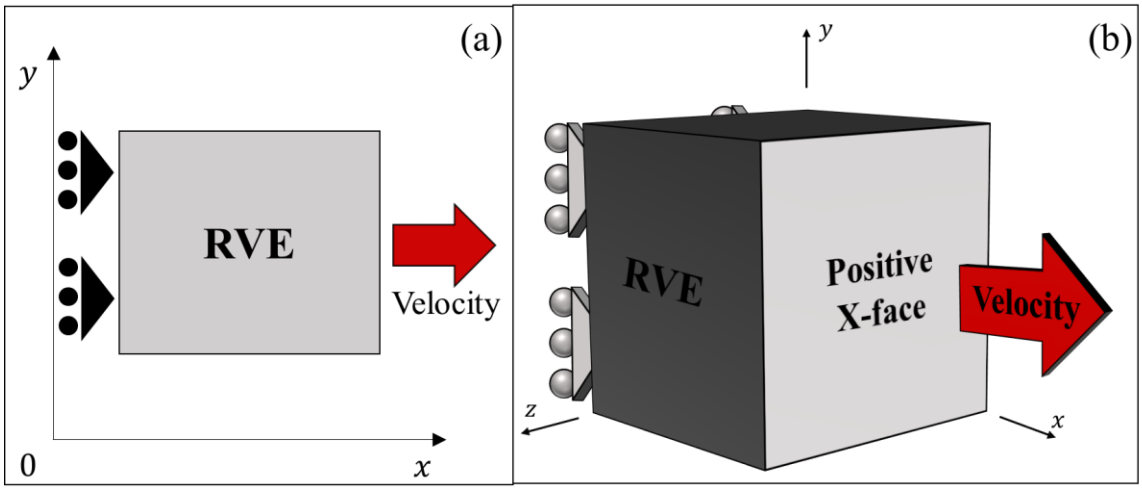

Figure 4.12 Illustration showing finite element boundary conditions applied to Representative Volume Elements (RVEs) in two dimensions (a) and three dimensions (b).

4.6.7 Finite Element Results

4.13 illustrates for DOE Simulation #6 the effect of applying MCE periodic boundary conditions to the outer surfaces of the RVEs. Fig. 4.13 plainly shows that corresponding surfaces deformed with equivalent shapes so that when stacked in three dimensions, the resulting material would be continuous. All DOE simulations featured inelastic deformation driven by delamination between MMT nanoclay particles and the PVA matrix. 4.13 contains MAXSCRT contour plots illustrating the delamination process via cohesive damage over the course of DOE Simulation #6. MXSCRT is a measure of maximum sustainable traction for a cohesive element where a value of 1.0 refers to the point where a cohesive element reaches its maximum traction threshold and damage from the innate microporosity beings to propagate.

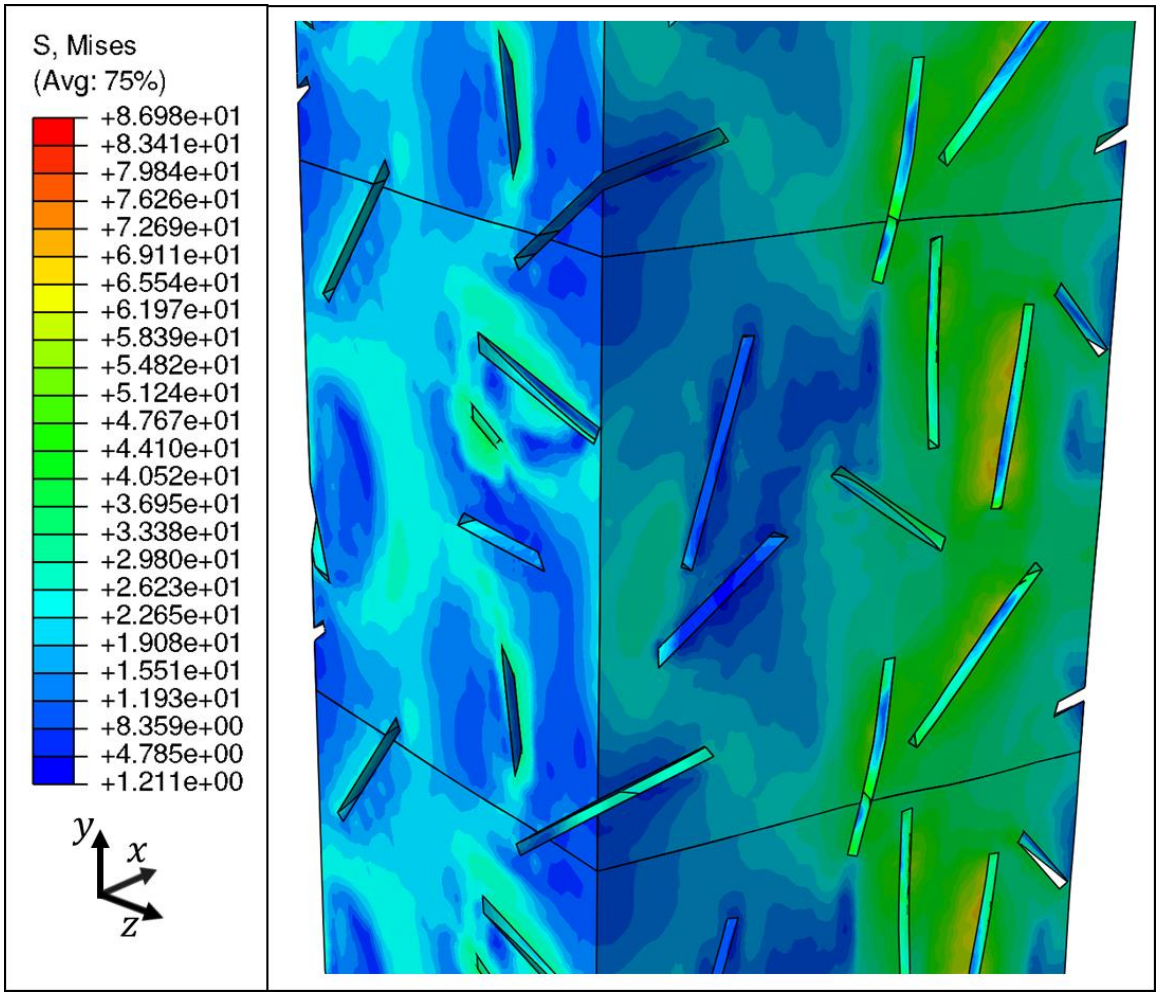

Figure 4.13 Deformed Representative Volume Element (RVE) matrix showing shape matching for corresponding sides at maximum applied strain level (0.1) applied to the positive ‘x’ face.

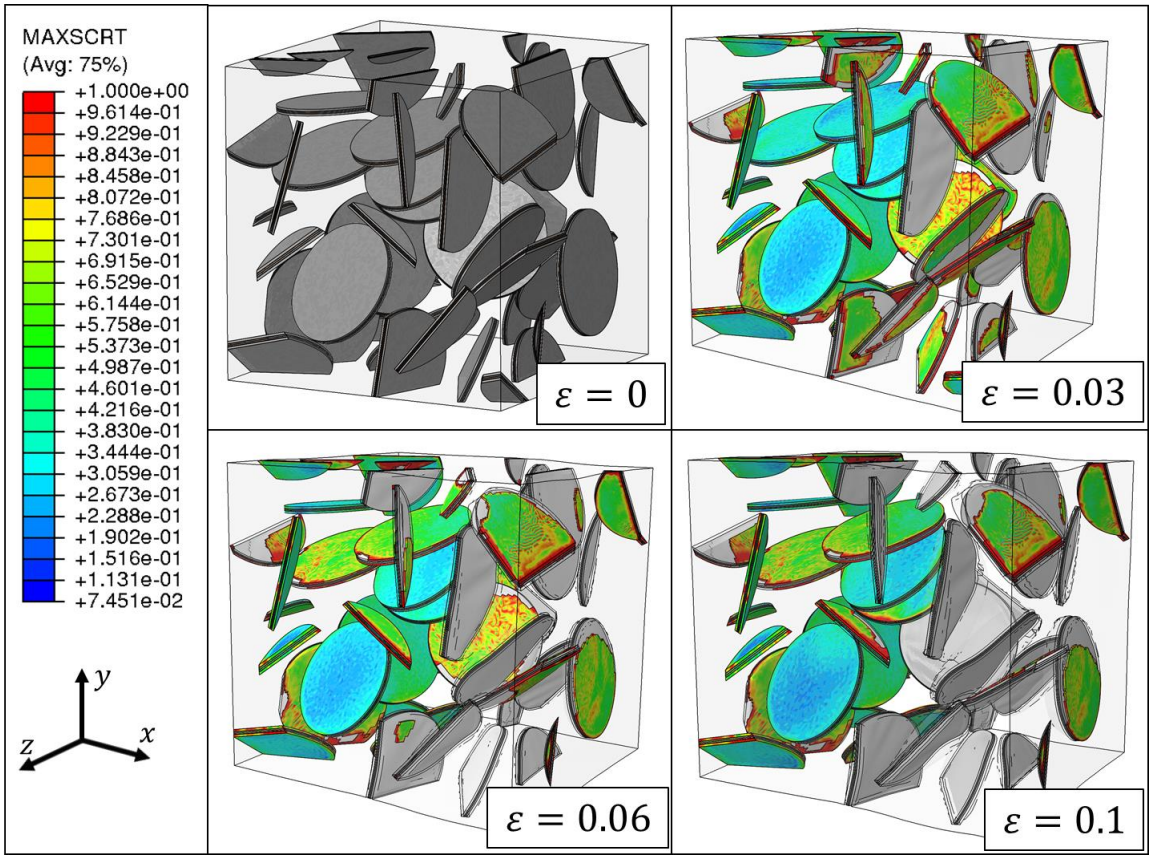

Figure 4.14 Color contours of the cohesive damage progression at different applied strains for Design of Experiments (DOE) Simulation #6 in which this Representative Volume Element (RVE) was created by the Virtual Composite Structure Generator (VCSG).

Note that MAXSCRT measures a cohesive element's progress towards its maximum traction threshold where a value of 1.0 (red color) refers to when a cohesive element reaches its maximum sustainable traction and begins damage propagation.

4.7 Finite Element Uncertainty Quantification

This work employed a Monte Carlo (MC) based metamodel method (Doebling *et al*. 2002) featuring a Radial Basis Function (RBF) to quantify the uncertainty related to the volume averaged stress-strain behavior of the finite element simulations. For the present work, FEA processed configurations of DOE parameters and produced volume averaged stress-strain responses. We calibrated the RBF using the DOE parameter

configurations as inputs and the respective FEA stress-strain results as outputs. A Matlab script executed the calibrated RBF analysis on a uniformly distributed random parameter sampling from within an expanded DOE parameter space in a MC framework. Table 4.4 shows the expanded parameter space generated based on physical admissibility. At each strain point corresponding to the FEA stress-strain behavior, the MC routine sampled one million parameter combinations from the expanded parameter space and passed them through the RBF. Fig. 4.15 contains the stress-strain results of the DOE FEA simulations as well as the MC-RBF calculated uncertainty bands.

Table 4.4 Expanded parameter space used with a Monte Carlo (MC) metamodel method to quantify uncertainty related to the multiscale modeling method presented in this study for polymer/clay nanocomposites.

	Minimum	Maximum
Aspect Ratio	10	2000
Orientation	0^o	180^o
Intercalation	1	50
Gallery Strength	1 MPa	100 MPa

Note that 'intercalation' refers to the number of nanoclay layers used in intercalated lamellar clusters and 'gallery strength corresponds to percentages of the maximum traction used in the Traction-Separation (T-S) rule

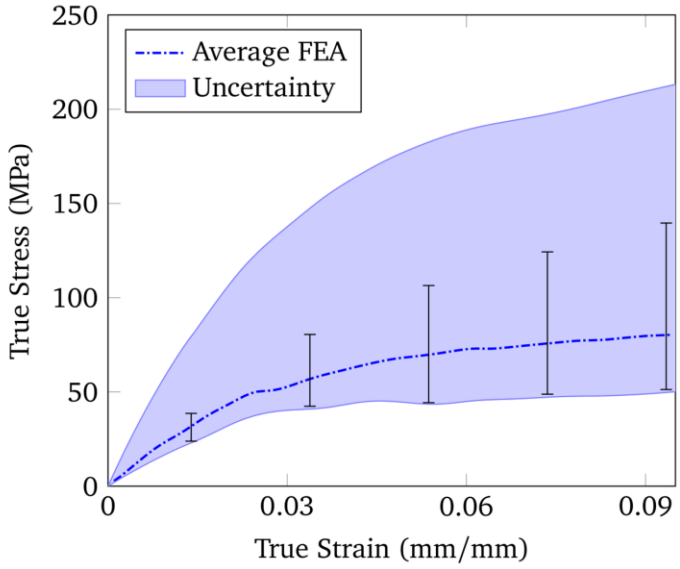

Figure 4.15 True stress-strain behavior showing the range of the Design of Experiments (DOE) Finite Element Analysis (FEA) output along with the uncertainty associated with this work's multiscale modeling implementation.

The uncertainty band was obtained using a Radial Basis Function (RBF) within a Monte Carlo sampling framework.

4.8 Design of Experiments Parametric Examination

The DOE parametric method compares the relative parametric influences between the parameters described in Section 4.3 on the elastic modulus and yield stress of PCNs. Having four parameters quantified at three levels yields 81 (3^4) unique simulations (one for each possible parameter grouping). Since this investigation is only concerned with the first order main parametric effects (no interaction effects), only nine simulations are needed to span the simulation space (DeVor *et al.* 1992). The DOE process organizes parameter settings into an orthogonal array containing the configurations for each DOE simulation (Table 4.5). Mirroring the work of Ramakrishnan and Karunamoorthy (2005), we considered the individual main parametric effects of each DOE parameter on the elastic modulus and yield stress of the FEA simulations using a one-way Analysis of

Variance (ANOVA) method. In general, the one-way ANOVA measures the variance of some 'metric' within each 'parameter level' and compares that "variance within" with the variance of the same metric between parameter levels. A high variance between levels and a low variance within levels indicates a high influence on the metric by the particular parameter being examined. For this work, 'metric' refers to the DOE metrics, elastic modulus and yield stress while 'parameter level' refers to a specific level (Table 4.1) within a DOE parameter (i.e. 400 is the second level within the 'aspect ratio' parameter).

Table 4.5 L9 orthogonal array containing parameter settings for nine Design of Experiments (DOE) finite element simulations.

	Aspect Ratio	Orientation	Intercalation	Gallery Strength
1	100	0	3	0.2
2	100	90	6	0.6
3	100	180	10	1
4	400	0	6	1
5	400	90	10	0.2
6	400	180	3	0.6
7	800	0	10	0.6
8	800	90	3	1
9	800	180	6	0.2

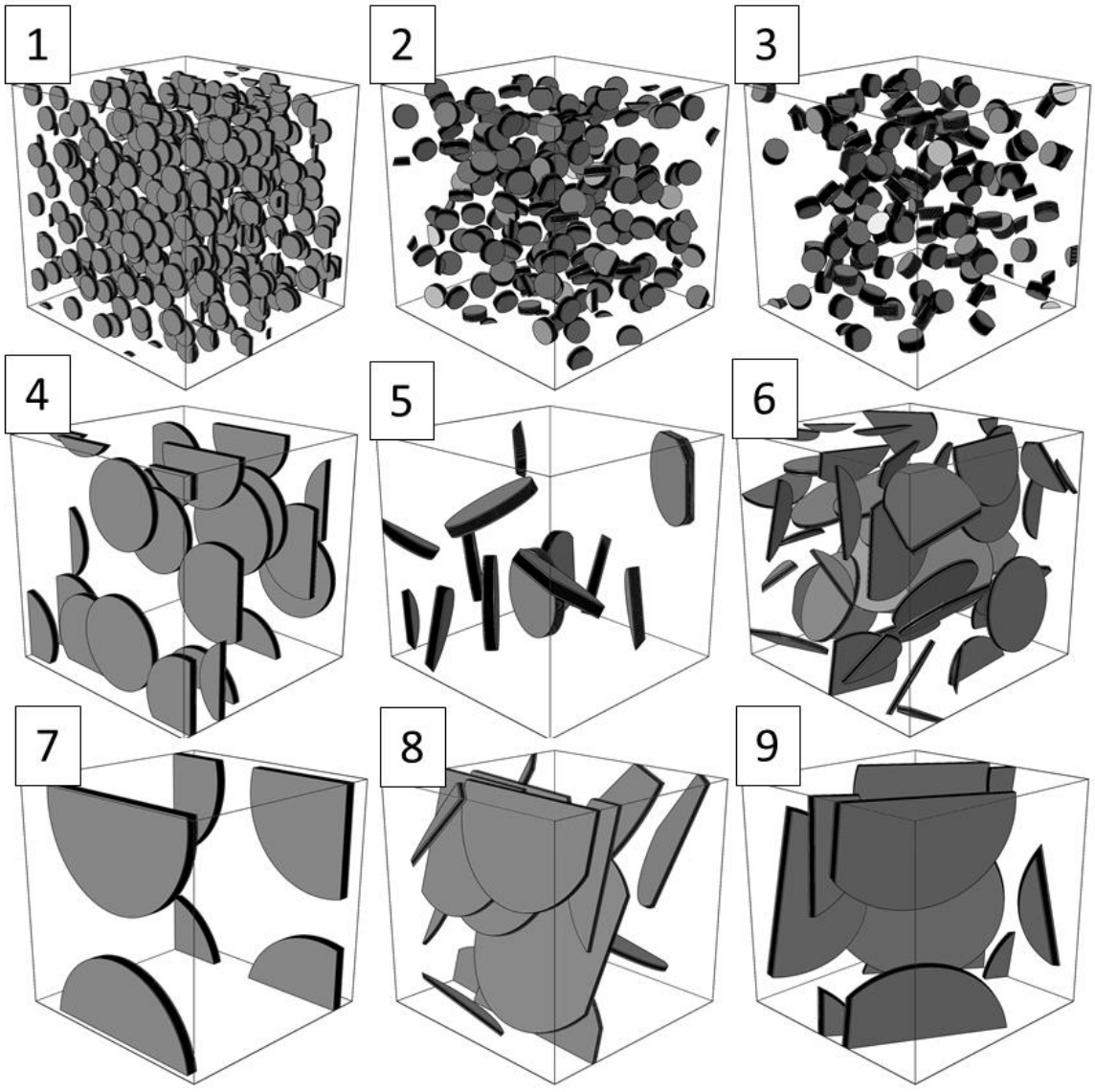

Figure 4.16 Representative Volume Element (RVE) realizations for each Design of Experiments (DOE) parameter configuration.

As Table 4.5 shows, each prescribed level for each DOE parameter (Table 4.1) has three corresponding DOE finite element simulations associated with it. Fig. 4.16 displays an example RVE realization for each DOE parameter configuration. Each DOE finite element simulation resulted in a particular elastic modulus and yield stress (Table 4.6). Thus considering elastic modulus for example, ANOVA takes the variance of the

three elastic moduli within a particular DOE parameter level and compares it to the variance of the *means* of the elastic moduli of each level (Table 4.7). That comparison is called the 'F-Factor' and it is a measure of a parameter's influence on some metric (i.e. elastic modulus). A high variance between levels and a low variance within levels indicates a high influence on the metric by the particular parameter being examined. Whereas the opposite case, high variance within levels and low variance between levels indicates a low parametric influence on the metric.

Table 4.6 Design of Experiments (DOE) finite element results for elastic modulus and yield stress.

Simulation	Elastic Modulus (MPa)	Yield Stress (MPa)
1	2448.48	53.64
2	2476.94	54.28
3	2477.67	85.51
4	2821.97	60.58
5	2468.39	20.05
6	2534.37	40.64
7	2856.25	33.11
8	2468.01	51.70
9	2323.03	22.52

4.9 Parametric Finite Element Results

4.6 contains the elastic modulus and yield stress results for each DOE finite element calculation. Table 4.7 contains mean values of the elastic moduli associated with each DOE parameter level as well as each parameter's relative of influence determined by 'F-Factors' calculated with ANOVA. Similarly, Table 4.8 contains the mean values of the yield stresses corresponding to each DOE parameter level and each parameter's relative influence also determined by 'F-Factors'. Figures 4.16 and 4.17 display the relative normalized influences of each DOE parameter (aspect ratio, orientation,

intercalation, gallery strength) on PCN elastic moduli and yield stresses, respectively. From the data in 4.7 and 4.16, nanoclay particle orientation was the most influential parameter affecting PCN elastic modulus which agrees well with Spencer and Sweeney (2008). Alternatively, 4.8 and 4.17 show that the strength of the interlayer galleries was the most crucial parameter corresponding to PCN yield stress. The importance of interlamellar galleries agrees well with the experimental work performed by Wang *et al*. (2005) which showed that PCN interlayer galleries contained initial microporosity that lead to damage nucleation and propagation from within interlayer galleries.

Table 4.7 Mean values corresponding to each Design of Experiments (DOE) parameter level and each DOE parameter F-Factor influence for the finite element response of the elastic modulus

	Level 1	Level 2	Level 3	F-Factor
Aspect Ratio	2467.71	2608.25	2549.09	0.40
Orientation	2708.90	2471.11	2445.03	3.01
Intercalation	2483.62	2540.65	2600.77	0.06
Gallery Strength	2413.30	2622.52	2589.22	1.28

Table 4.8 Mean values corresponding to each Design of Experiments (DOE) parameter level and each DOE parameter F-Factor influence for the finite element response of the yield stress.

	Level 1	Level 2	Level 3	F-Factor
Aspect Ratio	64.47	40.42	35.60	2.22
Orientation	49.11	42.01	49.38	0.09
Intercalation	48.66	45.62	46.22	0.01
Gallery Strength	31.89	42.67	65.93	3.50

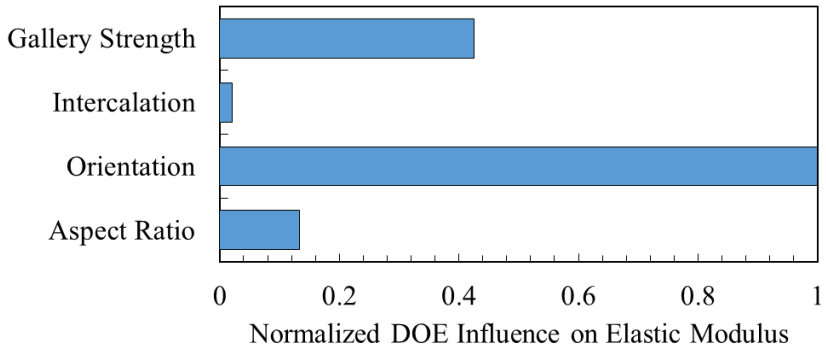

Figure 4.17 Normalized Design of Experiments (DOE) parametric influences on Polymer/Clay Nanocomposite (PCN) elastic moduli.

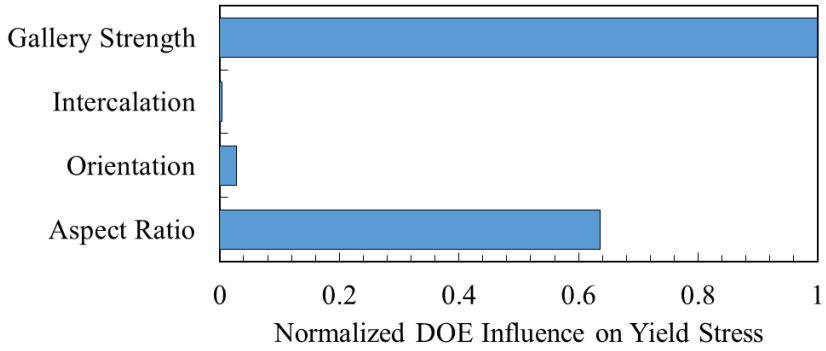

Figure 4.18 Normalized Design of Experiments (DOE) parametric influences on Polymer/Clay Nanocomposite (PCN) yield strengths.

4.10 Discussion

The context of this PVA/MMT study can be found in the multiscale modeling methodology that is the basis behind the Integrated Computational Materials Engineering (ICME) movement (M.F. Horstemeyer 2012). ICME is a paradigm in which a material system can be *designed* using key simulations at relevant length scales to achieve a certain performance. Horstemeyer (2012) highlights a pair of case study examples where ICME was used to effectively optimize metallic material systems. In this study we have

shown that multiscale modeling, and by extension ICME, can be used to effectively design and analyze any material system.

In the case of PCNs, the TEM images in Fig. 4.1 show that the PVA/MMT nanocomposites examined in this study were not optimized as they contained many agglomerations which degrade overall mechanical performance. Fig. 4.18 contains a comparison between the quantified experimental uncertainty and the uncertainty of the DOE FEA simulations quantified with a MC-metamodel method. The comparison in Fig. 4.18 coupled with the TEM evidence in 4.1 exposes the potential for optimization in PCN materials.

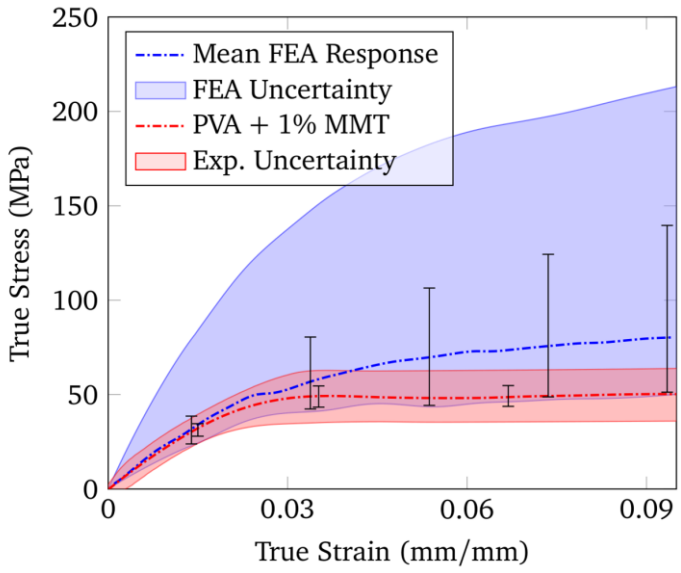

Figure 4.19 True stress-strain comparison between the Design of Experiments (DOE) finite element results and the 1% volume fraction Polyvinyl Alcohol (PVA)/Montmorillonite (MMT) tensile experiments with their associated uncertainties.

Note the overlapping portions of the uncertainties indicate the portions of the DOE parameter space that is physically admissible.

For example according to the MC-RBF routine, the optimum configuration within the expanded parameter space considered in the present work is:

- Aspect ratio: 2000
- Orientation: 0^o
- Intercalation: 1
- Gallery strength: 100 MPa

where each of the above values constitutes the extreme case for each parameter. The very top-most boundary of the multiscale modeling uncertainty shown in Fig, 4.18 corresponds to the aforementioned optimum configuration. Conversely, the MC-RBF routine found the following non-unique parameter configuration to produce a result closest to the 1% volume fraction PVA/MMT experimental data:

- Aspect ratio: 670
- Orientation: 140^o
- Intercalation: 8
- Gallery strength: 84 MPa

While the configuration above is non-unique, it serves to demonstrate the large amount of optimization still possible if a sufficiently advanced fabrication technique can be established for PCNs.

4.11 Summary

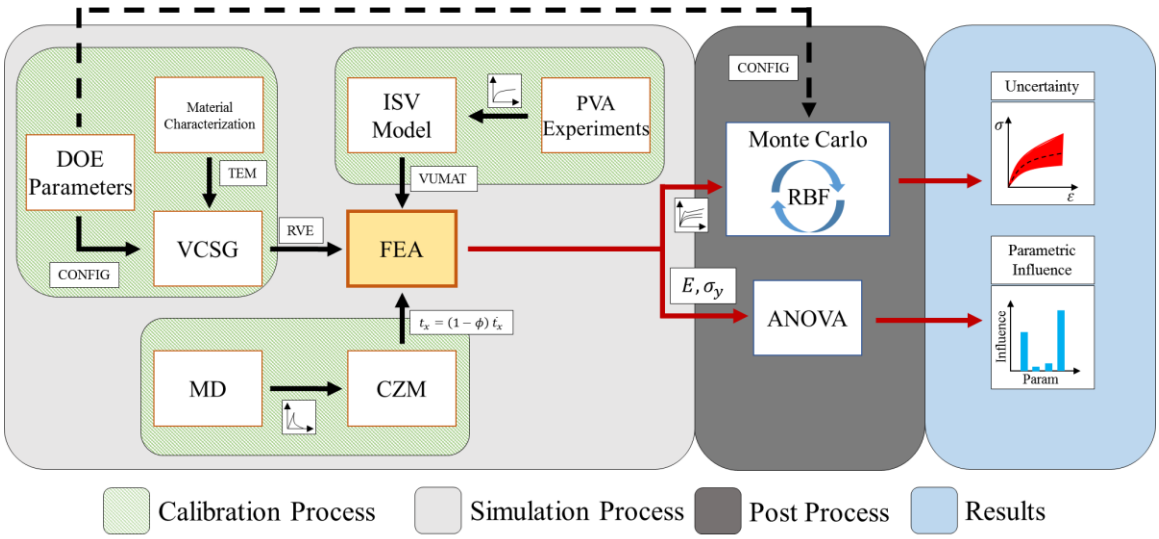

Figure 4.20 Simulation process schematic displaying information flow for Design of Experiments (DOE) finite parametric analysis.

4.19 contains a process schematic outlining the information flow of the multiscale modeling technique featured in this investigation. In the present work we employed a hierarchical multiscale modeling methodology to bridge the nanoscale and micro/mesoscale for PCNs via implementing key information from MD simulation results into a T-S rule within a CZM to govern interfacial behavior within PCN micro/mesoscale finite element simulations. The FEA simulations consisted of three-dimensional RVEs constructed with VCSG, a physically-based ISV polymer model for the PVA matrix, and a CZM obtained using subscale MD simulation results for the PVA/MMT interfaces. A DOE parametric study was conducted under uncertainty on four parameters (aspect ratio, orientation, intercalation, and gallery strength) related to nanoclay filler within a polymer matrix. The parametric study used an ANOVA method

to quantify the influence of each DOE parameter. The effort determined that nanoclay particle orientation had the greatest influence on PCN elastic modulus while the interlayer gallery strength had the greatest impact on PCN yield stress. Finally a RBF cast in a MC framework quantified the uncertainty of the multiscale modeling method used in this study.

CHAPTER V

SUMMARY AND FUTURE WORK

5.1 Summary

The presented effort consists of a hierarchical multiscale modeling methodology for polymer based material systems. Two dimensional plane-strain finite element simulations coupled to the Bouvard ISV polymer model calibrated to physical experiments, and cast in a DOE parametric framework at the mesoscale revealed that the applied stress state, which promotes a particular stress triaxiality, was the most influential parameter affecting damage growth and coalescence in polymers. The importance of the applied stress state then served as key information upscaled into the macroscale and motivated the modification of the Bouvard ISV polymer model. The ISV model was modified using deviatoric stress invariants to enhance the model's sensitivity to changes in mechanical performance across different stress states (tension, compression, and torsion). The modification utilizes a stress invariant function obtained from similar work in modeling metals (Mark F. Horstemeyer and Gokhale 1999; M.F. Horstemeyer, Lathrop, *et al*. 2000). A hierarchical multiscale modeling method was then employed to examine the relative parametric influences of four parameters (aspect ratio, orientation, intercalation, and gallery strength) related to PCN morphological heterogeneities on the elastic modulus and yield stress of PCNs. Results obtained from MD simulations of a PVA/MMT interface were upscaled to calibrate a T-S rule within a CZM to govern

interfacial behavior within PCN micro/mesoscale finite element simulations. The FEA simulations consisted of three-dimensional RVEs constructed with VCSG, a physically-based ISV polymer model for the PVA matrix, and a CZM obtained using subscale MD simulation results for the PVA/MMT interfaces. A DOE parametric study was conducted under uncertainty on four parameters (aspect ratio, orientation, intercalation, and gallery strength) related to nanoclay filler within a polymer matrix. The parametric study revealed that nanoclay particle orientation had the greatest influence on PCN elastic modulus while the interlayer gallery strength had the greatest impact on PCN yield stress.

5.2 Future Work

5.2.1 Expand VCSG Capability and Use it to Simulate Higher Complexity Composites

Currently, VCSG can generate composite morphologies with disk or cylinder shaped heterogeneities only. Furthermore the algorithm uses uniform (as opposed to normal or bi-modal, *etc.*) distributions for the random positions and orientations it generates. Thus further work is needed to outfit the VCSG algorithm with the capability of producing RVEs with different heterogeneity geometries (*i.e.* spherical, ellipsoidal, and or amorphous). Additional geometries could be combined to form highly complex composites like concrete.

Advancing the VCSG algorithm will require additional knowledge of the composite morphology in question. In the case of nanocomposites, obtaining the morphological data will require either better nanostructural imaging (TEM, AFM, *etc*) and/or better nanostructure quantification techniques. Fig. 5.1 shows a typical TEM image of a 5% volume fraction PVA/MMT nanocomposite material. With an image like

the one in Fig. 5.1, it is impossible using traditional image analysis techniques to capture morphological properties such as particle sizes, nearest neighbor distances, particle orientations, *etc.* Thus enhancing either the imagine techniques, the analysis techniques, or both would enable VCSG to use physically-based heterogeneity distributions in RVEs.

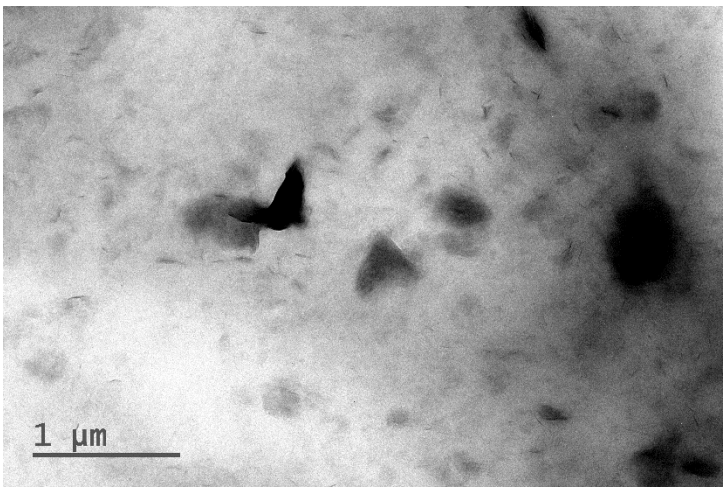

Figure 5.1 Transmission Electron Micrograph (TEM) of a 5% volume fraction Polyvinyl Alcohol (PVA)/Montmorillonite (MMT) nanocomposite.

Note that specific morphological details are impossible to isolate using image analysis techniques.

5.2.2 Use VCSG and Metamodeling to Optimize PCNs and Other Composites

In Chapter 4 a MC based RBF metamodel was used to quantify a set of parameters that would optimize the physical mechanical performance of a 1% volume fraction PVA/MMT nanocomposite. Those results however were for uniaxial quasi-static tension behavior. Further work is needed in order to use objective design optimization on composites under complex loading and/or at higher strains.

More mechanical experimental data from a range of temperatures, strain rates, and stress states is required to achieve a true (unique) calibration of the Bouvard ISV

model. Then micro/nanostructural (particle size, orientation, nearest neighbor distance, *etc.)* data needs to be quantified and used to modify VCSG to include physically-based distributions and geometries of that structural data. With the aforementioned collection of experimental data, a similar procedure outlined in Chapter 4 could be implemented to find the optimum structural parameter configuration for some set of objectives (*i.e.* high ductility/strain-to-failure, high modulus/yield stress, increased damping, fatigue resistance, *etc.*).

As an example, concrete traditionally contains an assortment of different secondary phases that all have different geometries, distributions, *etc.* Given the appropriate amount a statistical data and an adequately calibrated physically-based material model for the concrete matrix, a small number of high complexity FEA simulations could be used to train a much reduced order metamodel (such as RBF or a polynomial response function, or a Kriging model, *etc.*). That metamodel can then be run thousands or millions of times relatively quickly over any range of parameters looking for optimized configurations for any set of criteria. This would be analogous to the process laid out in Chapter 4.

5.2.3 Development of Full CZM for Composite Material Interfaces

In Chapter 4, a CZM is established featuring a T-S rule to control the PVA/MMT interface behavior. The T-S rule was calibrated to results of MD simulations upscaled in a hierarchical framework. While this multiscale method is effective in simulating composite interfaces, as Equation 4.2 shows there are three components of traction in cohesive elements (a normal, and two shear directions). Furthermore Fig. 5.2 shows the normal direction T-S rule used in Chapter 4 as well as the theoretical shear behavior for

the same system from Paliwal *et al*.(2016). Fig, 5.2 demonstrates a drastic difference in T-S behavior for separate components of traction.

Thus further work is needed to construct a custom user subroutine (UMAT, VUMAT, or UEL) to capture the full range of cohesive behaviors. The subroutine could then be combined with RVEs from VCSG to create higher fidelity simulations for any material system.

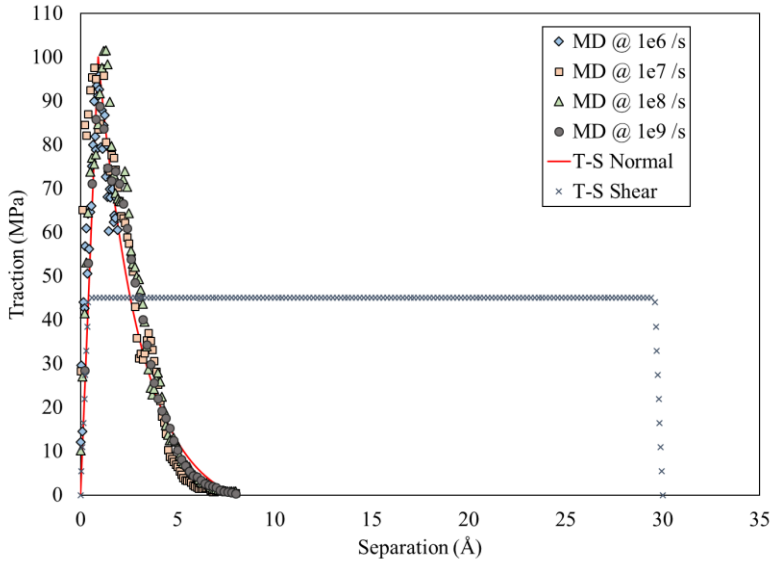

Figure 5.2 Traction vs separation (T-S) plot showing the Molecular Dynamics (MD) simulation results, the T-S rule for the normal direction used in Chapter 4, and a theoretical T-S rule for a shear direction.

5.2.4 Development of a Physically-based Macroscale Constitutive Model for Polymers Featuring Any Length Scale Heterogeneities

The novel materials of the future will likely be rely on synergy between a host material and one or more constituent fillers (i.e. high performance concrete). Such materials cannot be effectively simulated at the macro/structural scale without the proper

constitutive relationships implemented in a physically-based mathematical model. Such a model could make use of key information regarding specific heterogeneity effects upscaled from lower length scale simulations or experiments. The Bouvard-Francis (J. L. Bouvard *et al*. 2013; Francis *et al*. 2014) ISV model works well, but only covers the physically-based behavior of pure polymers. Likewise widely used physically-based models for metals (Bammann *et al*. 1993; Mark F. Horstemeyer and Gokhale 1999; M.F. Horstemeyer, Lathrop, *et al*. 2000) do well for pure metallics and even alloys, but do not contain the necessary constitutive relationships for polymeric secondary phases. More work is needed to develop constitutive relations that account for the effects of secondary phase geometry, orientations, *etc*.

REFERENCES

Abts, Georg, Thomas Eckel, and Rolf Wehrmann. 2014. “Polycarbonates.” In *Ullmann’s Encyclopedia of Industrial Chemistry*. Wiley-VCH Verlag GmbH & Co. KGaA. doi:10.1002/14356007.a21_207.pub2.

Acar, Erdem, and Kiran Solanki. 2008. “System Reliability Based Vehicle Design for Crashworthiness and Effects of Various Uncertainty Reduction Measures.” *Structural and Multidisciplinary Optimization* 39 (3) (October 31): 311–325. doi:10.1007/s00158-008-0327-3. http://link.springer.com/10.1007/s00158-008-0327-3.

Adams, D. F. 1970. “Inelastic Analysis of a Unidirectional Composite Subjected to Transverse Normal Loading.” *Journal of Composite Materials* 4 (3) (January 1): 310–328. doi:10.1177/002199837000400303. http://jcm.sagepub.com/cgi/doi/10.1177/002199837000400303.

Alexandre, Michael, and Philippe Dubois. 2000. “Polymer-Layered Silicate Nanocomposites: Preparation, Properties and Uses of a New Class of Materials.” *Materials Science and Engineering: R: Reports* 28 (1-2) (June): 1–63. doi:10.1016/S0927-796X(00)00012-7. http://www.sciencedirect.com/science/article/pii/S0927796X00000127.

Alfano, G., and M. A. Crisfield. 2001. “Finite Element Interface Models for the Delamination Analysis of Laminated Composites: Mechanical and Computational Issues.” *International Journal for Numerical Methods in Engineering* 50 (7) (March 10): 1701–1736. doi:10.1002/nme.93. http://doi.wiley.com/10.1002/nme.93.

Alisafaei, Farid, Chung-Souk Han, and Nitin Garg. 2016. “On Couple-Stress Elasto-Plastic Constitutive Frameworks for Glassy Polymers.” *International Journal of Plasticity* 77 (February): 30–53. doi:10.1016/j.ijplas.2015.09.011. http://www.sciencedirect.com/science/article/pii/S0749641915001655.

Allison, P G, R D Moser, M Q Chandler, O G Rivera, J R Goodwin, E R Gore, and C A Weiss Jr. 2015. “Mechanical , Thermal , and Microstructural Analysis of Polyvinyl Alcohol / Montmorillonite Nanocomposites.” *Journal of Nanomaterials* 2015.

Ames, Nicoli M., Vikas Srivastava, Shawn A. Chester, and Lallit Anand. 2009. “A Thermo-Mechanically Coupled Theory for Large Deformations of Amorphous Polymers. Part II: Applications.” *International Journal of Plasticity* 25 (8): 1495–1539. http://www.sciencedirect.com/science/article/pii/S074964190800171X.

Anand, L, and N Ames. 2006. “On Modeling the Micro-Indentation Response of an Amorphous Polymer.” *International Journal of Plasticity* 22 (6) (June): 1123–1170. doi:10.1016/j.ijplas.2005.07.006. http://www.sciencedirect.com/science/article/pii/S0749641905001415.

Anand, Lallit, Nicoli M. Ames, Vikas Srivastava, and Shawn A. Chester. 2009. “A Thermo-Mechanically Coupled Theory for Large Deformations of Amorphous Polymers. Part I: Formulation.” *International Journal of Plasticity* 25 (8): 1474–1494. http://www.sciencedirect.com/science/article/pii/S0749641908001708.

Arruda, Ellen M., Mary C. Boyce, and R. Jayachandran. 1995. “Effects of Strain Rate, Temperature and Thermomechanical Coupling on the Finite Strain Deformation of Glassy Polymers.” *Mechanics of Materials* 19 (2-3) (January): 193–212. doi:10.1016/0167-6636(94)00034-E. http://www.sciencedirect.com/science/article/pii/016766369400034E.

Arruda, Ellen M., Mary C. Boyce, and Harald Quintus-Bosz. 1993. “Effects of Initial Anisotropy on the Finite Strain Deformation Behavior of Glassy Polymers.” *International Journal of Plasticity* 9 (7): 783–811. doi:10.1016/0749-6419(93)90052-R.

Asp, L.E., L.A. Berglund, and R. Talreja. 1996. “A Criterion for Crack Initiation in Glassy Polymers Subjected to a Composite-like Stress State.” *Composites Science and Technology* 56 (11) (January): 1291–1301. doi:10.1016/S0266-3538(96)00090-5. http://www.sciencedirect.com/science/article/pii/S0266353896000905.

Ayoub, G., F. Zaïri, C. Fréderix, J.M. Gloaguen, M. Naït-Abdelaziz, R. Seguela, and J.M. Lefebvre. 2011. “Effects of Crystal Content on the Mechanical Behaviour of Polyethylene under Finite Strains: Experiments and Constitutive Modelling.” *International Journal of Plasticity* 27 (4) (April): 492–511. doi:10.1016/j.ijplas.2010.07.005. http://www.sciencedirect.com/science/article/pii/S0749641910000963.

Baghani, M., R. Naghdabadi, J. Arghavani, and S. Sohrabpour. 2012. “A Thermodynamically-Consistent 3D Constitutive Model for Shape Memory Polymers.” *International Journal of Plasticity* 35 (August): 13–30. doi:10.1016/j.ijplas.2012.01.007. http://www.sciencedirect.com/science/article/pii/S0749641912000083.

Balieu, R., F. Lauro, B. Bennani, R. Delille, T. Matsumoto, and E. Mottola. 2013. “A Fully Coupled Elastoviscoplastic Damage Model at Finite Strains for Mineral Filled Semi-Crystalline Polymer.” *International Journal of Plasticity* 51 (December): 241–270. doi:10.1016/j.ijplas.2013.05.002. http://www.sciencedirect.com/science/article/pii/S0749641913001009.

Bammann, D. J., M. L. Chiesa, M. F. Horstemeyer, L. I. Weingarten, and N. J. A. T. Weirzbicki. 1993. “Structural Crashworthiness and Failure.” *Applied Science*: 1–54.

Bammann, D. J., M. L. Chiesa, and G. C. Johnson. 1996. “Modeling Large Deformation and Failure in Manufacturing Processes.” In *Proceedings of the XIXth International Congress of Theoretical and Applied Mechanics*, 359–375. Kyoto, Japan.

Bardenhagen, S.G., M.G. Stout, and G.T. Gray. 1997. “Three-Dimensional, Finite Deformation, Viscoplastic Constitutive Models for Polymeric Materials.” *Mechanics of Materials* 25 (4) (May): 235–253. doi:10.1016/S0167-6636(97)00007-0. http://www.sciencedirect.com/science/article/pii/S0167663697000070.

Barenblatt, G. I. 1962. “The Mathematical Theory of Equilibrium Cracks in Brittle Fracture.” In *Advances in Applied Mechanics, Vol. 7*, 55–125.

Baskes, M.I. 1987. “Application of the Embedded-Atom Method to Covelant Materials: A Semiempirical Potential for Silicon.” *Physical Review Letters* 59 (23): 2666–2669.

Beyer, Günter. 2002. “Nanocomposites: A New Class of Flame Retardants for Polymers.” *Plastics, Additives and Compounding* 4 (10) (October): 22–28. doi:10.1016/S1464-391X(02)80151-9. http://www.sciencedirect.com/science/article/pii/S1464391X02801519.

Bigoni, D., M. Ortiz, and A. Needleman. 1997. “Effect of Interfacial Compliance on Bifurcation of a Layer Bonded to a Substrate.” *International Journal of Solids and Structures* 34 (33-34) (November): 4305–4326. doi:10.1016/S0020-7683(97)00025-5. http://www.sciencedirect.com/science/article/pii/S0020768397000255.

Bouvard, J. L., D. K. Francis, M. A. Tschopp, E. B. Marin, D. J. Bammann, and M. F. Horstemeyer. 2013. “An Internal State Variable Material Model for Predicting the Time, Thermomechanical, and Stress State Dependence of Amorphous Glassy Polymers under Large Deformation.” *International Journal of Plasticity* 42: 168–193. http://www.sciencedirect.com/science/article/pii/S0749641912001581.

Bouvard, J. L., D. K. Ward, D. Hossain, E. B. Marin, D. J. Bammann, and M. F. Horstemeyer. 2010. “A General Inelastic Internal State Variable Model for Amorphous Glassy Polymers.” *Acta Mechanica* 213 (1-2) (June 19): 71–96. doi:10.1007/s00707-010-0349-y. http://link.springer.com/10.1007/s00707-010-0349-y.

Bouvard, J. L., D. K. Ward, D. Hossain, S. Nouranian, E. B. Marin, and M. F. Horstemeyer. 2009. “Review of Hierarchical Multiscale Modeling to Describe the Mechanical Behavior of Amorphous Polymers.” *Journal of Engineering Materials and Technology* 131 (4): 041206. doi:10.1115/1.3183779. http://materialstechnology.asmedigitalcollection.asme.org/article.aspx?articleid=1428527.

Bouvard, J.L., J.L. Chaboche, F. Feyel, and F. Gallerneau. 2009. “A Cohesive Zone Model for Fatigue and Creep–fatigue Crack Growth in Single Crystal Superalloys.” *International Journal of Fatigue* 31 (5) (May): 868–879. doi:10.1016/j.ijfatigue.2008.11.002. http://www.sciencedirect.com/science/article/pii/S0142112308002521.

Bouvard, Jean-Luc, Hayley Brown, Esteban Marin, Paul Wang, and Mark Horstemeyer. 2011. “Mechanical Testing and Material Modeling of Thermoplastics: Polycarbonate, Polypropylene and Acrylonitrile-Butadiene-Styrene.” *MRS Proceedings* 1130 (February 1): 1130–W06–09. doi:10.1557/PROC-1130-W06-09. http://journals.cambridge.org/abstract_S1946427400024040.

Box, G. E. P., J. S. Hunter, and W. G. Hunter. 1978. *Statistics for Experimenters: Design, Innovation, and Discovery*. New York: Wiley *et al*.

Boyce, Mary C., David M. Parks, and Ali S. Argon. 1988. “Large Inelastic Deformation of Glassy Polymers. Part I: Rate Dependent Constitutive Model.” *Mechanics of Materials* 7 (1) (September): 15–33. doi:10.1016/0167-6636(88)90003-8. http://www.sciencedirect.com/science/article/pii/0167663688900038.

Brazel, Christopher S, and Nikolaos A Peppas. 1999. “Mechanisms of Solute and Drug Transport in Relaxing, Swellable, Hydrophilic Glassy Polymers.” *Polymer* 40 (12) (June): 3383–3398. doi:10.1016/S0032-3861(98)00546-1. http://www.sciencedirect.com/science/article/pii/S0032386198005461.

Bridgman, P. W. 1923. “The Compressibility of Thirty Metals as a Function of Pressure and Temperature.” *Proceedings of the American Academy of Arts and Sciences* 58 (5): 165–242.

Brown, L. M., and J. D. Embury. 1973. “Initiation and Growth of Voids at Second-Phase Particles.” In *Proc. Conf. on Microstructure and Design of Alloys, Institute of Metals and Iron and Steel Insitute*, 164–169. London.

Budd, Peter M., Neil B. McKeown, and Detlev Fritsch. 2005. “Free Volume and Intrinsic Microporosity in Polymers.” *Journal of Materials Chemistry* 15 (20) (May 18): 1977. doi:10.1039/b417402j. http://pubs.rsc.org/en/content/articlehtml/2005/jm/b417402j.

Camacho, G.T., and M. Ortiz. 1996. “Computational Modelling of Impact Damage in Brittle Materials.” *International Journal of Solids and Structures* 33 (20-22) (August): 2899–2938. doi:10.1016/0020-7683(95)00255-3. http://www.sciencedirect.com/science/article/pii/0020768395002553.

Carrado, Kathleen a., P. Thiyagarajan, and Delwin L. Elder. 1996. “Polyvinyl Alcohol-Clay Complexes Formed by Direct Synthesis.” *Clays and Clay Minerals* 44 (4): 506–514. doi:10.1346/CCMN.1996.0440409.

Cayzac, Henri-Alexandre, Kacem Saï, and Lucien Laiarinandrasana. 2013. “Damage Based Constitutive Relationships in Semi-Crystalline Polymer by Using Multi-Mechanisms Model.” *International Journal of Plasticity* 51 (December): 47–64. doi:10.1016/j.ijplas.2013.06.008. http://www.sciencedirect.com/science/article/pii/S0749641913001198.

Chaboche, Jean-Louis. 1997. “Thermodynamic Formulation of Constitutive Equations and Application to the Viscoplasticity and Viscoelasticity of Metals and Polymers.” *International Journal of Solids and Structures* 34 (18) (June): 2239–2254. doi:10.1016/S0020-7683(96)00162-X. http://www.sciencedirect.com/science/article/pii/S002076839600162X.

Chawla, N, R Sidhu, and V Ganesh. 2006. “Three-Dimensional Visualization and Microstructure-Based Modeling of Deformation in Particle-Reinforced Composites.” *Acta Materialia* 54 (6) (April): 1541–1548. doi:10.1016/j.actamat.2005.11.027. http://linkinghub.elsevier.com/retrieve/pii/S1359645405007056.

Chen, C. C., and J. A. Sauer. 1990. “Yield and Fracture Mechanisms in ABS.” *Journal of Applied Polymer Science* 40 (34) (August 5): 503–521. doi:10.1002/app.1990.070400317. http://doi.wiley.com/10.1002/app.1990.070400317.

Chin, In-Joo, Thomas Thurn-Albrecht, Ho-Cheol Kim, Thomas P. Russell, and Jing Wang. 2001. “On Exfoliation of Montmorillonite in Epoxy.” *Polymer* 42 (13) (June): 5947–5952. doi:10.1016/S0032-3861(00)00898-3. http://www.sciencedirect.com/science/article/pii/S0032386100008983.

Christensen, R. M. 1982. *Theory of Viscoplasticity*.

Clausen, Arild Holm, Mario Polanco-Loria, Torodd Berstad, and Odd Sture Hopperstad. 2010. “A Constitutive Model for Thermoplastics with Some Applications.” *8th European LS-DYNA Users Conference* (May 2011): 1–11. http://sem-proceedings.com/10f/sem.org-IMPLAST-2010-SEM-Fall-s005p02-A-Constitutive-Model-Thermoplastics-With-Some-Applications.pdf.

Cocks, A. C. F., and M. F. Ashby. 1980. “Intergranular Fracture during Power-Law Creep under Multiaxial Stresses.” *Metal Science* 14 (8-9) (August 18): 395–402. doi:10.1179/030634580790441187. http://www.maneyonline.com/doi/abs/10.1179/030634580790441187.

Coleman, Bernard D., and Morton E. Gurtin. 1967. “Thermodynamics with Internal State Variables.” *The Journal of Chemical Physics* 47 (2) (July 15): 597–613. doi:10.1063/1.1711937. http://scitation.aip.org/content/aip/journal/jcp/47/2/10.1063/1.1711937.

Coleman, H. W., and W. G. Steele. 1999. *Experimentation and Uncertainty Analysis for Engineers*. New York.

Constable, I, J G Williams, and D J Burns. 1970. “Fatigue and Cyclic Thermal Softening of Thermoplastics.” *ARCHIVE: Journal of Mechanical Engineering Science 1959-1982 (Vols 1-23)* 12 (1) (February 1): 20–29. doi:10.1243/JMES_JOUR_1970_012_006_02. http://jms.sagepub.com/content/12/1/20.short.

Cooper, Andrew I. 2009. “Conjugated Microporous Polymers.” *Advanced Materials* 21 (12) (March 26): 1291–1295. doi:10.1002/adma.200801971. http://doi.wiley.com/10.1002/adma.200801971.

Dandekar, Chinmaya R., and Yung C. Shin. 2011. “Molecular Dynamics Based Cohesive Zone Law for Describing Al–SiC Interface Mechanics.” *Composites Part A: Applied Science and Manufacturing* 42 (4) (April): 355–363. doi:10.1016/j.compositesa.2010.12.005. http://www.sciencedirect.com/science/article/pii/S1359835X10003210.

Day, Daniel, and Min Gu. 2002. “Formation of Voids in a Doped Polymethylmethacrylate Polymer.” *Applied Physics Letters* 80 (13) (March 26): 2404. doi:10.1063/1.1467615. http://scitation.aip.org/content/aip/journal/apl/80/13/10.1063/1.1467615.

DeVor, E., T. Chang, and J. W. Sutherland. 1992. *Statistical Quality Design and Control : Contemporary Concepts and Methods*. http://www.abebooks.com/Statistical-Quality-Design-Control-Contemporary-Concepts/1406720410/bd.

Doebling, Scott W, Francois M Hemez, John F Schultze, and Amanda L Cundy. 2002. "A Metamodel-Based Approach to Model Validation for Nonlinear Finite Element Simulations Model Validation – Beyond Test / Analysis Correlation." *Simulation*.

Drucker, D. C. 1949. "No Title." *Proceedings and Symposia of Applied Math* 1 (181).

Dugdale, D.S. 1960. "Yielding of Steel Sheets Containing Slits." *Journal of the Mechanics and Physics of Solids* 8 (2) (May): 100–104. doi:10.1016/0022-5096(60)90013-2. http://www.sciencedirect.com/science/article/pii/0022509660900132.

Espinosa, Horacio D., and Pablo D. Zavattieri. 2003. "A Grain Level Model for the Study of Failure Initiation and Evolution in Polycrystalline Brittle Materials. Part I: Theory and Numerical Implementation." *Mechanics of Materials* 35 (3-6) (March): 333–364. doi:10.1016/S0167-6636(02)00285-5. http://www.sciencedirect.com/science/article/pii/S0167663602002855.

Fisher, R. A. 1935a. *Statistical Methods for Research Workers(Oliver and Boyd)*.

———. 1935b. *The Design of Experiments (Oliver and Boyd)*.

Fleischhauer, R., H. Dal, M. Kaliske, and K. Schneider. 2012. "A Constitutive Model for Finite Deformation of Amorphous Polymers." *International Journal of Mechanical Sciences* 65 (1) (December): 48–63. doi:10.1016/j.ijmecsci.2012.09.003. http://www.sciencedirect.com/science/article/pii/S0020740312001981.

Fotheringham, D. G., and B. W. Cherry. 1978. "The Role of Recovery Forces in the Deformation of Linear Polyethylene." *Journal of Materials Science* 13 (5) (May): 951–964. doi:10.1007/BF00544690. http://link.springer.com/10.1007/BF00544690.

Fotheringham, David, B. W. Cherry, and C. Bauwens-Crowet. 1976. "Comment on the Compression Yield Behaviour of Polymethyl Methacrylate over a Wide Range of Temperatures and Strain-Rates." *Journal of Materials Science* 11 (7): 1368–1371. doi:10.1007/BF00545162. http://link.springer.com/10.1007/BF00545162.

Fountain, Jason Elvin. 2010. "Microstucture-Based Multistage Fatigue Characterization and Modeling of an Acrylonitrile Butadiene Styrene Copolymer." Mississippi State University.

Francis, D.K., J.L. Bouvard, Y. Hammi, and M.F. Horstemeyer. 2014. "Formulation of a Damage Internal State Variable Model for Amorphous Glassy Polymers." *International Journal of Solids and Structures* 51 (15-16) (August): 2765–2776. doi:10.1016/j.ijsolstr.2014.03.025. http://www.sciencedirect.com/science/article/pii/S0020768314001231.

Frank, F. C. 1970. “The Strength and Stiffness of Polymers.” *Proceedings of the Royal Society A: Mathematical, Physical and Engineering Sciences* 319 (1536) (October 6): 127–136. doi:10.1098/rspa.1970.0170. http://rspa.royalsocietypublishing.org/content/319/1536/127.short.

Fu, Shao-Yun, Xi-Qiao Feng, Bernd Lauke, and Yiu-Wing Mai. 2008. “Effects of Particle Size, Particle/matrix Interface Adhesion and Particle Loading on Mechanical Properties of Particulate–polymer Composites.” *Composites Part B: Engineering* 39 (6) (September): 933–961. doi:10.1016/j.compositesb.2008.01.002. http://www.sciencedirect.com/science/article/pii/S135983680800005X.

Gall, Ken, M. F. Horstemeyer, D. L. McDowell, and J. Fan. 2000. “Finite Element Analysis of the Stress Distributions near Damaged Si Particle Clusters in Cast Al–Si Alloys.” *Mechanics of Materials* 32 (5) (May): 277–301. doi:10.1016/S0167-6636(00)00003-X. http://linkinghub.elsevier.com/retrieve/pii/S016766360000003X.

Gall, Ken, M.F Horstemeyer, Mark Van Schilfgaarde, and M.I Baskes. 2000. “Atomistic Simulations on the Tensile Debonding of an Aluminum–silicon Interface.” *Journal of the Mechanics and Physics of Solids* 48 (10) (October): 2183–2212. doi:10.1016/S0022-5096(99)00086-1. http://linkinghub.elsevier.com/retrieve/pii/S0022509699000861.

Gam, K. T., M. Miyamoto, R. Nishimura, and H. J. Sue. 2003. “Fracture Behavior of Core-Shell Rubber-Modified Clay-Epoxy Nanocomposites.” *Polymer Engineering & Science* 43 (10) (October 7): 1635–1645. doi:10.1002/pen.10137. http://doi.wiley.com/10.1002/pen.10137.

Glaessgen, E. H., E. Saether, and D. R. Phillips. 2006. “Multiscale Modeling of Grain-Boundary Fracture: Cohesive Zone Models Parameterized from Atomistic Simulations.” In *47th AIAA/ASME/ASCE/AHS/ASC Structures, Structural Dynamics, and Materials Conference*. Newport, Rhode Island. http://arc.aiaa.org/doi/abs/10.2514/6.2006-1674.

Govaert, L. E., P. H. M. Timmermans, and W. A. M. Brekelmans. 2000. “The Influence of Intrinsic Strain Softening on Strain Localization in Polycarbonate: Modeling and Experimental Validation.” *Journal of Engineering Materials and Technology* 122 (2) (April 1): 177. doi:10.1115/1.482784. http://materialstechnology.asmedigitalcollection.asme.org/article.aspx?articleid=1426132.

Hachour, K., F. Zaïri, M. Naït-Abdelaziz, J.M. Gloaguen, M. Aberkane, and J.M. Lefebvre. 2014. “Experiments and Modeling of High-Crystalline Polyethylene Yielding under Different Stress States.” *International Journal of Plasticity* 54 (March): 1–18. doi:10.1016/j.ijplas.2013.06.004. http://www.sciencedirect.com/science/article/pii/S0749641913001150.

Hagerman, Edward M. 1973. “Mechanism of Yield and Fracture in ABS Materials.” *Journal of Applied Polymer Science* 17 (7) (July): 2203–2212. doi:10.1002/app.1973.070170719. http://doi.wiley.com/10.1002/app.1973.070170719.

Haward, R. N., and G. Thackray. 1968. “The Use of a Mathematical Model to Describe Isothermal Stress-Strain Curves in Glassy Thermoplastics.” *Proceedings of the Royal Society A: Mathematical, Physical and Engineering Sciences* 302 (1471) (January 23): 453–472. doi:10.1098/rspa.1968.0029. http://rspa.royalsocietypublishing.org/content/302/1471/453.short.

Hay, J. M., and D. Lyon. 1967. “Vinyl Alcohol: A SGas Phase Species?” *Nature* 216 (5117) (November 25): 790–791. doi:10.1038/216790a0. http://dx.doi.org/10.1038/216790a0.

Hayward, V., S. Aubry, A. Foisy, and Y. Ghallab. 1995. “Efficient Collision Prediction Among Many Moving Objects.” *The International Journal of Robotics Research* 14 (2) (April 1): 129–143. doi:10.1177/027836499501400203. http://ijr.sagepub.com/content/14/2/129.abstract.

Heinz, Hendrik, Hilmar Koerner, Kelly L. Anderson, Richard A. Vaia, and B. L. Farmer. 2005. “Force Field for Mica-Type Silicates and Dynamics of Octadecylammonium Chains Grafted to Montmorillonite.” *Chemistry of Materials* 17 (23) (November): 5658–5669. doi:10.1021/cm0509328. http://dx.doi.org/10.1021/cm0509328.

Hibbitt, H.D. 1984. “ABAQUS/EPGEN—A General Purpose Finite Element Code with Emphasis on Nonlinear Applications.” *Nuclear Engineering and Design* 77 (3) (February): 271–297. doi:10.1016/0029-5493(84)90106-7. http://www.sciencedirect.com/science/article/pii/0029549384901067.

Horstemeyer, M. F. 2012. *Integrated Computational Materials Engineering (ICME) for Metals*.

Horstemeyer, M. F., and S. Ramaswamy. 2000. “On Factors Affecting Localization and Void Growth in Ductile Metals: A Parametric Study.” *International Journal of Damage Mechanics* 9 (1) (January 1): 5–28. doi:10.1177/105678950000900102. http://ijd.sagepub.com/content/9/1/5.short.

Horstemeyer, M.F. 2012. *Integrated Computation Materials Engineering (ICME) for Metals*. John Wiley & Sons, Inc.

Horstemeyer, M.F., J. Lathrop, A.M. Gokhale, and M. Dighe. 2000. “Modeling Stress State Dependent Damage Evolution in a Cast Al–Si–Mg Aluminum Alloy.” *Theoretical and Applied Fracture Mechanics* 33 (1) (February): 31–47. doi:10.1016/S0167-8442(99)00049-X. http://linkinghub.elsevier.com/retrieve/pii/S016784429900049X.

Horstemeyer, M.F., M.M. Matalanis, A.M. Sieber, and M.L. Botos. 2000. “Micromechanical Finite Element Calculations of Temperature and Void Configuration Effects on Void Growth and Coalescence.” *International Journal of Plasticity* 16 (7-8) (June): 979–1015. doi:10.1016/S0749-6419(99)00076-5. http://www.sciencedirect.com/science/article/pii/S0749641999000765.

Horstemeyer, M.F., D.L. McDowell, and R.D. McGinty. 1999. “Design of Experiments for Constitutive Model Selection: Application to Polycrystal Elastoviscoplasticity.” *Mod. Simul. Mater. Sci. Eng.* 7: 253–273.

Horstemeyer, M.F., S. Ramaswamy, and M. Negrete. 2003. “Using a Micromechanical Finite Element Parametric Study to Motivate a Phenomenological Macroscale Model for Void/crack Nucleation in Aluminum with a Hard Second Phase.” *Mechanics of Materials* 35 (7) (July): 675–687. doi:10.1016/S0167-6636(02)00165-5. http://www.sciencedirect.com/science/article/pii/S0167663602001655.

Horstemeyer, Mark F., and Arun M. Gokhale. 1999. “A Void–crack Nucleation Model for Ductile Metals.” *International Journal of Solids and Structures* 36 (33) (November): 5029–5055. doi:10.1016/S0020-7683(98)00239-X. http://www.sciencedirect.com/science/article/pii/S002076839800239X.

Horstemeyer, Mark F., David L. McDowell, and Douglas J. Bammann. 1996. “Torsional Softening and the Forming Limit Diagram.” In . doi:10.4271/960599. http://papers.sae.org/960599/.

Hu, Hurang, Landon Onyebueke, and Ayo Abatan. 2010. “Characterizing and Modeling Mechanical Properties of Nanocomposites- Review and Evaluation.” *Journal of Minerals & Materials Characterization & Engineering* 9 (4): 275–319.

Hughes, J. M., M. F. Horstemeyer, R. Carino, N. Sukhija, W. B. Lawrimore, S. Kim, and M. I. Baskes. 2014. “Hierarchical Bridging Between Ab Initio and Atomistic Level Computations: Sensitivity and Uncertainty Analysis for the Modified Embedded-Atom Method (MEAM) Potential (Part B).” *Jom* (December 2): 1–8. doi:10.1007/s11837-014-1205-7. http://link.springer.com/10.1007/s11837-014-1205-7.

Inberg, J.P.F., A. Takens, and R.J. Gaymans. 2002. “Strain Rate Effects in Polycarbonate and polycarbonate/ABS Blends.” *Polymer* 43 (9) (April): 2795–2802. doi:10.1016/S0032-3861(02)00081-2. http://www.sciencedirect.com/science/article/pii/S0032386102000812.

Khan, Akhtar S., Oscar Lopez-Pamies, and Rehan Kazmi. 2006. “Thermo-Mechanical Large Deformation Response and Constitutive Modeling of Viscoelastic Polymers over a Wide Range of Strain Rates and Temperatures.” *International Journal of Plasticity* 22 (4) (April): 581–601. doi:10.1016/j.ijplas.2005.08.001. http://www.sciencedirect.com/science/article/pii/S0749641905001385.

Khan, Akhtar, and Haoyue Zhang. 2001. “Finite Deformation of a Polymer: Experiments and Modeling.” *International Journal of Plasticity* 17 (9) (September): 1167–1188. doi:10.1016/S0749-6419(00)00073-5. http://www.sciencedirect.com/science/article/pii/S0749641900000735.

Khan, Fazeel, and Colin Yeakle. 2011. “Experimental Investigation and Modeling of Non-Monotonic Creep Behavior in Polymers.” *International Journal of Plasticity* 27 (4) (April): 512–521. doi:10.1016/j.ijplas.2010.06.007. http://www.sciencedirect.com/science/article/pii/S0749641910000975.

Kim, G.-M., D.-H. Lee, B. Hoffmann, J. Kressler, and G. Stöppelmann. 2001. “Influence of Nanofillers on the Deformation Process in Layered Silicate/polyamide-12 Nanocomposites.” *Polymer* 42 (3) (February): 1095–1100. doi:10.1016/S0032-3861(00)00468-7. http://www.sciencedirect.com/science/article/pii/S0032386100004687.

Kobayashi, M, J. Toguchida, and M. Oka. 2003. “Preliminary Study of Polyvinyl Alcohol-Hydrogel (PVA-H) Artificial Meniscus.” *Biomaterials* 24 (4) (February): 639–647. doi:10.1016/S0142-9612(02)00378-2. http://www.sciencedirect.com/science/article/pii/S0142961202003782.

Krempl, Erhard. 1995. “The Overstress Ddependence of Inelastic Rate of Deformation Inferred From Transient Tests.” *Journal of the Society of Materials Science, Japan* 44 (498Appendix) (March): 3–10. doi:10.2472/jsms.44.498Appendix_3. http://ci.nii.ac.jp/naid/110002283699/en/.

Launay, A., M.H. Maitournam, Y. Marco, I. Raoult, and F. Szmytka. 2011. “Cyclic Behaviour of Short Glass Fibre Reinforced Polyamide: Experimental Study and Constitutive Equations.” *International Journal of Plasticity* 27 (8) (August): 1267–1293. doi:10.1016/j.ijplas.2011.02.005. http://www.sciencedirect.com/science/article/pii/S0749641911000210.

Lawrimore II, W. B., B. Paliwal, M. Q. Chandler, K. L. Johnson, and M. F. Horstemeyer. 2016. “Hierarchical Multiscale Modeling of Polyvinyl Alcohol/Montmorillonite Nanocomposites.” *Composites Science and Technology* Submitted.

Lawrimore II, W.B., D.K. Francis, J.L. Bouvard, Y. Hammi, and M.F. Horstemeyer. 2016. “A Mesomechanics Parametric Finite Element Study of Damage Growth and Coalescence in Polymers Using an Internal State Variable Model.” *Mechanics of Materials* 96 (February): 83–95. doi:10.1016/j.mechmat.2016.02.002. http://www.sciencedirect.com/science/article/pii/S0167663616000260.

Lee, Hyun Woo, Mohammad Rezaul Karim, Hyun Mi Ji, Jin Hyun Choi, Han Do Ghim, Sung Min Park, Weontae Oh, and Jeong Hyun Yeum. 2009. “Electrospinning Fabrication and Characterization of Poly(vinyl Alcohol)/montmorillonite Nanofiber Mats.” *Journal of Applied Polymer Science* 113 (3) (August 5): 1860–1867. doi:10.1002/app.30165. http://doi.wiley.com/10.1002/app.30165.

Lemaitre, J., and J. L. Chaboche. 1990. *Mechanics of Solid Materials*. Cambridge University Press.

Lin, T.H., D. Salinas, and Y.M. Ito. 1972. “Elastic-Plastic Analysis of Unidirectional Composites.” *Journal of Composite Materials* 6 (1) (January 1): 48–60. doi:10.1177/002199837200600105. http://jcm.sagepub.com/cgi/doi/10.1177/002199837200600105.

Lu, W.Y., M.F. Horstemeyer, J.S. Korellis, R.B. Grishabar, and D. Mosher. 1998. “High Temperature Sensitivity of Notched AISI 304L Stainless Steel Tests.” *Theoretical and Applied Fracture Mechanics* 30 (2) (October): 139–152. doi:10.1016/S0167-8442(98)00051-2. http://www.sciencedirect.com/science/article/pii/S0167844298000512.

Lubarda, V.A., D.J. Benson, and M.A. Meyers. 2003. “Strain-Rate Effects in Rheological Models of Inelastic Response.” *International Journal of Plasticity* 19 (8) (August): 1097–1118. doi:10.1016/S0749-6419(02)00011-6. http://www.sciencedirect.com/science/article/pii/S0749641902000116.

Lugo, Marcos, Jason E. Fountain, Justin M. Hughes, Jean-Luc Bouvard, and Mark F. Horstemeyer. 2014. “Microstructure-Based Fatigue Modeling of an Acrylonitrile Butadiene Styrene (ABS) Copolymer.” *Journal of Applied Polymer Science* 131 (20) (October 15): n/a–n/a. doi:10.1002/app.40882. http://doi.wiley.com/10.1002/app.40882.

Markarian, Jennifer. 2007. “Strengthening Compounds through Fibre Reinforcement.” *Reinforced Plastics* 51 (2) (February): 36–39. doi:10.1016/S0034-3617(07)70057-7. http://www.sciencedirect.com/science/article/pii/S0034361707700577.

McClintock, F. A. 1968. “A Criterion for Ductile Fracture by the Growth of Holes.” *Journal of Applied Mechanics* 35 (2) (June 1): 363. doi:10.1115/1.3601204. http://appliedmechanics.asmedigitalcollection.asme.org/article.aspx?articleid=1398614.

McNally, Tony, W. Raymond Murphy, Chun Y. Lew, Robert J. Turner, and Gerard P. Brennan. 2003. “Polyamide-12 Layered Silicate Nanocomposites by Melt Blending.” *Polymer* 44 (9) (April): 2761–2772. doi:10.1016/S0032-3861(03)00170-8. http://www.sciencedirect.com/science/article/pii/S0032386103001708.

Miller, M.P., and D.L. McDowell. 1996. “Modeling Large Strain Multiaxial Effects in FCC Polycrystals.” *International Journal of Plasticity* 12 (7) (January): 875–902. doi:10.1016/S0749-6419(96)00032-0. http://www.scopus.com/inward/record.url?eid=2-s2.0-0030399376&partnerID=tZOtx3y1.

Needleman, A. 1987. “A Continuum Model for Void Nucleation by Inclusion Debonding.” *Journal of Applied Mechanics* 54 (3) (September 1): 525. doi:10.1115/1.3173064. http://appliedmechanics.asmedigitalcollection.asme.org/article.aspx?articleid=1408962.

———. 1990a. “An Analysis of Tensile Decohesion along an Interface.” *Journal of the Mechanics and Physics of Solids* 38 (3) (January): 289–324. doi:10.1016/0022-5096(90)90001-K. http://linkinghub.elsevier.com/retrieve/pii/002250969090001K.

———. 1990b. “An Analysis of Decohesion along an Imperfect Interface.” *International Journal of Fracture* 42 (1) (January): 21–40. doi:10.1007/BF00018611. http://link.springer.com/10.1007/BF00018611.

Newaz, Golam M. 1986. “Tensile Behavior of Clay-Filled Polyester Composites.” *Polymer Composites* 7 (3): 176–181. http://www.scopus.com/inward/record.url?eid=2-s2.0-0022733897&partnerID=tZOtx3y1.

O’Connell, P.A., and G.B. McKenna. 2002. “The Non-Linear Viscoelastic Response of Polycarbonate in Torsion: An Investigation of Time-Temperature and Time-Strain Superposition.” *Mechanics of Time-Dependent Materials* 6 (3): 207–229. doi:10.1023/A:1016205712110. http://link.springer.com/article/10.1023/A%3A1016205712110.

Paliwal, B., W. B. Lawrimore II, and M. F. Horstemeyer. 2016. “Modeling PVA-MMT Clay Nano-Interfacial Mechanical Behavior Using Molecular Dynamics.” *(To Be Submitted)*.

Park, Kyoungsoo, and Glaucio H. Paulino. 2013. “Cohesive Zone Models: A Critical Review of Traction-Separation Relationships Across Fracture Surfaces.” *Applied Mechanics Reviews* 64 (6) (February 5): 060802. doi:10.1115/1.4023110. http://appliedmechanicsreviews.asmedigitalcollection.asme.org/article.aspx?articleid=1678924.

Passerello, C.E. 1982. “Interference Detection Using Barycentric Coordinates.” *Mechanics Research Communications* 9 (6): 373–378.

Pavlidou, S., and C.D. Papaspyrides. 2008. “A Review on Polymer–layered Silicate Nanocomposites.” *Progress in Polymer Science* 33 (12) (December): 1119–1198. doi:10.1016/j.progpolymsci.2008.07.008. http://www.sciencedirect.com/science/article/pii/S0079670008000701.

Plimpton, Steve. 1995. “Fast Parallel Algorithms for Short-Range Molecular Dynamics.” *Journal of Computational Physics* 117 (1) (March): 1–19. doi:10.1006/jcph.1995.1039. http://www.sciencedirect.com/science/article/pii/S002199918571039X.

Ploehn, Harry J., and Chunyan Liu. 2006. “Quantitative Analysis of Montmorillonite Platelet Size by Atomic Force Microscopy.” *Industrial & Engineering Chemistry Research* 45 (21) (October): 7025–7034. doi:10.1021/ie051392r. http://dx.doi.org/10.1021/ie051392r.

Ponçot, M., F. Addiego, and A. Dahoun. 2013. “True Intrinsic Mechanical Behaviour of Semi-Crystalline and Amorphous Polymers: Influences of Volume Deformation and Cavities Shape.” *International Journal of Plasticity* 40 (January): 126–139. doi:10.1016/j.ijplas.2012.07.007. http://www.sciencedirect.com/science/article/pii/S0749641912001155.

Popa, C.M., R. Fleischhauer, K. Schneider, and M. Kaliske. 2014. “Formulation and Implementation of a Constitutive Model for Semicrystalline Polymers.” *International Journal of Plasticity* 61 (October): 128–156. doi:10.1016/j.ijplas.2014.05.010. http://www.sciencedirect.com/science/article/pii/S0749641914001156.

Poulain, X., A.A. Benzerga, and R.K. Goldberg. 2014. “Finite-Strain Elasto-Viscoplastic Behavior of an Epoxy Resin: Experiments and Modeling in the Glassy Regime.” *International Journal of Plasticity* 62 (November): 138–161. doi:10.1016/j.ijplas.2014.07.002. http://www.sciencedirect.com/science/article/pii/S0749641914001351.

Pouriayevali, H., S. Arabnejad, Y.B. Guo, and V.P.W. Shim. 2013. “A Constitutive Description of the Rate-Sensitive Response of Semi-Crystalline Polymers.” *International Journal of Impact Engineering* 62 (December): 35–47. doi:10.1016/j.ijimpeng.2013.05.002. http://www.sciencedirect.com/science/article/pii/S0734743X13001085.

Prager, W. 1944. “Exploring Stress-Strain Relations of Isotropic Plastic Solids.” *Journal of Applied Physics* 15 (1) (April 15): 65. doi:10.1063/1.1707369. http://scitation.aip.org/content/aip/journal/jap/15/1/10.1063/1.1707369.

Prantil, Vincent C., James T. Jenkins, and Paul R. Dawson. 1993. “An Analysis of Texture and Plastic Spin for Planar Polycrystals.” *Journal of the Mechanics and Physics of Solids* 41 (8) (August): 1357–1382. doi:10.1016/0022-5096(93)90084-S. http://www.sciencedirect.com/science/article/pii/002250969390084S.

Radon, J. C. 1980. “Fatigue Crack Growth in Polymers.” *International Journal of Fracture* 16 (6) (December): 533–552. doi:10.1007/BF02265216. http://link.springer.com/10.1007/BF02265216.

Ramakrishnan, R., and L. Karunamoorthy. 2005. “Multi Response Optimization of Wire EDM Operations Using Robust Design of Experiments.” *The International Journal of Advanced Manufacturing Technology* 29 (1-2) (July 6): 105–112. doi:10.1007/s00170-004-2496-6. http://link.springer.com/10.1007/s00170-004-2496-6.

Rice, J.R. 1971. “Inelastic Constitutive Relastions for Solids : An Internal-Variable Theroy and Its Application to Metal Plasticity.” *Mech. Phys. Solids* 19: 433–455.

Richeton, J., S. Ahzi, K.S. Vecchio, F.C. Jiang, and A. Makradi. 2007. “Modeling and Validation of the Large Deformation Inelastic Response of Amorphous Polymers over a Wide Range of Temperatures and Strain Rates.” *International Journal of Solids and Structures* 44 (24): 7938–7954. http://www.sciencedirect.com/science/article/pii/S0020768307002296.

Richeton, J., G. Schlatter, K.S. Vecchio, Y. Rémond, and S. Ahzi. 2005. “A Unified Model for Stiffness Modulus of Amorphous Polymers across Transition Temperatures and Strain Rates.” *Polymer* 46 (19) (September): 8194–8201. doi:10.1016/j.polymer.2005.06.103. http://www.sciencedirect.com/science/article/pii/S0032386105009389.

Riddell, M. N., G. P. Koo, and J. L. O’Toole. 1966. “Fatigue Mechanisms of Thermoplastics.” *Polymer Engineering and Science* 6 (4) (October): 363–368. doi:10.1002/pen.760060414. http://doi.wiley.com/10.1002/pen.760060414.

Sapalidis, Andreas A., Fotios K. Katsaros, and Nick K. Kanellopoulos. 2011. “PVA/Montmorillonite Nanocomposites: Development and Properties.” In *Nanocomposites and Polymers with Analytical Methods*, edited by John Cuppoletti, 29–50. InTech. doi:10.5772/1548. http://www.intechopen.com/books/nanocomposites-and-polymers-with-analytical-methods/pva-montmorillonite-nanocomposites-development-and-properties.

Sheng, N., M. C. Boyce, D. M. Parks, G. C. Rutledge, J. I. Abes, and R. E. Cohen. 2004. “Multiscale Micromechanical Modeling of Polymer/clay Nanocomposites and the Effective Clay Particle.” *Polymer* 45 (2): 487–506. http://www.sciencedirect.com/science/article/pii/S0032386103010425.

Shepherd, P.D., F.J. Golemba, and F.W. Maine. 1973. *Mica Reinforced Plastics*. *Am Chem Soc Div Org Coatings Plast Chem Prepr*. Vol. 33. http://www.scopus.com/inward/record.url?eid=2-s2.0-0015936712&partnerID=tZOtx3y1.

Shojaei, Amir, and Guoqiang Li. 2013. "Viscoplasticity Analysis of Semicrystalline Polymers: A Multiscale Approach within Micromechanics Framework." *International Journal of Plasticity* 42 (March): 31–49. doi:10.1016/j.ijplas.2012.09.014. http://www.sciencedirect.com/science/article/pii/S0749641912001441.

Sinha Ray, Suprakas, M. Bousmina, and A. Maazouz. 2006. "Morphology and Properties of Organoclay Modified Polycarbonate/Poly(methyl Methacrylate) Blend." *Polymer Engineering & Science* 46 (8): 1121–1129.

Siviour, C.R., S.M. Walley, W.G. Proud, and J.E. Field. 2005. "The High Strain Rate Compressive Behaviour of Polycarbonate and Polyvinylidene Difluoride." *Polymer* 46 (26) (December): 12546–12555. doi:10.1016/j.polymer.2005.10.109. http://www.sciencedirect.com/science/article/pii/S0032386105015806.

Song, Shaoning, Yu Chen, Zhoucheng Su, Chenggen Quan, and Vincent B.C. Tan. 2013. "Effects of Clay Structural Parameters and Gallery Strength on the Damage Behavior of Epoxy/clay Nanocomposites." *Composites Science and Technology* 85 (August): 50–57. doi:10.1016/j.compscitech.2013.05.019. http://www.sciencedirect.com/science/article/pii/S0266353813002376.

———. 2014. "Multiscale Modeling of Damage Progression in Nylon 6/clay Nanocomposites." *Composites Science and Technology*, August. doi:10.1016/j.compscitech.2014.06.014. http://www.sciencedirect.com/science/article/pii/S0266353814002152.

Soundararajah, Q.Y., B.S.B. Karunaratne, and R.M.G. Rajapakse. 2009. "Mechanical Properties of Poly(vinyl Alcohol) Montmorillonite Nanocomposites." *Journal of Composite Materials* 44 (3) (September 22): 303–311. doi:10.1177/0021998309347040. http://jcm.sagepub.com/content/44/3/303.abstract.

Spencer, P E, and J Sweeney. 2008. "Modelling of Polymer Clay Nanocomposites for a Multiscale Approach." *ArXiv*.

Srivastava, Vikas, Shawn A. Chester, Nicoli M. Ames, and Lallit Anand. 2010. "A Thermo-Mechanically-Coupled Large-Deformation Theory for Amorphous Polymers in a Temperature Range Which Spans Their Glass Transition." *International Journal of Plasticity* 26 (8) (August): 1138–1182. doi:10.1016/j.ijplas.2010.01.004. http://www.sciencedirect.com/science/article/pii/S0749641910000057.

Stoilov, Vesselin. 2008. “A Multiscale Model of First and Second Order Phase Transformations with Application to SMA Single Crystals.” *Multiscale Modeling & Simulation* 7 (1) (January 16): 197–213. doi:10.1137/070695940. http://epubs.siam.org/doi/abs/10.1137/070695940.

Strawhecker, K. E., and E. Manias. 2000. “Structure and Properties of Poly(vinyl alcohol)/Na + Montmorillonite Nanocomposites.” *Chemistry of Materials* 12 (10) (October): 2943–2949. doi:10.1021/cm000506g. http://dx.doi.org/10.1021/cm000506g.

Taguchi, G. 1974. “Shaishin Igaku.” *The Newest Medicine* 9: 806–13.

———. 1986. *Introduction to Quality Engineering: Designing Quality into Products and Processes*. Quality Resources.

———. 1987. *The System of Experimental Design: Engineering Methods to Optimize Quality and Minimize Costs*. Vol 1 & 2. Quality Resources.

Tay, T.E., F. Shen, K.H. Lee, A. Scaglione, and M. Di Sciuva. 1999. “Mesh Design in Finite Element Analysis of Post-Buckled Delamination in Composite Laminates.” *Composite Structures* 47 (1-4) (December): 603–611. doi:10.1016/S0263-8223(00)00033-7. http://www.sciencedirect.com/science/article/pii/S0263822300000337.

Tehrani, Ardeshir H., and Rashid K. Abu Al-Rub. 2011. “Mesomechanical Modeling of Polymer⁄Clay Nanocomposites Using a Viscoelastic-Viscoplastic-Viscodamage Constitutive Model.” *Journal of Engineering Materials and Technology* 133 (4): 041011. doi:10.1115/1.4004696. http://materialstechnology.asmedigitalcollection.asme.org/article.aspx?articleid=1429078.

Tervoort, T. A., and L. E. Govaert. 2000. “Strain-Hardening Behavior of Polycarbonate in the Glassy State.” *Journal of Rheology* 44 (6) (November 1): 1263. doi:10.1122/1.1319175. http://scitation.aip.org/content/sor/journal/jor2/44/6/10.1122/1.1319175.

Tervoort, T.A., R.J.M. Smit, W.A.M. Brekelmans, and L.E. Govaert. 1997. “A Constitutive Equation for the Elasto-Viscoplastic Deformation of Glassy Polymers.” *Mechanics of Time-Dependent Materials* 1 (3) (September 1): 269–291. doi:10.1023/A:1009720708029. http://link.springer.com/article/10.1023/A:1009720708029.

Tijssens, M. 2000. “Modeling of Crazing Using a Cohesive Surface Methodology.” *Mechanics of Materials* 32: 19–35.

Tjia, J S, and P V Moghe. 1998. “Analysis of 3-D Microstructure of Porous Poly(lactide-Glycolide) Matrices Using Confocal Microscopy.” *Journal of Biomedical Materials Research* 43 (3) (January): 291–9. http://www.ncbi.nlm.nih.gov/pubmed/9730067.

Tvergaard, V. 1990. “Material Failure by Growth to Coalescence.” *Advances in Applied Mechanics* 27: 83–151.

Tvergaard, Viggo, and John W. Hutchinson. 1992. “The Relation between Crack Growth Resistance and Fracture Process Parameters in Elastic-Plastic Solids.” *Journal of the Mechanics and Physics of Solids* 40 (6) (August): 1377–1397. doi:10.1016/0022-5096(92)90020-3. http://www.sciencedirect.com/science/article/pii/0022509692900203.

———. 1996. “On the Toughness of Ductile Adhesive Joints.” *Journal of the Mechanics and Physics of Solids* 44 (5) (May): 789–800. doi:10.1016/0022-5096(96)00011-7. http://www.sciencedirect.com/science/article/pii/0022509696000117.

Uchida, Makoto, and Naoya Tada. 2013. “Micro-, Meso- to Macroscopic Modeling of Deformation Behavior of Semi-Crystalline Polymer.” *International Journal of Plasticity* 49 (October): 164–184. doi:10.1016/j.ijplas.2013.03.007. http://www.sciencedirect.com/science/article/pii/S0749641913000776.

Valavala, P K, and G M Odegard. 2005. “MODELING TECHNIQUES FOR DETERMINATION OF MECHANICAL PROPERTIES OF POLYMER NANOCOMPOSITES.” *Reviews on Advanced Materials Science* 9: 34–44.

van der Sluis, O., P.J.G. Schreurs, and H.E.H. Meijer. 2001. “Homogenisation of Structured Elastoviscoplastic Solids at Finite Strains.” *Mechanics of Materials* 33 (9) (September): 499–522. doi:10.1016/S0167-6636(01)00066-7. http://www.sciencedirect.com/science/article/pii/S0167663601000667.

Varlot, K., E. Reynaud, M. H. Kloppfer, G. Vigier, and J. Varlet. 2001. “Clay-Reinforced Polyamide: Preferential Orientation of the Montmorillonite Sheets and the Polyamide Crystalline Lamellae.” *Journal of Polymer Science Part B: Polymer Physics* 39 (12) (June 15): 1360–1370. doi:10.1002/polb.1108. http://doi.wiley.com/10.1002/polb.1108.

Voyiadjis, George Z., Amir Shojaei, and Guoqiang Li. 2012. “A Generalized Coupled Viscoplastic–viscodamage–viscohealing Theory for Glassy Polymers.” *International Journal of Plasticity* 28 (1) (January): 21–45. doi:10.1016/j.ijplas.2011.05.012. http://www.sciencedirect.com/science/article/pii/S0749641911000969.

Wang, H.W., H.W. Zhou, R.D. Peng, and Leon Mishnaevsky. 2011. “Nanoreinforced Polymer Composites: 3D FEM Modeling with Effective Interface Concept.” *Composites Science and Technology* 71 (7) (May): 980–988. doi:10.1016/j.compscitech.2011.03.003. http://www.sciencedirect.com/science/article/pii/S0266353811000935.

Wang, Ke, Ling Chen, Jingshen Wu, Mei Ling Toh, Chaobin He, and Albert F. Yee. 2005. “Epoxy Nanocomposites with Highly Exfoliated Clay: Mechanical Properties and Fracture Mechanisms.” *Macromolecules* 38 (3) (February 11): 788–800. doi:10.1021/ma048465n. http://pubs.acs.org/doi/abs/10.1021/ma048465n.

Wang, L, S Daniewicz, M Horstemeyer, S Sintay, and a Rollett. 2009. “Three-Dimensional Finite Element Analysis Using Crystal Plasticity for a Parameter Study of Fatigue Crack Incubation in a 7075 Aluminum Alloy.” *International Journal of Fatigue* 31 (4) (April): 659–667. doi:10.1016/j.ijfatigue.2008.03.022. http://linkinghub.elsevier.com/retrieve/pii/S0142112308000716.

Xu, X -P, and A Needleman. 1993. “Void Nucleation by Inclusion Debonding in a Crystal Matrix.” *Modelling and Simulation in Materials Science and Engineering* 1 (2) (January 1): 111–132. doi:10.1088/0965-0393/1/2/001. http://iopscience.iop.org/article/10.1088/0965-0393/1/2/001.

Yamakov, V., E. Saether, and E. H. Glaessgen. 2008. “Multiscale Modeling of Intergranular Fracture in Aluminum: Constitutive Relation for Interface Debonding.” *Journal of Materials Science* 43 (23-24) (August 7): 7488–7494. doi:10.1007/s10853-008-2823-7. http://link.springer.com/10.1007/s10853-008-2823-7.

Yamakov, V., E. Saether, D.R. Phillips, and E.H. Glaessgen. 2006. “Molecular-Dynamics Simulation-Based Cohesive Zone Representation of Intergranular Fracture Processes in Aluminum.” *Journal of the Mechanics and Physics of Solids* 54 (9) (September): 1899–1928. doi:10.1016/j.jmps.2006.03.004. http://www.sciencedirect.com/science/article/pii/S0022509606000421.

Yang, Seunghwa, Suyoung Yu, Junghyun Ryu, Jeong-Min Cho, Woomin Kyoung, Do-Suck Han, and Maenghyo Cho. 2013. “Nonlinear Multiscale Modeling Approach to Characterize Elastoplastic Behavior of CNT/polymer Nanocomposites Considering the Interphase and Interfacial Imperfection.” *International Journal of Plasticity* 41 (February): 124–146. doi:10.1016/j.ijplas.2012.09.010. http://www.sciencedirect.com/science/article/pii/S0749641912001404.

Zaïri, F., M. Naït-Abdelaziz, J.M. Gloaguen, and J.M. Lefebvre. 2011. “A Physically-Based Constitutive Model for Anisotropic Damage in Rubber-Toughened Glassy Polymers during Finite Deformation.” *International Journal of Plasticity* 27 (1) (January): 25–51. doi:10.1016/j.ijplas.2010.03.007. http://www.sciencedirect.com/science/article/pii/S07496t1910000495.

Zaïri, Fahmi, Moussa Naït-Abdelaziz, Krzysztof Woznica, and Jean-Michel Gloaguen. 2007. “Elasto-Viscoplastic Constitutive Equations for the Description of Glassy Polymers Behavior at Constant Strain Rate.” *Journal of Engineering Materials and Technology* 129 (1) (January 1): 29. doi:10.1115/1.2400256. http://materialstechnology.asmedigitalcollection.asme.org/article.aspx?articleid=1427906.

Zhang, Qiang, and Qing-Sheng Yang. 2012. “Recent Advance on Constitutive Models of Thermal-Sensitive Shape Memory Polymers.” *Journal of Applied Polymer Science* 123 (3) (February 5): 1502–1508. doi:10.1002/app.34307. http://doi.wiley.com/10.1002/app.34307.

Zhou, X.W., N.R. Moody, R.E. Jones, J.A. Zimmerman, and E.D. Reedy. 2009. “Molecular-Dynamics-Based Cohesive Zone Law for Brittle Interfacial Fracture under Mixed Loading Conditions: Effects of Elastic Constant Mismatch.” *Acta Materialia* 57 (16) (September): 4671–4686. doi:10.1016/j.actamat.2009.06.023. http://www.sciencedirect.com/science/article/pii/S1359645409003723.

Zhou, X.W., J.A. Zimmerman, E.D. Reedy, and N.R. Moody. 2008. “Molecular Dynamics Simulation Based Cohesive Surface Representation of Mixed Mode Fracture.” *Mechanics of Materials* 40 (10) (October): 832–845. doi:10.1016/j.mechmat.2008.05.001. http://www.sciencedirect.com/science/article/pii/S0167663608000628.

APPENDIX A

INTERNAL STATE VARIABLE MODEL CALIBRATED MATERIAL PARAMETERS

Table A.1 Calibrated Internal State Variable (ISV) polymer model constants for Acrylonitrile Butadiene Styrene (ABS), Polypropylene (PP), Polycarbonate (PC), and Polyvinyl Alcohol (PVA).

Regime	Param.	Constant	Material				Units
			ABS	PP	PC	PVA	
Elasticity	E	E_{ref}	1891	1500	2600	900	MPa
		E_0	-5	0	0	0	MPa/K
		V_{E1}	1	0	0.1	0.1	
		V_{E2}	0.01	0.1	0.1	0.1	
	ν		0.36	0.45	0.37	0.42	
	$\dot{\varepsilon}_{ref}$		1000	1000	1000	1000	1/s
Viscoplasticity	$\dot{\bar{\gamma}}^p$	$\dot{\bar{\gamma}}_0^p$	4.21E+23	2000	2000	300	1/s
		ΔH_β	81	31.5	19	25	kJ/mol
		V	1.00E-28	1.00E-27	1.00-27	1.00E-27	m^3
		m	9	1	1	1	
	$Y(\theta)$	C_3	-0.15	0	0	0	MPa
		C_4	14	3.5	2	12	MPa
		a_Y	0	0	0	0	
		b_y	0	0	0	0	
Softening ($\bar{\xi}_1$)	$\bar{\xi}_0^*$	C_5	0.004	0	0	0	
		C_6	0.3	0.93	0.6	0.5	1/K
	$\bar{\xi}_{1_{sat}}^*$	C_7	0.001	0	0	0	
		C_8	0.31	0.2	0.75	1	
	g_0	C_9	-0.8	0	0	0	
		C_{10}	60	6	4	0	
		a_{g_0}	0	-5	-8	0	
		b_{g_0}	0	2	1	0	
	κ_1	$C_{\bar{\kappa}_1}$	0.03	0.027	0.08	0.026	
		a_{κ_1}	0	28	2.5	0	
		b_{κ_1}	0	-1	0.3	0	
	h_0		50	10.7	35	60	
	$\bar{\xi}_{1_0}^*$		0	0	0	0	

Table A.1 (Continued)

Hardening ($\bar{\xi}_2$)	$\bar{\xi}^*_{2_{sat}}$	C_{11}	0	0	-0.2	0	
		C_{12}	0.7	0.5	0.8	0.01	
	$\bar{\kappa}_2$	$C_{\bar{\kappa}_2}$	0	0.037	0.08	0	
		a_{κ_2}	0	-350	-100	0	
		b_{κ_2}	0	2.25	-0.001	0	
	h_1		0	2.5	10	0	
	$\bar{\xi}^*_{2_0}$		0	0	0	0	
Hardening ($\bar{\alpha}$)	R_{s_1}	C_{13}	-0.01	0	0	0	
		C_{14}	0.8	0.8	1.11	0.5	
	μ_R	C_1	-0.11	0	0	0	MPa
		C_2	9	0.32	3	20	MPa/K
	μ_B	λ_L	3	5	3.5	2.5	
		a_α	0	1700	-101.5	0	
		b_α	0	17	7.2	0	
Thermal	θ_{ref}		298	298	298	298	K
	θ_{init}		298	298	298	298	K
	θ_{glass}		400	273	433	358	K

APPENDIX B

VIRTUAL COMPOSITE STRUCTURE GENERATION (VCSG) ALGORITHM

As introduced in section 4.1., the VCSG algorithm uses Random Sequential Absorption (RSA) and interference detection to generate random assortments of inclusions within a matrix. RSA governed the creation of RVEs by:

1. Define candidate inclusion's properties such as dimensions, thickness, intercalation level, gallery strength (if a gallery is present), and maximum orientation freedom (θ_{max}).
2. Generate a random trial position $(x_{trial}, y_{trial}, z_{trial})$ and random trial orientation $(\alpha_{trial}, \beta_{trial}, \gamma_{trial})$ for the candidate with the constraints:
    a. $0 < (x_{trial}, y_{trial}, z_{trial}) < D_{RVE}$
    b. $0 < (\alpha_{trial}, \beta_{trial}, \gamma_{trial}) < \theta_{max}$
3. Perform interference detection verification scheme for the candidate inclusion at the trial location and orientation
    a. Generate a list of all pre-existing inclusions within the neighborhood of the candidate's trial position.
    b. Reject candidate inclusion if any part of its volume occupies the same space as another inclusion.
4. If candidate inclusion has remained unrejected, determine if the candidate penetrates the outer boundaries of the RVE and if so, enforce periodicity.
    a. Make a copy of the candidate inclusion for each RVE boundary face from which it protrudes (a candidate at a corner may penetrate multiple faces).
    b. Move each copy to the corresponding opposite RVE boundary face.

    c. Remove portions of candidate and copies that are outside RVE.
    d. Perform interference detection on newly formed copies.
5. If both the original candidate as well as any periodic copies have been accepted under interference detection, then place candidate and copies at their respective trial locations.
6. Repeat 2-5 until desired volume fraction is reached.

A considerable number of algorithms that vary in robustness and efficiency exist for computing the interference between virtual objects (Hayward *et al*. 1995). Given the asymmetry that is characteristic of the inclusions in this study, barycentric interference detection (Passerello 1982) was employed to prevent neighboring inclusions from intersecting within an RVE as it allows for very little wasted volume as a reasonable computational cost. The algorithm for barycentric interference detection is:

1. Identify a pair of neighboring objects to test for interference. We will refer to the first object as the "test object" (TO) and the second object as the "candidate object" (CO).
2. Construct a rectangular prismatic bounding surface around both object in their respective local coordinate systems.
3. Transform the CO bounding surface into a global coordinate system.
    a. Optionally, interpolate any number of points in between the nodes of the bounding surface. More points will produce better results but will also take more time.
4. Subdivide the TO into tetrahedrons using any triangulation method.

5. Iteratively, for each node (and any interpolated points) on the bounding surface of the CO:
    a. Iteratively, for each tetrahedron within the bounding surface:
        i. Convert the current point into barcentric coordinates using the method described by Passerello (1982).
        ii. Interference is present if all barcentric coordinates of current point are between 0 and 1.
        iii. Reject CO if interference is detected.

VCSG was implemented in Matlab 2014b and features a user-friendly Graphical User Interface (GUI) that allows the manipulation of input parameters to generate input files containing lists of inclusion data. A supplementary script was composed in Python to construct an RVE within the Abaqus finite element framework using the input files generated by VCSG.

APPENDIX C

BOUVARD INTERNAL STATE VARIABLE MODEL WALKTHROUGH

The ISV constitutive model (Bouvard *et al.* 2013; Francis *et al.* 2014) was developed based upon the thermodynamic foundation proposed by Coleman and Gurtin (1967). Three ISVs accounted for polymeric internal energy dissipation mechanisms based on the molecular dynamics studies on Hossain *et al.* (2010)

C.1 Assumptions

- Plastic flow is incompressible: $|\boldsymbol{F^p}| = 1, Tr(\bar{\boldsymbol{L}}^{\boldsymbol{p}}) = 0.$
- Plastic flow is irrotational: $\overline{\boldsymbol{W}}^{\boldsymbol{p}} = 0.$
- Thermal portion of deformation gradient is isotropic: $\boldsymbol{F^\theta} = F^\theta,\ \overline{\boldsymbol{W}}^{\boldsymbol{\theta}} = 0.$

C.2 Cauchy Stress

The constitutive model consists of two intermediate configurations corresponding to the decomposition of the deformation gradient (Fig C1). All calculations are executed in the first intermediate configuration ($\overline{\boldsymbol{B}}$), and results are "pushed forward" with the elastic component of the deformation gradient.

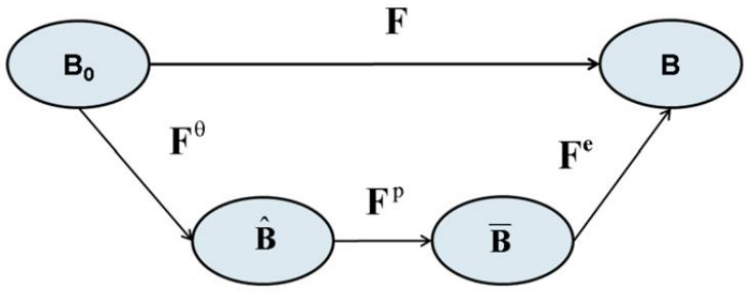

Figure C.1 Illustration of the glassy polymer Internal State Variable Model deformation gradient decomposition.

The Cauchy stress is written in terms of the Mandel stress where J^e is the Jacobian determinant of the elastic deformation gradient, $\mu(\theta)$ is the shear modulus, $K(\theta)$ is the bulk modulus, and $\overline{\boldsymbol{E}}^e$ is the elastic portion of the Green's strain tensor.

$$\boldsymbol{\sigma} = J^{e-1}\boldsymbol{\tau}, \;\; \boldsymbol{\tau} = J^{e-1}\boldsymbol{R^e}\overline{\boldsymbol{M}}\boldsymbol{R^{eT}}, \;\; \overline{\boldsymbol{M}} = 2\mu(\theta)\overline{\boldsymbol{E}}^e + \left[\boldsymbol{K}(\theta) - \frac{2}{3}\mu(\theta)\right] Tr(\overline{\boldsymbol{E}}^e)\boldsymbol{I} \quad \text{(C.1)}$$

C.3 Internal State Variables (ISVs)

The ISV rate schemes were constructed by modifying the works of Boyce *et al.* (1988) and Ames *et al.* (2009). As previously mentioned ISVs quantify unobservable, internal energy dissipation effects. This constitutive model features three such ISVs.

- The second rank tensorial quantity $\overline{\boldsymbol{\alpha}}$, seen in Equation (C.2) serves to represent large-strain hardening behavior caused by the str*etc*hing of polymer chains.

$$\overline{\boldsymbol{\alpha}} = \hat{\mu}_B(\theta)\overline{\boldsymbol{\beta}}; \;\; \hat{\mu}_B(\theta) = \mu_R(\theta)\left[1 - \frac{\lambda_1^{\overline{\beta}} + \lambda_2^{\overline{\beta}} + \lambda_3^{\overline{\beta}}}{\lambda_L}\right]^{-1} \quad \text{(C.2)}$$

$$\dot{\overline{\boldsymbol{\beta}}} = R_{s_1}(\theta)\left(\overline{\boldsymbol{D}}^p\,\overline{\boldsymbol{\beta}} + \overline{\boldsymbol{\beta}}\overline{\boldsymbol{D}}^p\right) \quad \text{(C.3)}$$

where $\mu_R(\theta)$ is a temperature dependent rubbery modulus, λ_L is a network locking str*etc*h, $\lambda_i^{\overline{\boldsymbol{\beta}}}$ are the eigenvalues of $\overline{\boldsymbol{\beta}}$, $R_{s_1}(\theta)$ is a temperature dependent material parameter, and $\boldsymbol{D}^p$ is the inelastic rate of deformation. The evolution form of $\overline{\boldsymbol{\beta}}$ is derived from the metallic kinematic hardening relation introduced by Prantil *et al.* (1993) and later modified for polymeric application by Ames *et al.* (2009).

$$R_{s_1}(\theta) = C_{13}\left(\theta - \theta_{ref}\right) + C_{14}, \;\; \mu_R(\theta) = C_1\left(\theta - \theta_{ref}\right) + C_2 \quad \text{(C.4)}$$

- A pair of scalar-valued ISVs accounting for polymer chain entanglement density as well as polymer chain coiling /alignment:

$$\bar{\kappa}_1 = C_{\bar{\kappa}_1}\mu(\theta)\bar{\xi}_1\,[1 + f(J_2,J_3)],\;\; \bar{\kappa}_2 = C_{\bar{\kappa}_2}\mu(\theta)\bar{\xi}_2 \tag{C.5}$$

where the first scalar ISV is defined:

$$\dot{\bar{\xi}}_1 = h_0\left(1 - \frac{\bar{\xi}_1}{\bar{\xi}^*}\right)\dot{\bar{\gamma}}^p,\;\; \xi^* = \left(\bar{\xi}^*_{sat} - g_0(\theta)\bar{\xi}^*\right)\dot{\bar{\gamma}}^p,\;\; \bar{\xi}^* = \bar{\xi}^*_0\; at\; t = 0 \tag{C.6}$$

where h_0 and $g_0(\theta)$ are hardening moduli (g_0 being temperature and stress state dependent), $\bar{\xi}^*$ is a temperature dependent strain-like quantity accounting for chain slippage, and $\bar{\xi}^*_{sat}$ is the temperature dependent saturation value for $\bar{\xi}^*$.

$$\bar{\xi}^*_0(\theta) = C_5\left(\theta - \theta_{ref}\right) + C_6,\;\; \bar{\xi}^*_{sat}(\theta) = C_7\left(\theta - \theta_{ref}\right) + C_8 \tag{C.7}$$

$$g_0(\theta) = \left[C_9\left(\theta - \theta_{ref}\right) + C_{10}\right] \tag{C.8}$$

The second scalar ISV is defined by:

$$\dot{\bar{\xi}}_2 = h_1\left(\,\bar{\lambda}^p - 1\right)\left(1 - \frac{\bar{\xi}_2}{\bar{\xi}_{2sat}(\theta)}\right)\dot{\bar{\gamma}}^p,\;\; \bar{\lambda}^p = \sqrt{\frac{1}{3}tr\left(\bar{\boldsymbol{B}}_p\right)} \tag{C.9}$$

where h_1 is the temperature independent hardening modulus, $\bar{\lambda}^p$ is the effective plastic str*etc*h related to the Cauchy-Green deformation tensor (Ames *et al*. 2009), and $\bar{\xi}_{2_{sat}}$ is the saturation value for $\bar{\xi}_2$.

$$\bar{\boldsymbol{B}}_p = \boldsymbol{F^p F^{p^T}},\;\; \bar{\xi}_{2_{sat}}(\theta) = C_{11}\left(\theta - \theta_{ref}\right) + C_{12} \tag{C.10}$$

C.3.1 Inelastic Rate of Deformation (Flow Rule)

A flow rule is employed to represent viscous flow phenomena rooted in relative polymer chain displacement (Boyce, Parks, and Argon 1988; L Anand and Ames 2006). The "dev" tag refers to the deviatoric portion of a tensor.

$$\dot{\boldsymbol{F}}^{\boldsymbol{p}} = \bar{\boldsymbol{D}}^{\boldsymbol{p}}\boldsymbol{F^p},\;\; \bar{\boldsymbol{D}}^{\boldsymbol{p}} = \frac{1}{\sqrt{2}}\dot{\bar{\gamma}}^p\bar{\boldsymbol{N}}^{\boldsymbol{p}},\;\; \bar{\boldsymbol{N}}^{\boldsymbol{p}} = \frac{\mathrm{dev}(\bar{\boldsymbol{M}} - \bar{\boldsymbol{\alpha}})}{\|\mathrm{dev}(\bar{\boldsymbol{M}} - \bar{\boldsymbol{\alpha}})\|} \tag{C.11}$$

where $\dot{\bar{\gamma}}^p$ represents the inelastic shear strain rate derived from a modified cooperative model (Richeton *et al*. 2005; Richeton *et al*. 2007), (D. Fotheringham,

Cherry, and Bauwens-Crowet 1976; D. G. Fotheringham and Cherry 1978) and $\bar{\boldsymbol{N}}^{\boldsymbol{p}}$ is the direction of viscous flow.

$$\dot{\bar{\gamma}}^{p} = \dot{\bar{\gamma}}_0^{p} exp\left(-\frac{\Delta H_{\beta}}{k_B \theta}\right) \sinh^{n}\left(\frac{[\bar{\tau}-(Y(\theta)+\bar{\kappa}_1+\bar{\kappa}_2)]V}{2k_B\theta}\right),\ \bar{\tau} = \frac{\mathrm{dev}\|\bar{\boldsymbol{M}}-\bar{\boldsymbol{\alpha}}\|}{\sqrt{2}}, \tag{C.12}$$

where $\dot{\bar{\gamma}}_0^{p}$ is a material constant that dictates when the inelastic shear strain rate dependence activates, ΔH_{β} is an activation energy, k_B is the Boltzmann constant, n is a parameter describing cooperative behavior of polymer chain segments, V is a shear activation volume, and $Y(\theta)$ is a temperature dependent yield surface also including the stress state dependence,

$$Y(\theta) = \{C_3\left(\theta - \theta_{ref}\right) + C_4\} \tag{C.13}$$

The effective shear stress $\bar{\tau}$ (Equation C.12) consists of the deviatoric portions of the Mandel stress and the backstress.